NASA-CR-197985

NAG3-853
399284
35p.P
INTERIM
IN-37-CR
45328
P. 186

STRATIFIED CHARGE ROTARY ENGINE COMBUSTION STUDIES

Progress Report
Submitted to

NASA Lewis Research Center
21000 Brookpark Road
Cleveland, OH 44135

by

MSU Engine Research Laboratory
Department of Mechanical Engineering
East Lansing, MI 48824

Principal Investigator:
Dr. H. Schock
Co-Investigators:
Dr. F. Hamady and Dr. C. Somerton

July 6, 1989

(NASA-CR-197985) STRATIFIED CHARGE ROTARY ENGINE COMBUSTION STUDIES Progress Report (Michigan State Univ.) 186 p

N95-24223

Unclas

G3/37 0045328

THIS REPORT WAS
PREPARED BY:

DR. H. SCHOCK, DIRECTOR, MSU ENGINE RESEARCH LAB
DR. F. HAMADY, MANAGER, MSU ENGINE RESEARCH LAB
DR. C. SOMERTON, ASSOC. PROFESSOR, MECHANICAL ENGINEERING, MSU
MR. T. STUECKEN, MSU ENGINE RESEARCH LAB
MR. E. CHOUINARD, GRADUATE STUDENT, MSU
MR. T. RACHAL, GRADUATE STUDENT, MSU
MS. J. KOSTERMAN, UNDERGRADUATE STUDENT, MSU
MR. M. LAMBETH, UNDERGRADUATE STUDENT, MTU
MR. C. OLBRICH, UNDERGRADUATE STUDENT, MSU

TABLE OF CONTENTS

1.0 INTRODUCTION

2.0 FUEL INJECTION STUDIES

2.1 Single Jet, Multi-Jet Fuel Nozzle Results
2.2 Design of Fuel Injector Assembly for RCE
2.3 Interaction With BKM
2.4 Planned Work

3.0 FLOW VISUALIZATION IN THE MOTORED RCE

3.1 Experimental Facilities and Equipment
3.1.1 Rotary Engine Assembly
3.1.2 Flow Visualization System
3.2 Results and Discussion
3.2.1 Flow Study In a Naturally Aspirated RE
3.2.2 Flow Study In a Supercharged RE
3.3 Planned Work

4.0 LASER DOPPLER VELOCIMETRY MEASUREMENTS

4.1 Brief Summary of Efforts on LDV and Status Including Pressure Measurement
4.2 Description of Optical System
4.3 Criteria for Acceptance of Data
4.4 Results in Intake/Compression
4.5 Planned Work

5.0 FRICTION STUDIES

5.1 Numerical Simulation of Thermodynamic Processes
5.2 Analysis of Bearing Friction
5.3 Apex and Side Seal Frictional Losses
5.4 Auxillary Components
5.5 Planned Work

6. 0 COMPUTER CONTROLLED SURFACE MAPPING

6.1 Description of Mapping System
6.2 Status

7. REFERENCES

8.0 APPENDICES

Appendix A - Operation of a BKM Fuel Injection System
Appendix B - SAE Paper No 890331, Feb. 27, 1989
Appendix C - LDV Data Taken in the Motored RCE Assembly*
Appendix D - Friction Studies and Ancillary Components
Appendix E - Digital Imaging System

* This material is bound under a separate cover

1.0 INTRODUCTION

Analytical and experimental studies of the combustion process in a stratified charge rotary engine (SCRE) continue to be the subject of active research in recent years. Specifically to meet the demand for more sophisticated products, a detailed understanding of the engine system of interest is warranted. With this in mind the objective of this work is to develop an understanding of the controlling factors that affect the SCRE combustion process so that efficient power dense rotary engine can be designed. The influence of the induction-exhaust systems and the rotor geometry are believed to have a significant effect on combustion chamber flow characteristics. In this report, emphasis is centered on Laser Doppler Velocimetry (LDV) measurements and on qualitative flow visualizations in the combustion chamber of the motored rotary engine assembly. This will provide a basic understanding of the flow processes in the RCE and serve as a data base for verification of numerical simulations.

Understanding fuel injection provisions is also important to the successful operation of the stratified charge rotary engine. Toward this end, flow visualizations depicting the development of high speed, high pressure fuel jets are described.

Friction is an important consideration in an engine from the standpoint of lost work, durability and reliability. MSU Engine Research Laboratory efforts in accessing the frictional losses associated with the rotary engine are described. This includes work which describes losses in bearing, seal and auxillary components.

Finally, a computer controlled mapping system under development is described. This system can be used to map shapes such as combustion chamber, intake manifolds or turbine blades accurately.

2.0 FUEL INJECTION STUDIES

During the current reporting period studies involving the BKM Servojet Fuel Injection System and its application to the rotary engine have progressed in three areas: development of expertise in system operation and spray visualization, introduction of injection system to the rotary engine, and in on going communication with BKM, Inc., the manufacturer of the fuel injection system being used in these experiments. Each of these areas will be addressed in detail below.

2.1 Single Jet, Multi-Jet Fuel Nozzle Results

The BKM Serojet Fuel Injection System is now operational in the MSU Engine Research Laboratory. Two visualization studies have been conducted and their principal results are principally in the film/video tape. These studies involve the use of the copper vapor laser synchronized with the high speed camera to visualize the spray characteristics of the injector. The experiments were conducted in ambient air. An aluminum fixture was constructed to hold the injector firmly in place, thus eliminating injector position variations caused by vibration transmitted along the fuel supply line. A suction vent, 10 cm in diameter,

was placed approximately 30 cm downstream of the nozzle tip to remove the fuel spray after it had passed out of the area of interest. This "area of interest" was defined by a sheet of light generated from the copper vapor laser approximately 1.5 mm thick, 100 mm wide, with power of 40 watts, positioned parallel to the injector body. The pulse width of the laser was 30 ns. The laser was externally triggered synchronously with a Nac E-10/EE 16 mm high speed rotating prism camera operating at 5000 Hz. The experiments were conducted with odorless kerosene injected with both a 1-hole nozzle tip and a 6-hole nozzle tip.

The injector was specifically designed by BKM so that the nozzle tip could easily be replaced. Though there were some problems early in replacing nozzle tips, the valuable assistance provided by the BKM technical staff has allowed these problems to be overcome.

The rationale for performing these experiments in ambient air, rather than in the rotary engine was three-fold. First, for future in-engine tests it was necessary to develop and establish the visualization technique using the copper vapor laser sheet and the high speed camera. Second, it was necessary to establish whether any event to event variability occurred for the injection process. Finally, it was necessary to confirm or dismiss the presence of large trailing droplets. While it is recognized that the flow and decay patterns observed in these experiments are not typical of those which will be found in the rotary engine application, some important observations can be made.

Both experiments were conducted with the same operating conditions:

Ambient Pressure:	1 atmosphere
Rail Injection Pressure:	700 psi
Energize Time:	8 ms
Injection Frequency:	100 Hz

The sprays formed by the two different nozzle tips are very different in structure, but the injection processes have some similarities. The visualization of the 1-hole nozzle tip injection shows that the injection event may take on any one of three distinct patterns. Approximately fifty percent of the injection events behave as a jet of diameter 1.6 mm traveling at 180 m/sec which gradually grows to 5.0 mm in diameter over a distance of 4.4 cm, then quickly spreads out to a diameter of 2.2 cm and maintains this diameter for 7 cm. In the initial spreading of the jet there appears to be little interaction with the surrounding air, while in the constant diameter region good mixing and air entrainment is seen. The main injection event lasts for approximately 2.0 ms, after which several large droplets of diameters approximately 0.5 to 1.5 mm are expelled over a period of 0.4 ms. This pattern is shown in Figure 2-1.

The second pattern identified, shown in Figure 2-2, occurs for approximately twenty percent of the events and behaves similarly to the first pattern, except that no large droplets are expelled. The third pattern, occurring in approximately thirty percent of the events and shown in Figure 2-3, begins identically to the first pattern, but the injection ceases at 1.4 ms, followed immediately by a second and smaller injection lasting for 0.6 ms.

For the 6-hole nozzle tip, the general form of the spray is a cloud that grows as the

ORIGINAL PAGE IS
OF POOR QUALITY

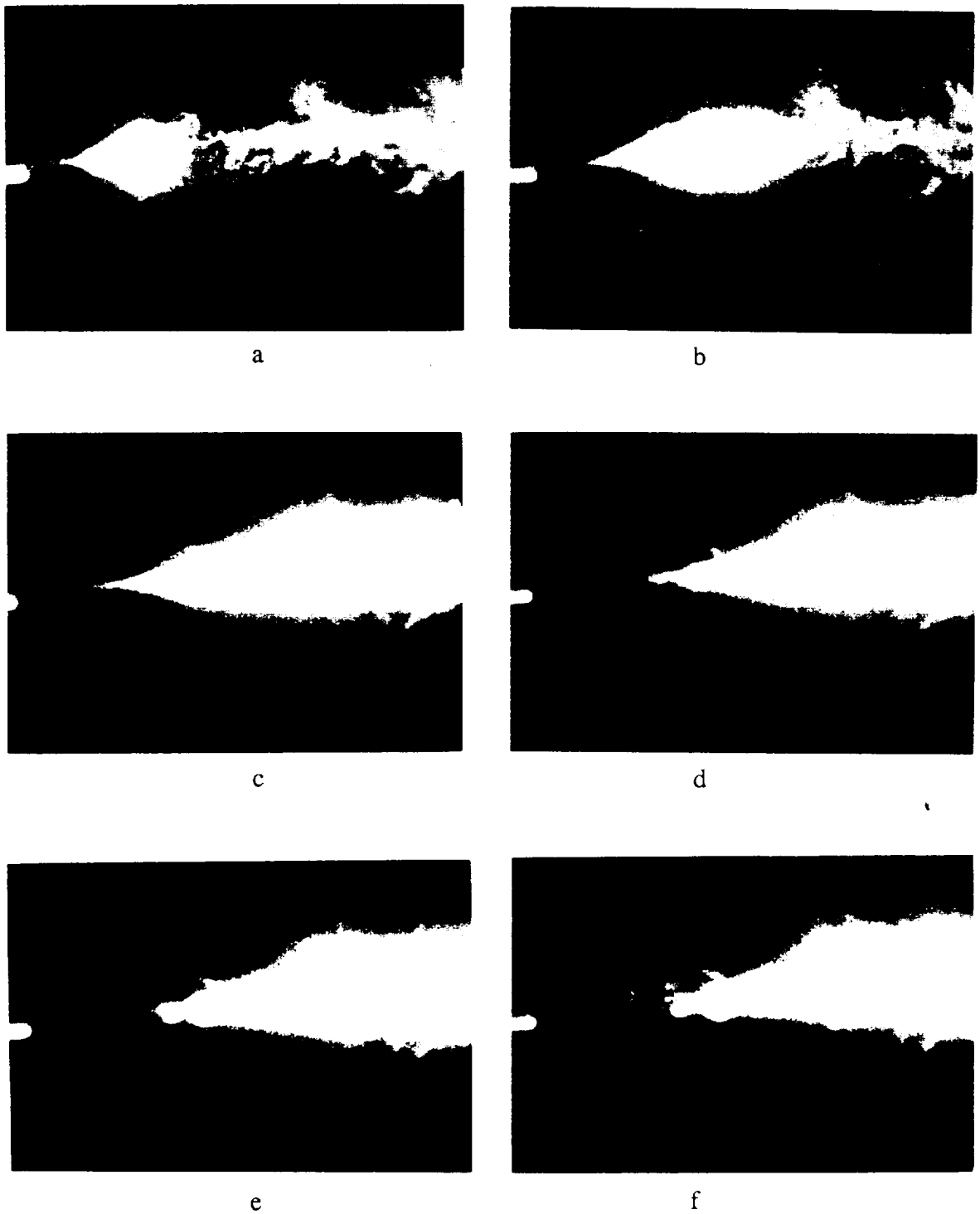

Figure 2-1 Single hole injection pattern with trailing droplets

ORIGINAL PAGE IS
OF POOR QUALITY

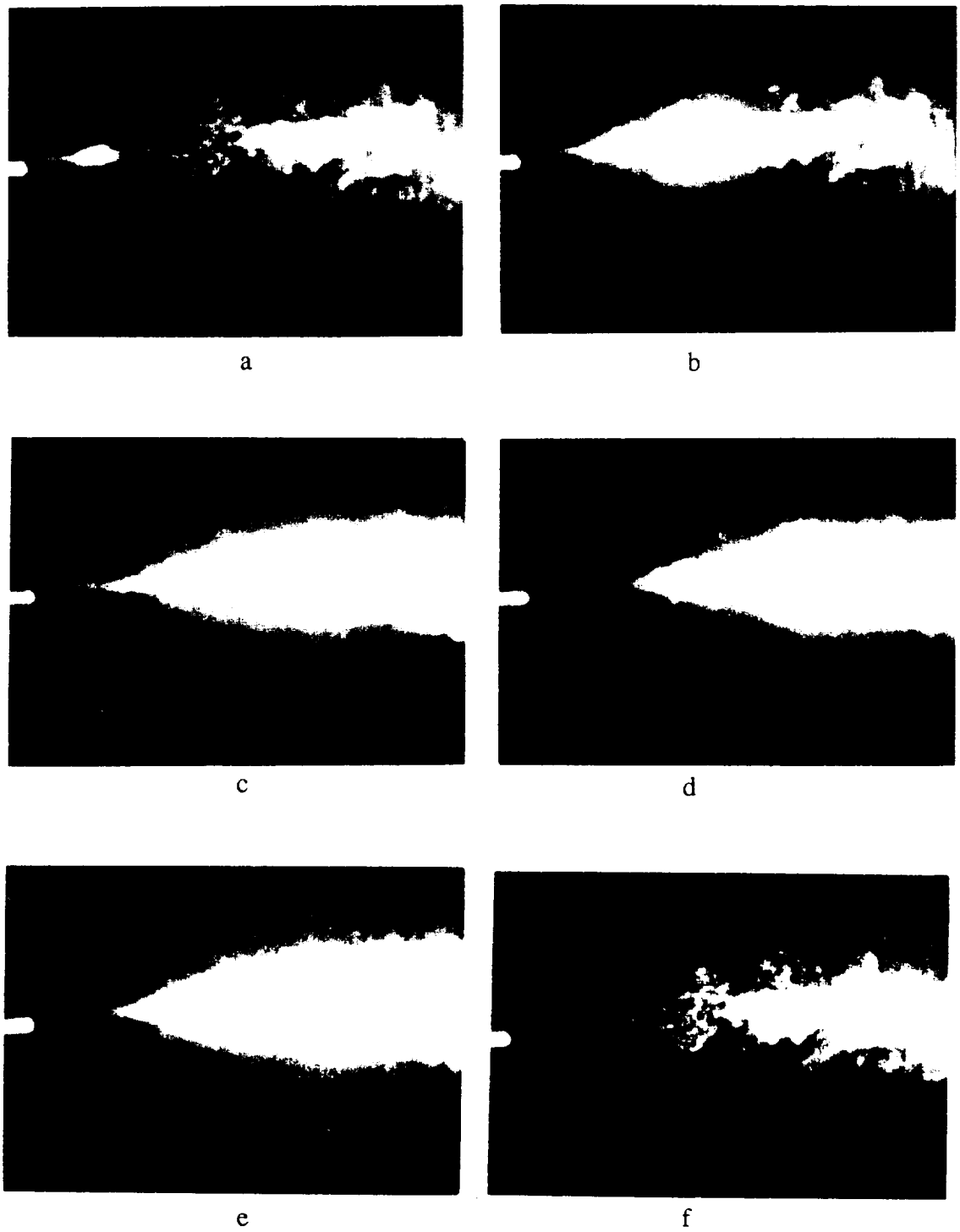

Figure 2-2 Single hole injection pattern without trailing droplets

ORIGINAL PAGE IS
OF POOR QUALITY

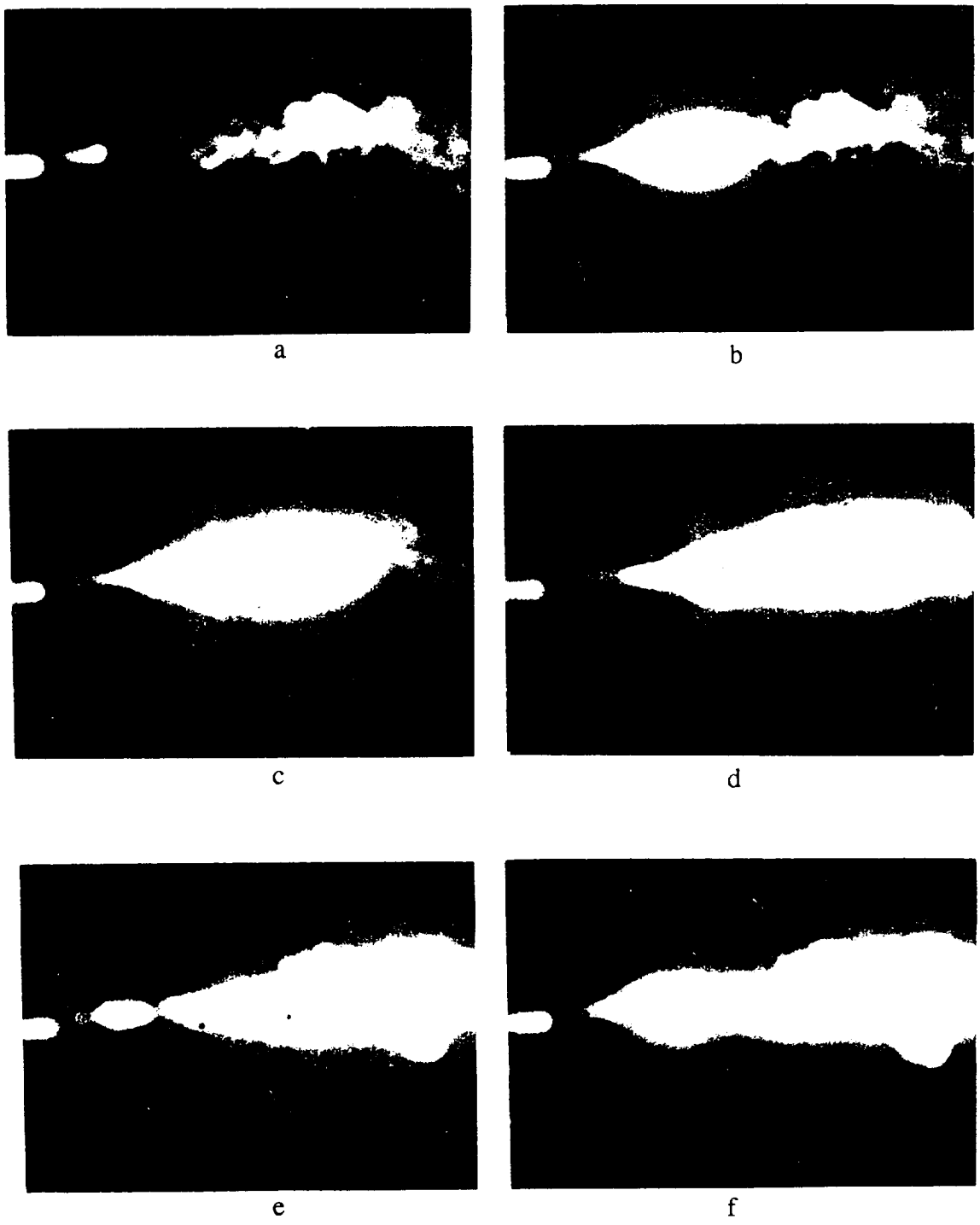

Figure 2-3 Single hole injection pattern with secondary injection burst

injection event proceeds. The process is much more complex than the single hole injection since in reality there are six single hole injections occurring and interacting with each other. Because of the complexity, it has not been possible to identify distinct patterns as in the case of the 1-hole nozzle, however, event to event variations still occur for the 6-hole nozzle. Figure 2-4 shows representative frames from two injection events. The second event is designated with a ('). In Figure 2-4(a) one sees a bright area near the nozzle tip which is the start of the injection event, labeled time = 0.0 ms. The first frame for each of the two injection events, Figures 2-4(a) and 2-4(a'), shows the remains of the previous event. Here large droplets are seen to follow the cloud of dense, small droplets. It is found that the main part of the injection event occurred in 0.6 ms with large droplets being expelled for an additional 0.6 ms. The presence of trailing droplets could lead to incomplete or late combustion, resulting in expressive emissions and poor performance. Continuing with Figure 2-4, frames (b) through (g) show the development of the fuel spray with time. As the photographs use the same scale and assuming that the scattered light is representative of the fuel mass, substantial spatial variations in the two injection events can be observed. One facet of these spatial variations is the observation that while there is flow from all six nozzle holes, these flows do not begin simultaneously. As about 8000 frames were examined, the phenomenon of non-simultaneous firings was found to occur regularly. Another important observation deals with mixing and air entrainment which occurs sooner for the 6-hole nozzle than for the 1-hole nozzle.

The complexity of the internal operation of the Servojet System has led to considerable effort exerted in developing a thorough understanding of its operation. Documentation of this effort can be found in Appendix A, which provides a detailed written account of Servojet Fuel Injection System operation.

The quantitative data given above for the visualization studies was obtained through measurements taken from the projection screen. This is a very tedious and somewhat imprecise method which has led to employing a digital image processing system specifically MegaVision. The availability of this system to the MSU Engine Research Laboratory provides a unique opportunity. Currently, sufficient expertise has been achieved to digitize a still photograph of an injection event and then appropriately process the digitized image. Photographs of interest can now be used to determine droplet position and size using the digitized image. Figures 2-5 (a),(b) and (c), show the original still photograph, the initial digitized image, and the processed digitized image. The next step is to use the MegaVision system to obtain quantitative information from the visualization experiments.

2.2 Design of Fuel Injector Assembly for RCE

A preliminary design has been finalized for mounting the fuel injector assembly onto the RCE. The injector assembly will be mounted directly onto the RCE housing. The injector nozzle will access the combustion chamber through the upper spark plug hole. The nozzle tip will be recessed so that no contact with the rotor will be possible. A compression gasket will be used between the first step of the injector and a machined step in the spark plug hole. The mounting mechanism of the injector assembly to the RCE housing will apply pressure to this gasket. The combustion chamber side of the hole will be machined to be slightly angled,

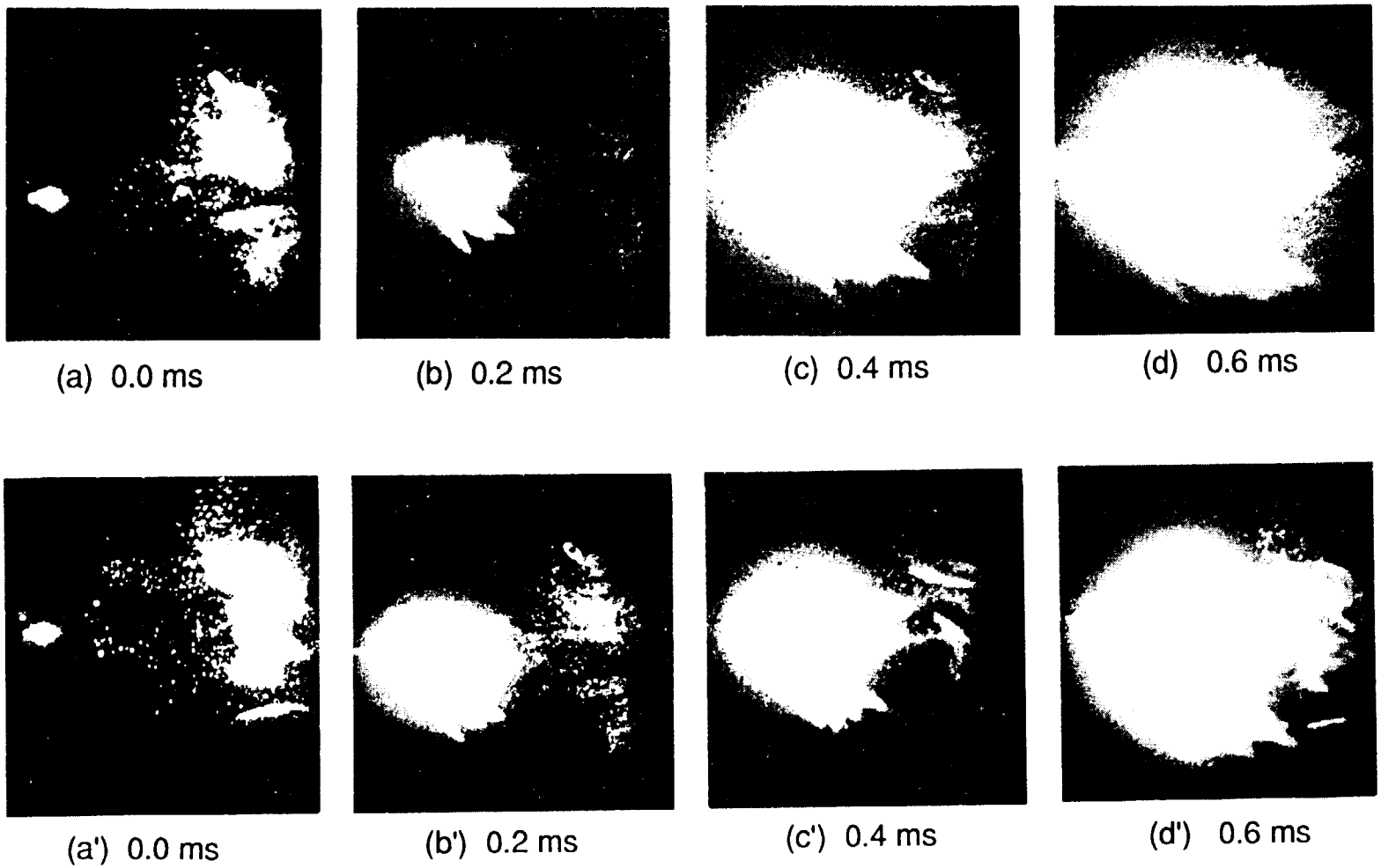

Figure 2-4 Sucessive frames in the development of two six hole injection events

ORIGINAL PAGE IS
OF POOR QUALITY

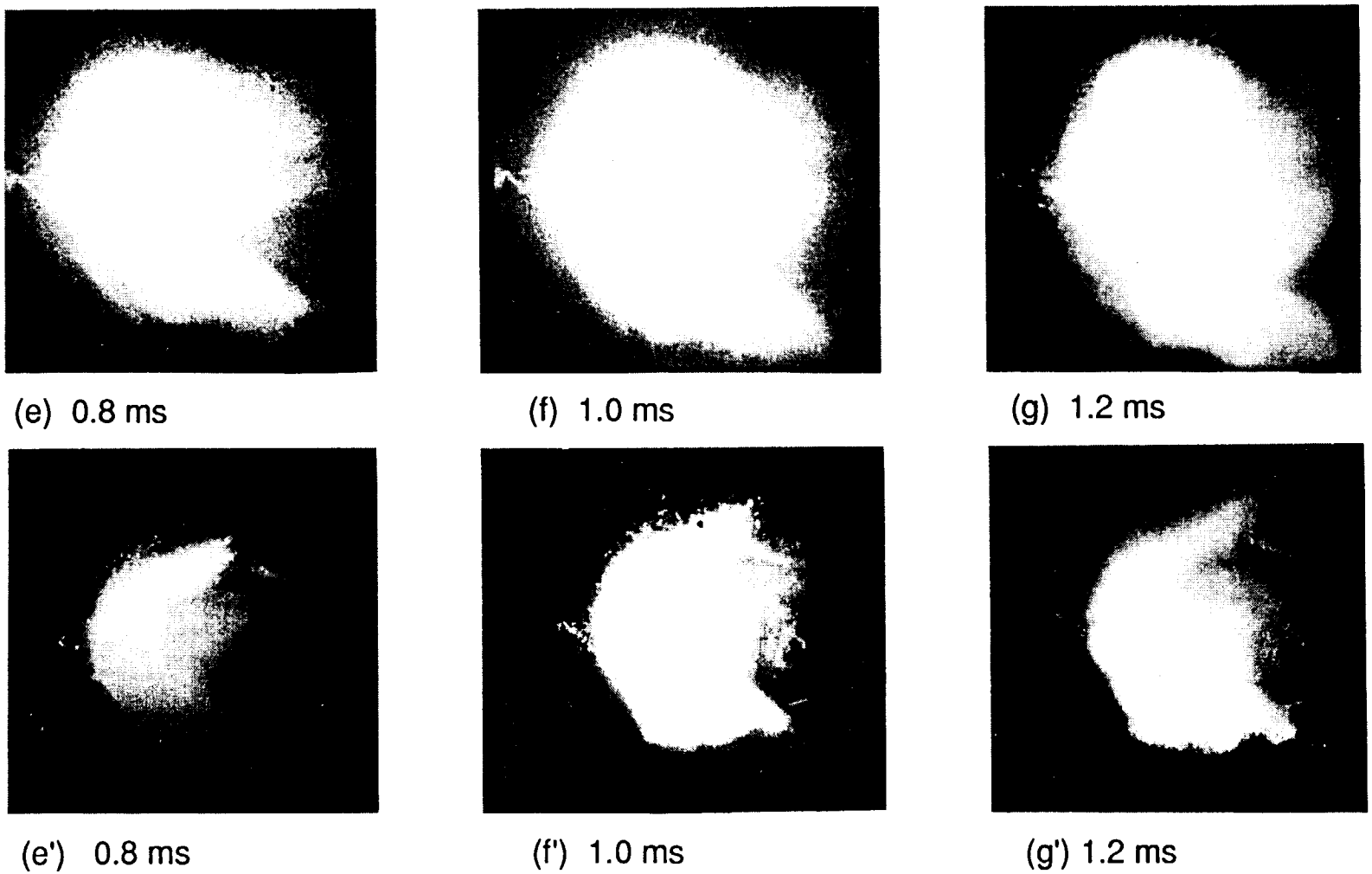

Figure 2-4 (cont.) Sucessive frames in the development of two six hole injection events

ORIGINAL PAGE IS
OF POOR QUALITY

ORIGINAL PAGE IS
OF POOR QUALITY

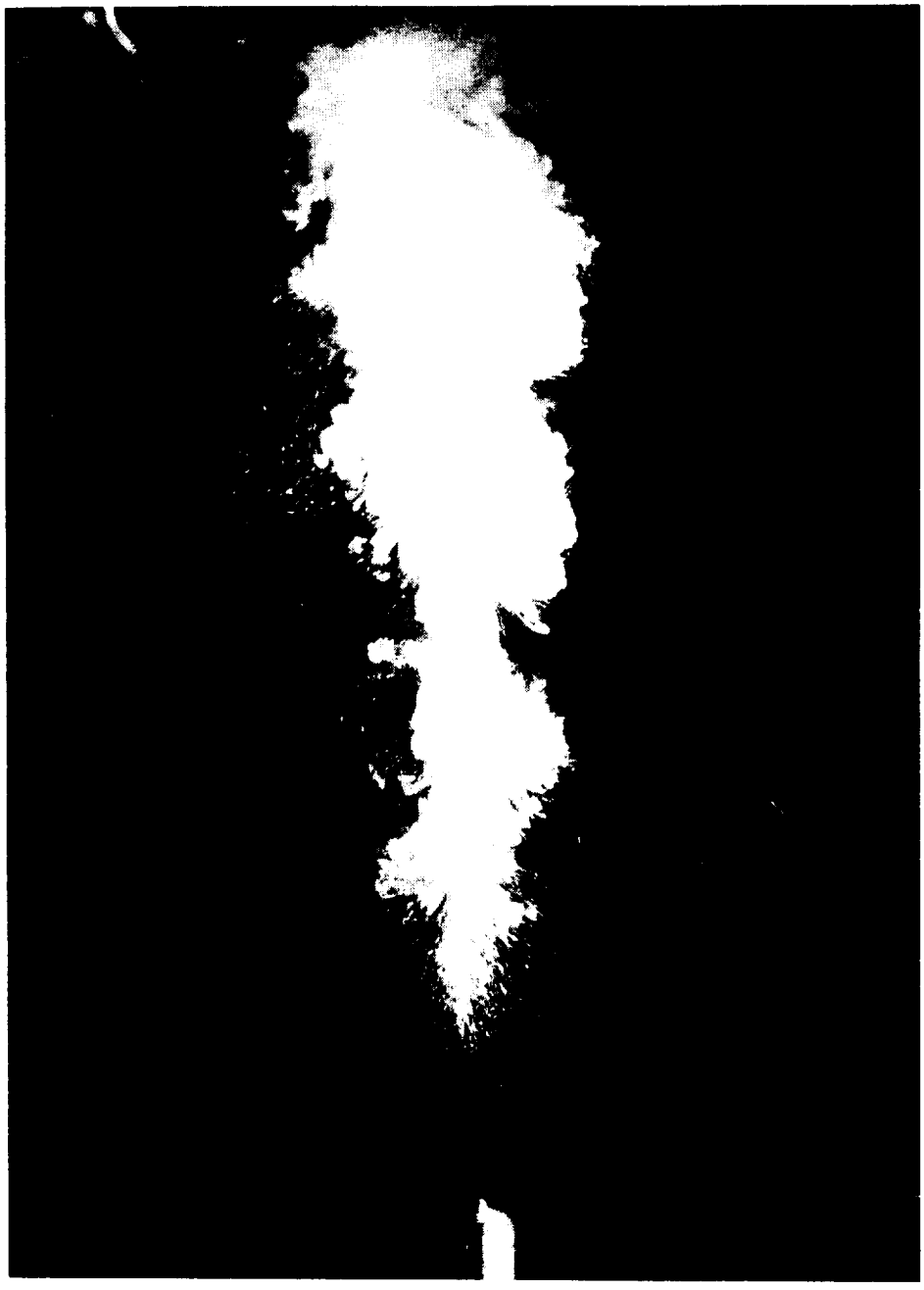

Figure 2-5(a) Original still photograph

ORIGINAL PAGE IS
OF POOR QUALITY

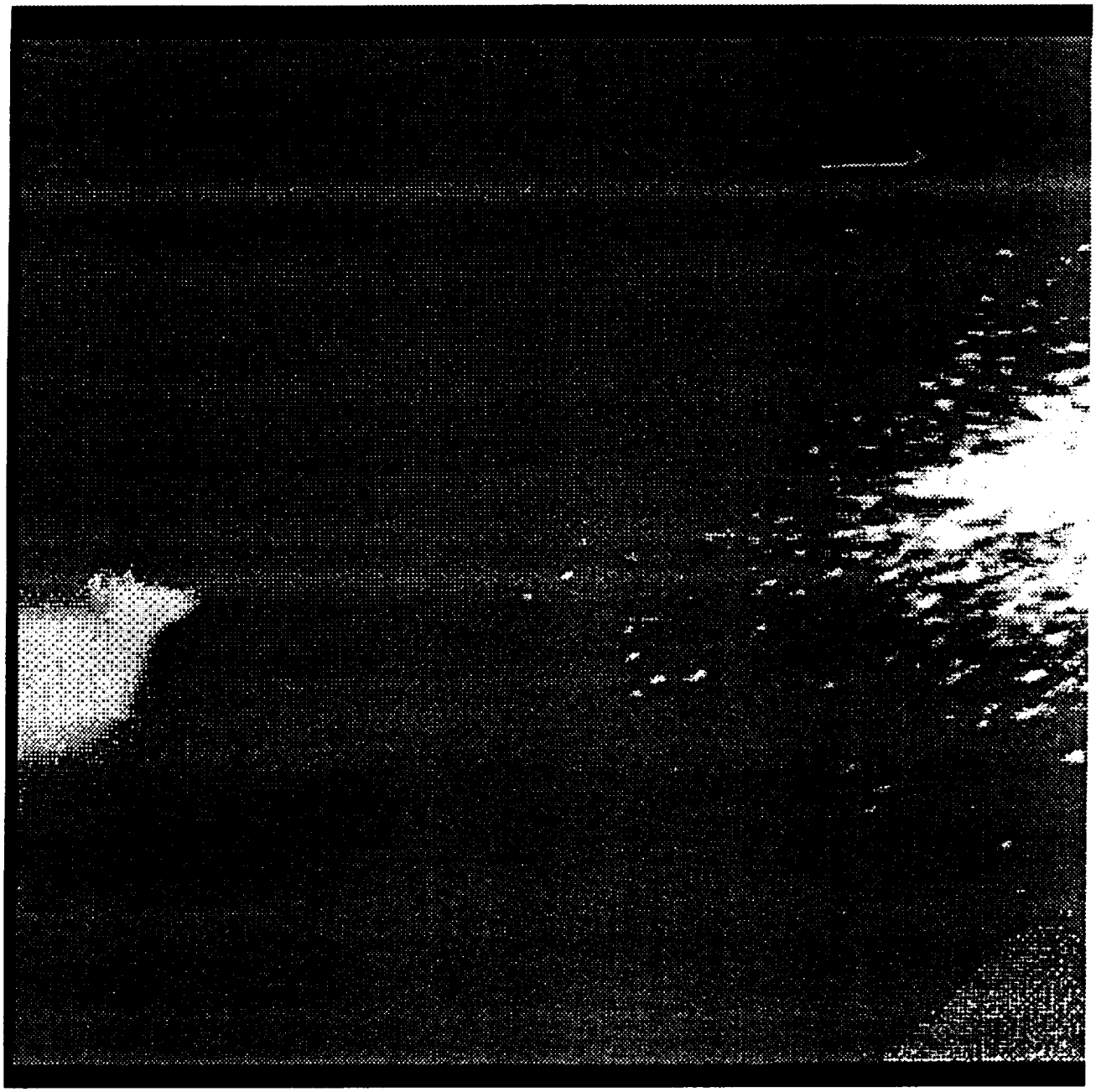

Figure 2-5(b) Initial Digitized Image

ORIGINAL PAGE IS
OF POOR QUALITY

Figure 2-5(c) Processed Digitized Image

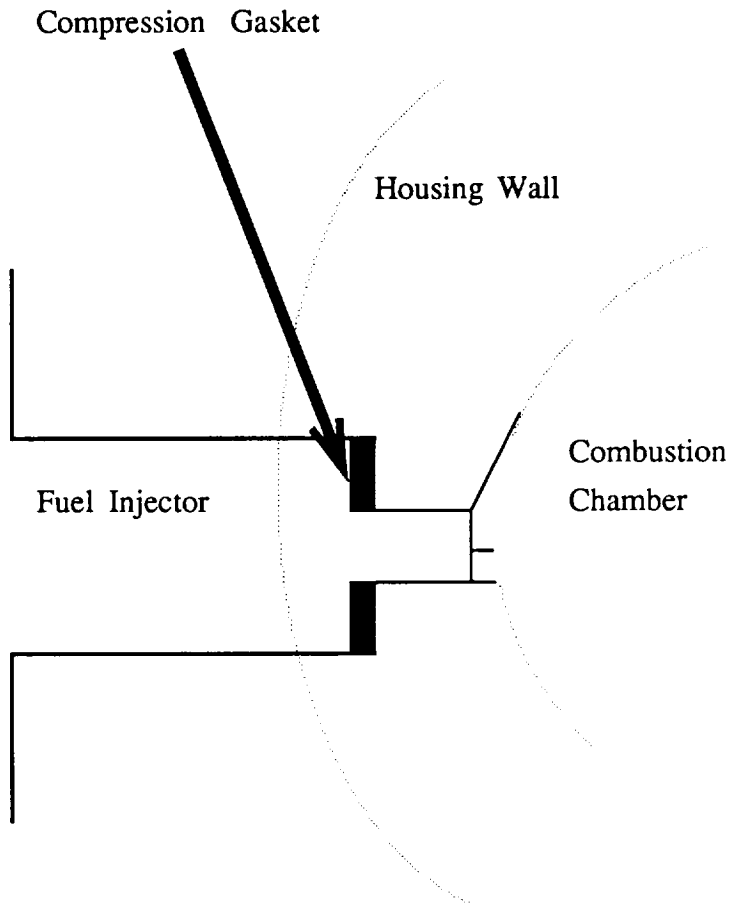

Figure 2-6 Fuel injector assembly attachment on rotary engine

as shown in Figure 2-6, so that fuel may be injected upwards into the down moving air stream. Nozzle tips with angled holes will be employed so that fuel may be injected at various angles to the airstream.

2.3 Interaction with BKM, Inc..

As noted in Section 2.1, when problems arose with the operation or maintenance of the Servojet Fuel Injection System, BKM, Inc., the manufacturer provided excellent technical assistance. The technical staff at BKM, including its president John Beck, has been helpful and very responsive to requests. Current discussions on technical aspects have benefited both parties and an information exchange path has been established. Observations provided on the operation of the BKM Servojet Fuel Injection System such as event to event variability and the presence of trailing droplets are not intended to be critical of the system, but rather findings of technical interest. The experiments have been conducted with only the BKM system and hence, no judgement on its operation in an engine can be fairly made without comparison studies with other systems.

2.4 Planned Work

By the end of summer, it is anticipated that the fuel injector assembly will be mounted onto the RCE and preliminary visualization tests will be conducted. A copper vapor laser sheet will be brought down through the central housing window. The high speed camera will record the visualizations through the upper side windows. By coupling the injector controller with the engine controller, injection timing can be controlled and various cases of timing can be studied. Similarly, the influence of injection angle, that is, the angle between the injection jet and the air stream, can be studied. It is anticipated that variation of these two parameters, timing and angle, in the visualization experiments will lead to some conclusions regarding control of the fuel distribution. Critical to developing these conclusions will be continuing efforts using the digital image processing system. It is anticipated that during the fall the injection visualization studies will be quantified through the use of image processing.

3.0 FLOW VISUALIZATION IN THE MOTORED SCRE

3.1 Experimental Facilities and Equipment

3.1.1 Rotary Engine Assembly

The rotary engine used in this study is a Mazda 12A engine. The engine apex and side seals are replaced by graphite seals in order to run the engine without lubrication except by the seeding which is used for the Laser Doppler Velocimetry (LDV) or for the flow visualization. The bearings are replaced by oil impregnated brass sleeve bearings. Optical access is provided by mounting sapphire windows on the sides and the housing of the engine. Further details and layout of the rotary engine assembly are given in Appendix B (Figure 1).

3.1.2 Flow Visualization System

The high speed flow visualization system developed for this study is shown in Figure 2 Appendix B. It consists of a 40-watt copper vapor laser (CVL), Model 451, a high speed camera, NAC E-10/EE, an electronic synchronization timing system, mirors, cylindrical lenses and a particle generator. The E-10/EE is equipped with a trigger pulse generator and optical pick-up to trigger the copper laser at 5 kHz and synchronize action with the film frame rate at 5000 frames per second (fps). Further details of the system and the experimental procedure were reported in our previous studies (Appendix B).

3.2 Results and Discussion

Section 3.2 presents flow field analysis under two conditions: naturally aspirated and supercharged conditions at 525 rpm. The entrained fluid is seeded by using di-octyl phthalate (DOP) through the induction system generated by an atomizer. A series of photographs selected from two 16mm high speed motion pictures filmed at 5000 frame per second (fps) will be presented to facilitate understanding of the fundamental aspects of the flow patterns in the intake and the compression cycles.

3.2.1 Flow Study In a Naturally Aspirated Rotary Engine(NARE)

In a naturally aspirated rotary engine, Figures 3-1(a) and (b) illustrate the flow pattern at 525 rpm during the intake-exhaust ports overlap, where the intake and exhaust pressure are at ambient condition. The air flow rate through the engine was measured at 6 cubic feet per minute (cfm). This set of figures indicate that the fluid is entrained by the velocity field generated by the rotor inward toward the rotor pocket. In this phase it is apparent that the flow is turbulent and it moves toward the leading apex where vorticity is generated and a counterclockwise circulation can be observed. Further in the intake, Figures 3-1(c) and (d) demonstrate the flow movement toward the boundary of the rotor housing, which is a consequence of the interaction between the rotor and the entrained fluid. Figures 3-1(e) and (f) show the instability of the entrained fluid near the intake due to the fluctuating pressure generated in the intake manifold by the rotor motion, and the blowby effect along the surface of the housing due to the leakage between the leading apex and the housing. Figures 3-1(g) and (h) show the flow field when the intake cycle reaches its maximum volume. In this event, it can be observed that the flow is moving in the direction of the rotor. However, this flow pattern will change at the end of the intake, and a subsequent flow reversal can be noted as shown in Figure 3-1(i) near the trailing apex as a result of the increasing pressure during the intake.

In the compression stroke at 525 rpm, it is apparent from Figure 3-1 that the vorticity generated during the intake is convected and diffused through the moving fluid. However, at the beginning of the compression the vortical structure near the boundary of the rotor housing is evident in Figure 3-1(a) and (b). Even so, some circulating flow can be observed later in the compression as demonstrated in the motion picture. This would imply that at higher speeds, this flow feature is reduced significantly when compared to the flow reported in Appendix B at 230 rpm. A special seeding technique is required which is currently being devel-

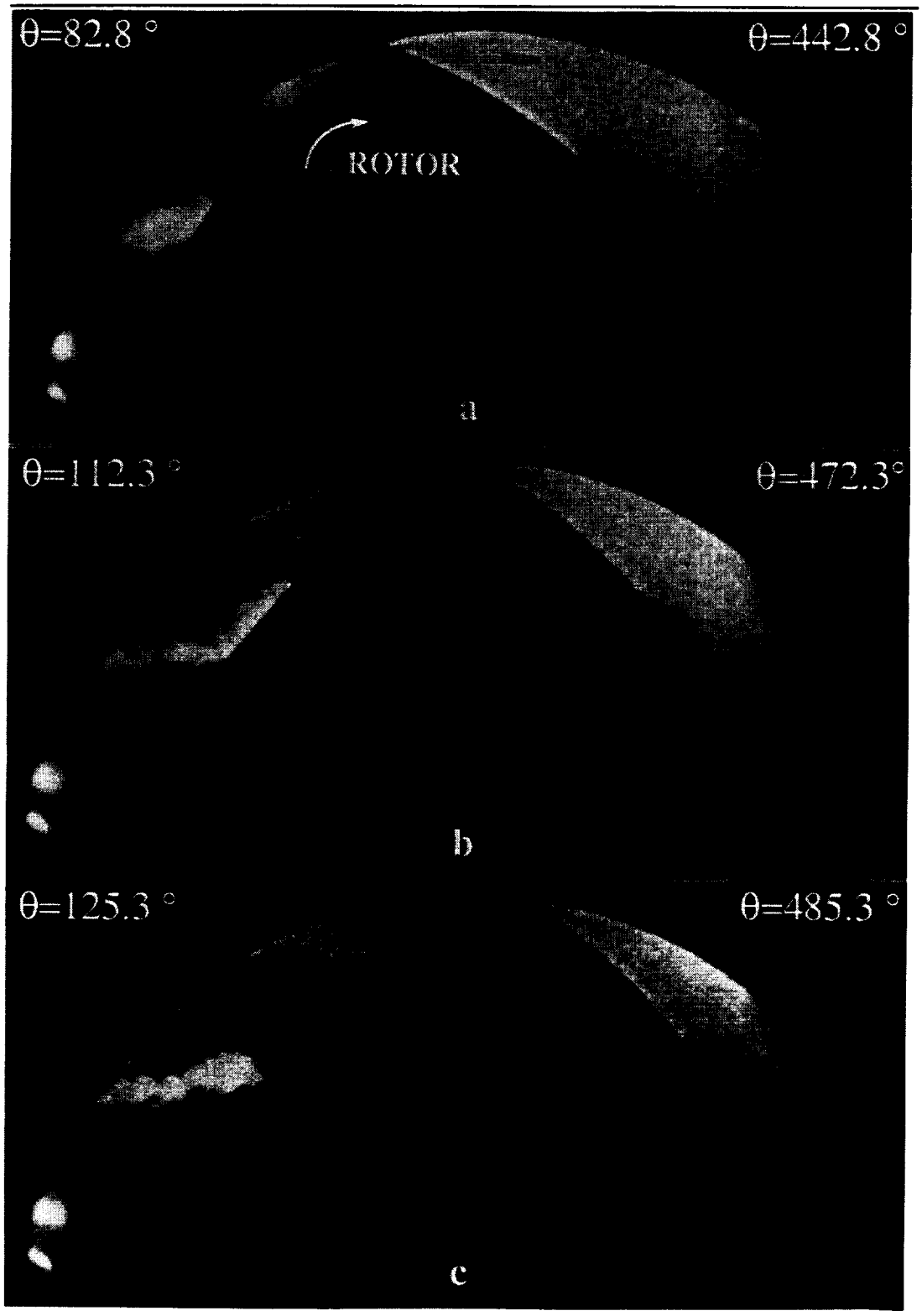

Figure 3-1 Flow pattern during intake and compression at 525 rpm in a naturally aspirated rotary engine

ORIGINAL PAGE IS
OF POOR QUALITY

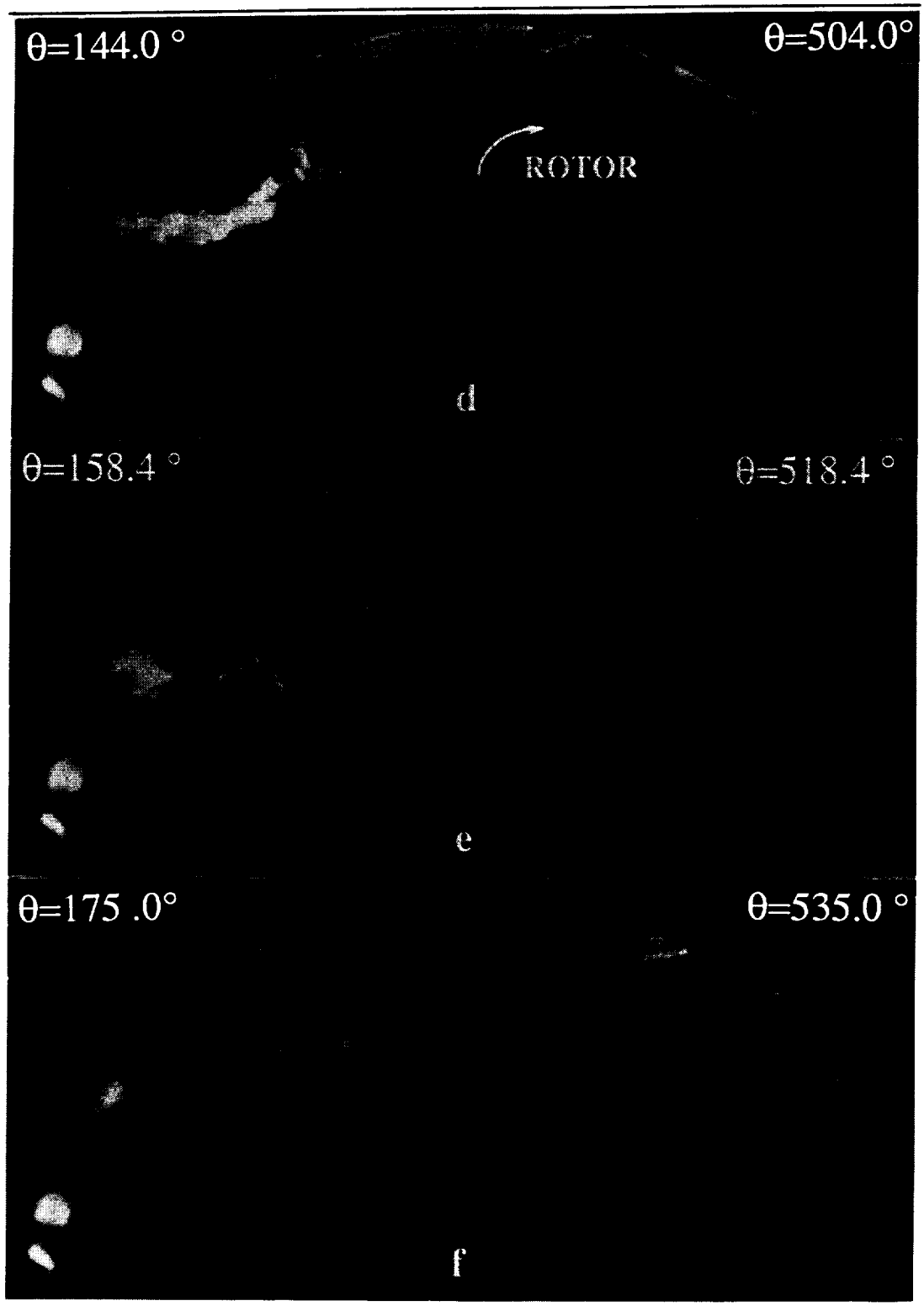

Figure 3-1 (cont'd.) Flow pattern during intake and compression at 525 rpm in a naturally aspirated rotary engine

ORIGINAL PAGE IS
OF POOR QUALITY

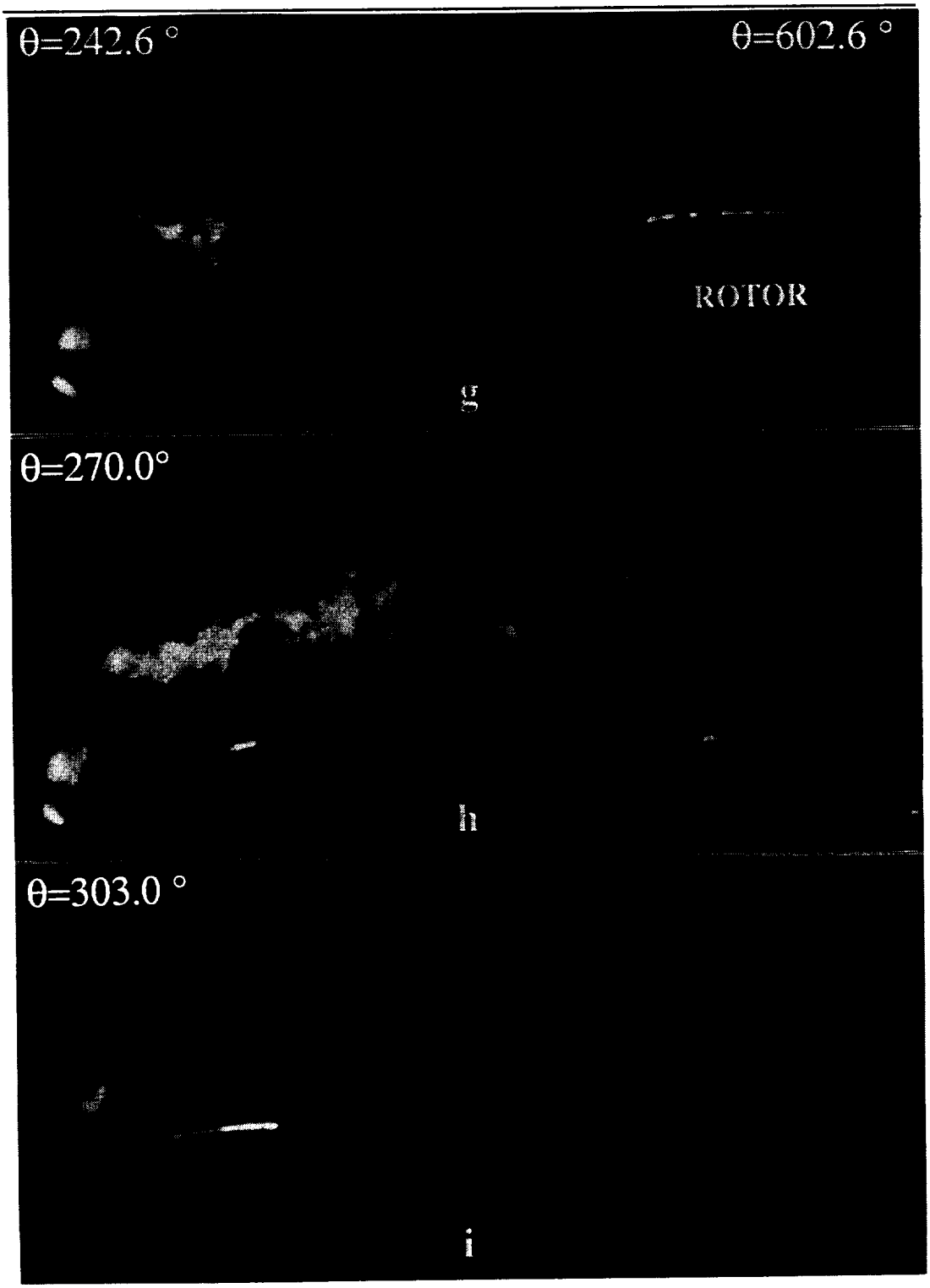

Figure 3-1 (cont'd.) Flow pattern during intake and compression at 525 rpm in a naturally aspirated rotary engine

ORIGINAL PAGE IS
OF POOR QUALITY

oped at the MSU Engine Research Laboratory.

3.2.2 Flow Study In a Supercharged Rotary Engine (SCRE)

In order to provide a comparison with the naturally aspirated configuration and clarity in interpretation of the LDV data a flow visualization of the supercharged rotary engine was conducted. The data presents an analysis of the flow field in a supercharged rotary engine at the same operating speed (525 rpm) and rotor positions as the previous analysis.

Figure 3-2 shows the flow development in supercharged rotary engine, at flow rate of 16 cubic feet per minute (cfm) and boost pressure of 41.0 " of water at selected crank angles during the intake. Figures 3-2(a) and 3-2(b) display the flow when the intake and exhaust ports are both opened. This overlapping of phases causes the flow in the intake to move toward the leading apex and the rotor where a clockwise recirculating motion is dominating the flow structure. This flow pattern is more clearly observed in the motion picture. The intake is a high pressure region relative to the back pressure in the exhaust. As the trailing apex proceeds toward the intake port it is evident from the motion picture and Figures 3-2(c),(d),(e) and (f) that the recirculating flow is in the counterclockwise direction and a strong rotating vortex is generated near the leading apex and the rotor. This fact is explained by the fluid blowby along the housing caused by the leakage between the leading apex and the housing which prevails near the vicinity of the housing, while some fluid is induced by the rotor. Clearly the complex flow structure depends markedly on the location of the rotor relative to the intake and exhaust ports and also on the direction of fluid flows through the induction system. In this regard, when the exhaust port is closed and the volume of the intake phase attains its maximum value as shown in Figure 3-2(g), the jet-like fluid flows through the intake manifold in the direction of the rotor motion and along the rotor surface towards the leading apex. However, before the fluid reaches the leading apex it changes direction to generate counterclockwise rotating vortex where the fluid moves toward the intake port in the vicinity of the housing. In this instance the fluid dissipates its energy. This subsequently leads to the formation of a stagnation zone later in the intake. Figures 3-2(h) and 3-2(i) clearly demonstrate the flow reversal and the manner in which the flow potential is reduced markedly when the trailing apex is half way through the intake port. This evidence is due to the pressure increase in the intake cycle and the exhaust port interference. Finally, in the intake, it is apparent from Figure 3-2(i) that when the intake port is almost closed, the fluid near the trailing apex moves in the direction of the rotor. However, the flow is relatively stagnant along the housing near the leading apex.

On the basis of the above discussion, it may be proposed that the position of the rotor relative to the intake-exhaust ports has the main influence on the flow and the vorticity generated in the intake. This is illustrated in Figure 3-2(a). Also, this figure shows the flow near the housing which constrained to move in the direction of the rotor. Moreover, this feature of the flow is clearly observed in Figure 3-2(b), where the fluid is driven by the rotor close to the trailing apex. Although Figures 3-2(a) and 3-2(b) illustrate the typical trend in which the rotor affects the flow field. Further in the compression it is interesting to note the clockwise recirculating flow pattern " roll-up vortex" at the surface of the rotor near the trailing apex as demonstrated in Figures 3-2(c) and 3-2(d). The general feature of the flow pat-

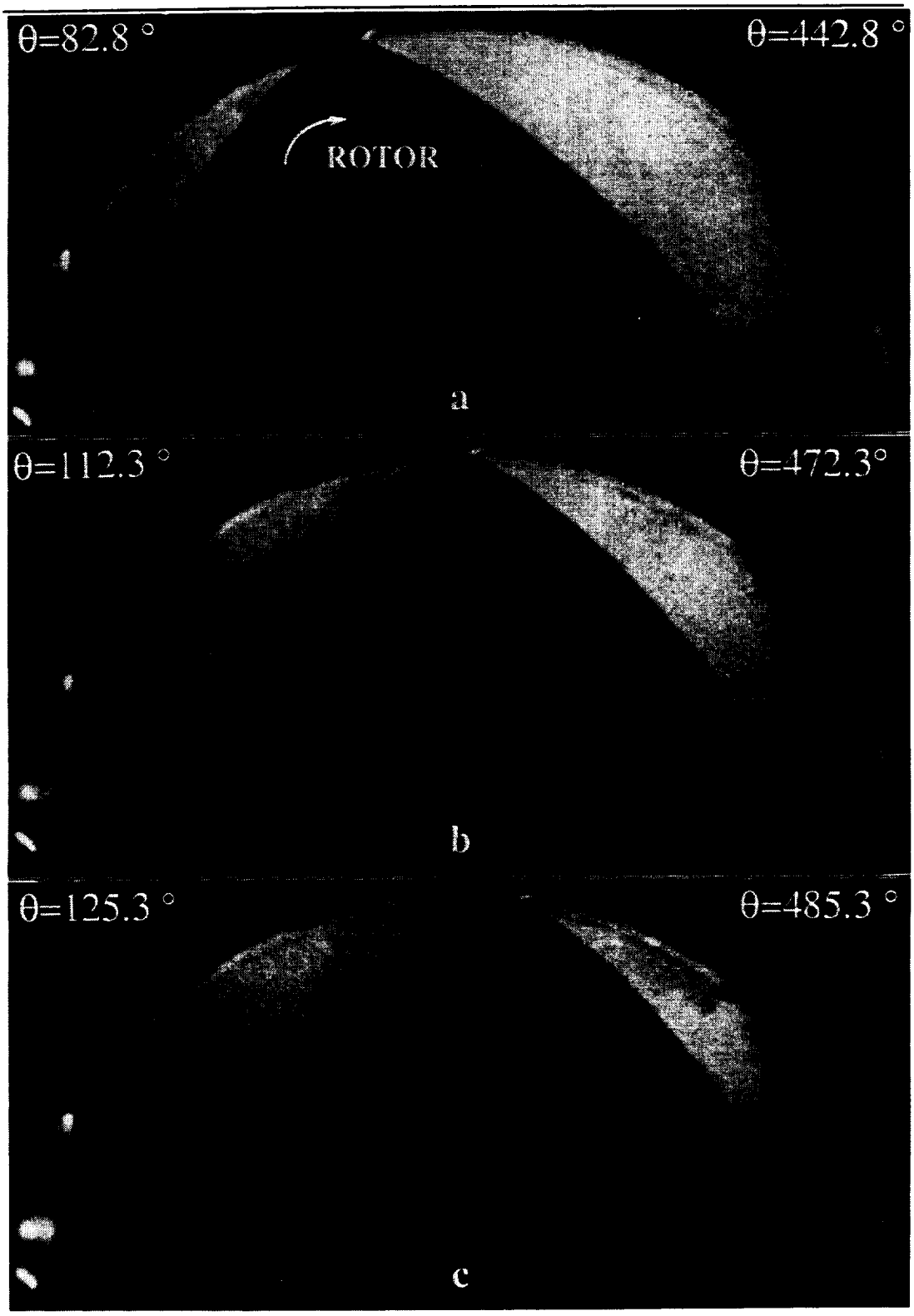

Figure 3-2 Flow pattern during intake and compression at 525 rpm in a supercharged rotary engine

ORIGINAL PAGE IS OF POOR QUALITY

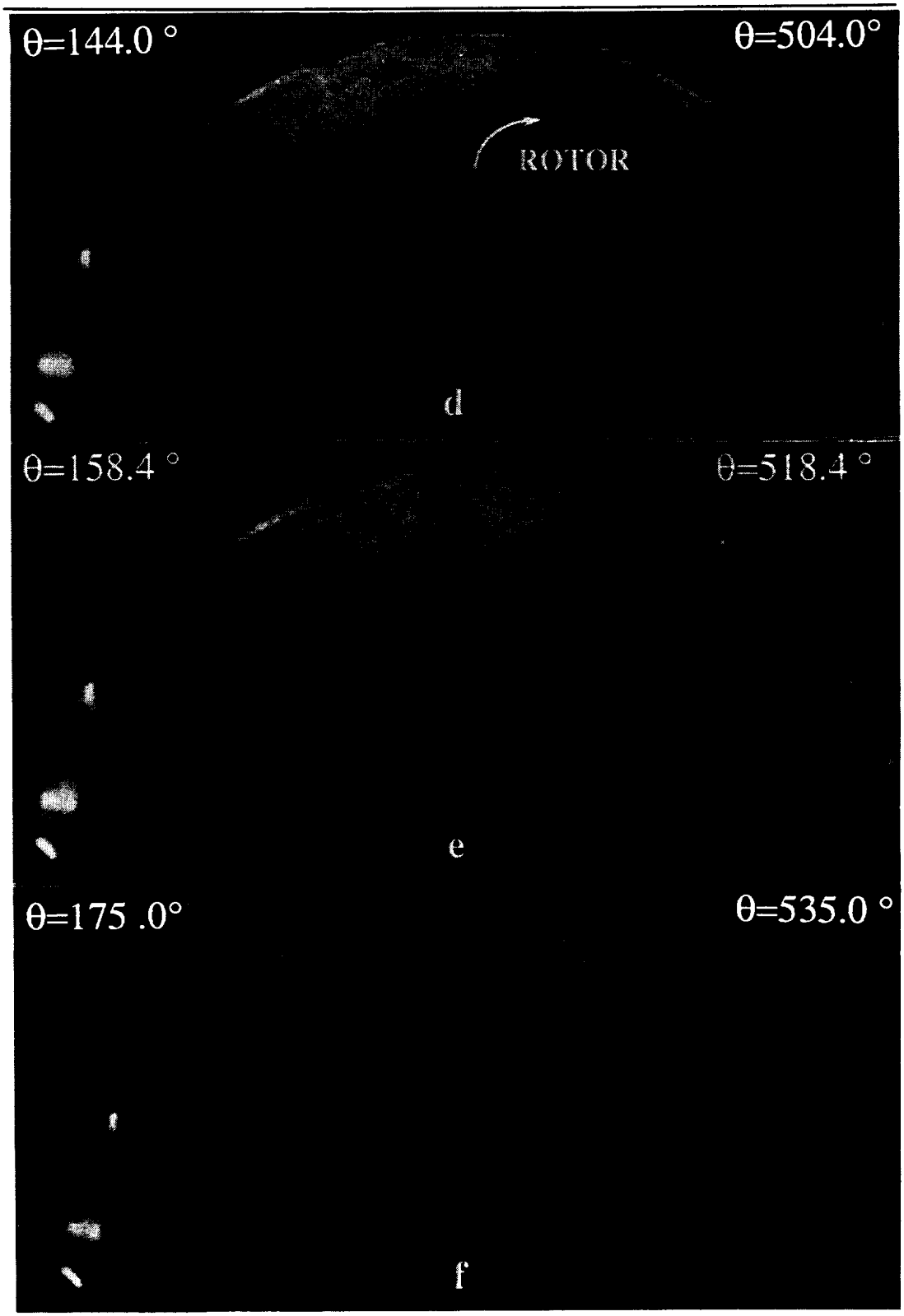

Figure 3-2 (cont'd.) Flow pattern during intake and compression at 525 rpm in a supercharged rotary engine

ORIGINAL PAGE IS
OF POOR QUALITY

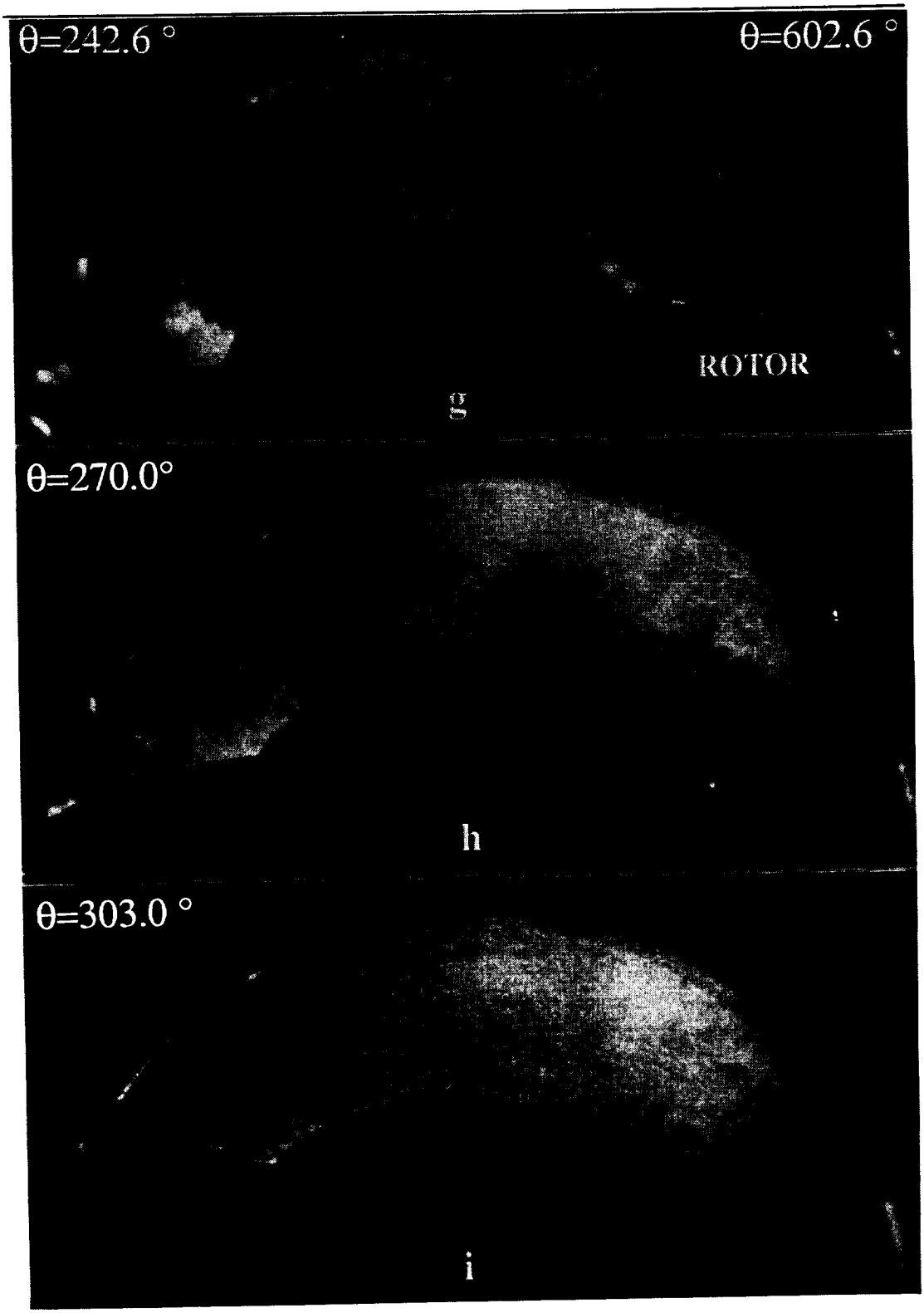

Figure 3-2 (cont'd.) Flow pattern during intake and compression at 525 rpm in a supercharged rotary engine

ORIGINAL PAGE IS
OF POOR QUALITY

tern is expected to maintain its structure further in the compression as indicated by Figures 3-2(e) and (f) and in the motion picture. However, more theoretical and experimental studies are required to confirm this aspect of the flow field at higher speed and for different rotor geometry, which in turn may lead to improve the engine design chamber flow characteristics.

Finally, it is interesting to conclude this section with the following brief comparative remarks. First, in the intake it is quite evident that the level of vorticity generated in the supercharged engine is higher than that in the naturally aspirated engine, which in turn exhibits to enhance the turbulent flow pattern in the compression stroke. Second, the flow reversal is reduced in the supercharged engine. However, the blowby along the surface of the housing is more distinct than that in the naturally aspirated engine. This flow feature is clearly demonstrated in the motion picture.

3.3 Planned Work

Progress has been made in demonstrating the controlling effects of the rotor and the induction-exhaust system on the flow behavioral pattern. Much is yet to be learned about the combustion chamber flow phenomena. Engineering applications will be greatly benifited by improved understanding of the flow structure at higher rotational speeds and for a wider range of boost pressures and mass flow rates. Presently, at the MSU Engine Research Lab, different types of seeding processes are understudy. A specifically designed particle generator with an electronically controlled solenoid valve has been designed and is under construction. This will be used in order to inject the seeding over a predetermined range of crank angles. This should provide a greater degree of stratification of seeded and unseeded air which in turn will provide greater contrast for photography.

4.0 LASER DOPPLER VELOCIMETRY (LDV) STUDIES

4..1 Status of LDV System

The Laser Doppler Velocimetry setup (See Appendix C for details) has been in production mode for approximately one month. During this time measurements have been made in nine locations in the motored RCE assembly. Three of these will be discussed in detail. The measurements were made under naturally aspirated conditions at a shaft speed of 500 rpm.

4.2 Description of Optics

The optical system is described in the figures. Figure 4-1 shows the optical setup. Figure 4-2 demonstrates the measurement volume and its dimensions.

4.3 Criteria For Acceptance of LDV Measurements

The data collected had criteria for acceptance as follows: The mean velocities had to compare reasonably well for two separate runs at different shifts (usually 5 MHz and 10

MHz). The histograms at locations where the flow is highly turbulent or highly negative had to be approximately Gaussian in shape (i.e. no low or high frequency cutoff). Also, an effort was made to assure that each encoder position (approximately 0.2 degrees) contained at least 100 good points, although at difficult locations, the number of good points was sometimes below 100.

4.4 Results in Intake and Compression

Measurements were taken at nine locations in the RE assembly. Figure 4-3 shows the three points labeled (A) , (B) and (C) which are of particular interest. The results of these measurements are described in detail. The crank angle position is referenced as previously discussed in Section 3.0, and is used consistently throughout this discussion.

The velocity measurements (mean and RMS) for location (A) are shown in figures 4-4(a) - 4-4(d). The flow visualization films for the naturally aspirated condition at a shaft speed of 525 rpm indicate that when the rotor is at 90 degrees and for a short period thereafter, the fluid flow is predominately rotor entrained and moving toward the rotor pocket. This is confirmed by the LDV measurements showing positive u and v mean velocity components. However the mean velocity components quickly become negative due to the counterclockwise vortical structures caused by the interaction of the blowby with the flow at the intake port. This vortical structure is accompanied by a sharp increase in the rms velocity. As the intake event progresses the blowby becomes less dominating, and over the crank angles of 195 to 220 degrees the flow again becomes entrained by the rotor motion. Here the flow moves toward the leading apex, until late in intake where it reverses due to the intake exhaust overlap. Late in intake a decrease in turbulence intensity is also apparent.

Figures 4-5(a) -4-5(d) show the velocity measurements for location (B) in compression at a shaft speed of 525 rpm. The v-component of velocity for these measurements is positive in the opposite direction of the rotor motion. The plots show that the flow beginning at 270 degrees quickly becomes diffused and convected and is "pushed" ahead of the leading apex. This results in a relatively steady velocity that fluctuates predominately due to rotor face orientation, changing with respect to a fixed reference. As compression progresses, the rms velocity decreases again indicating a dissipation of turbulence in compression.

Figures 4-6(a) - 4-6(d) show the velocity measurements during intake for location (b). The flow visualization film shows clearly that there is a substantial blowby due to fluid leaking past the apex seal. This observation was confirmed by the LDV measurements. For a short time after the rotor passes the control volume the flow is entrained by the rotor motion and is in the same direction as the rotor motion. However at that location the fluid velocity quickly rises in the opposite direction of the rotor motion and reaches a maximum velocity of 27 m/s in the v-direction near a crank angle of 180 degrees. As was previously discussed, as the intake progresses and the rate of change of the intake volume minimizes, the flow becomes entrained and moves with the rotor. The rms velocity indicates a high level of turbulence consistent with the action of a jet moving past the measurement location.

Figures 4-7(a) - 4-7(d) show the results for location (C) in compression. These

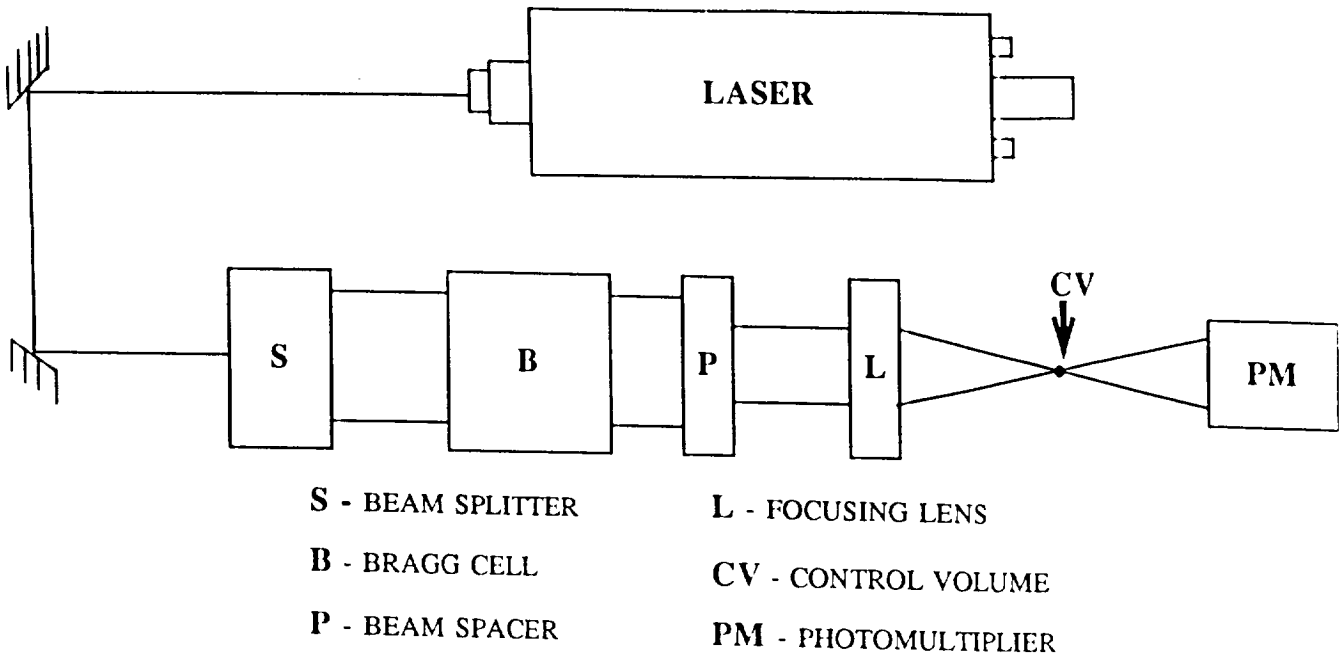

Figure 4-1 Optical setup

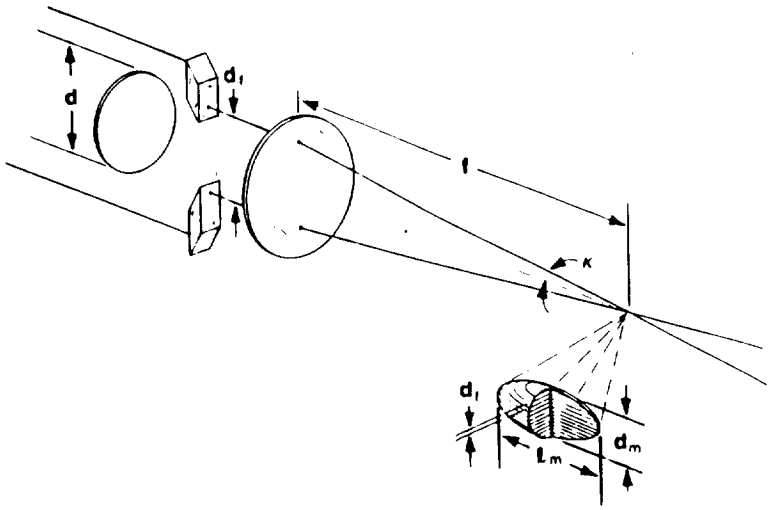

Figure 4-2 Measurement volume and dimensions

Model Number	f(mm)	d_m(μm)	Beam Separation Distance,d(mm) 22 Number of Fringes, N_{fr}(D_e-2 = 1mm) 28	
9118	250	164	d_f	6.12
			k	2.41
			l_m	3.89
			S_B	23

A- (x=81.2 mm, y=56.0 mm)
B- (x=114.6 mm, y=0.0 mm)
C- (x=108.4 mm, y=-37.1 mm)

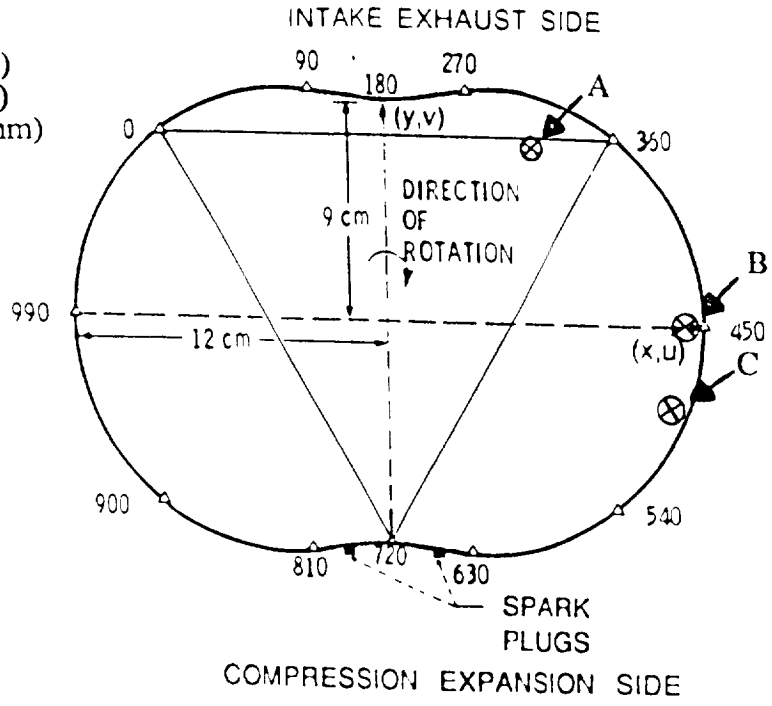

Figure 4-3 Rotor housing dimensions and measurement location

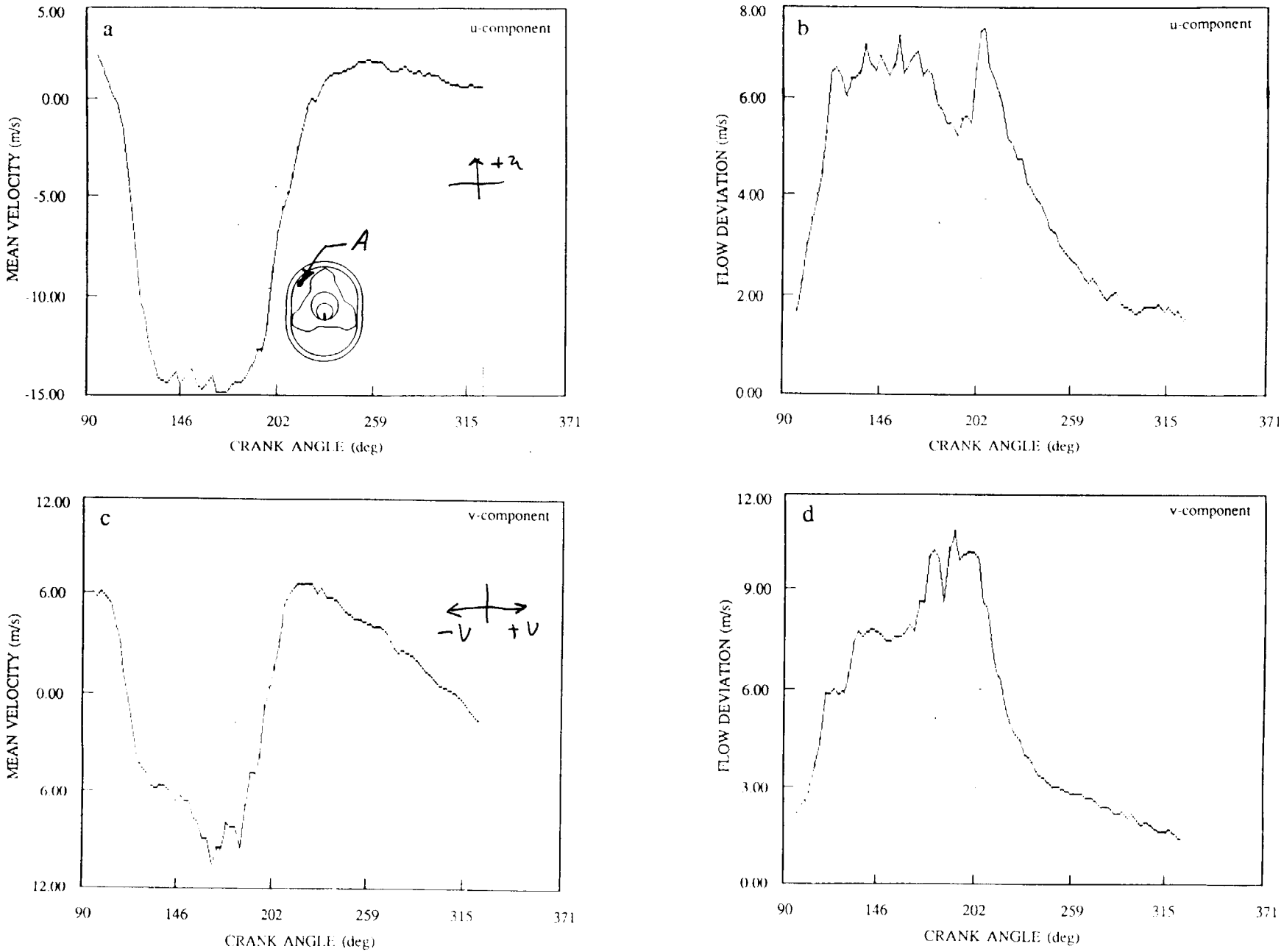

Figure 4-4 Velocity measurement during intake at 500 rpm at location (A) in a naturally aspirated rotary engine

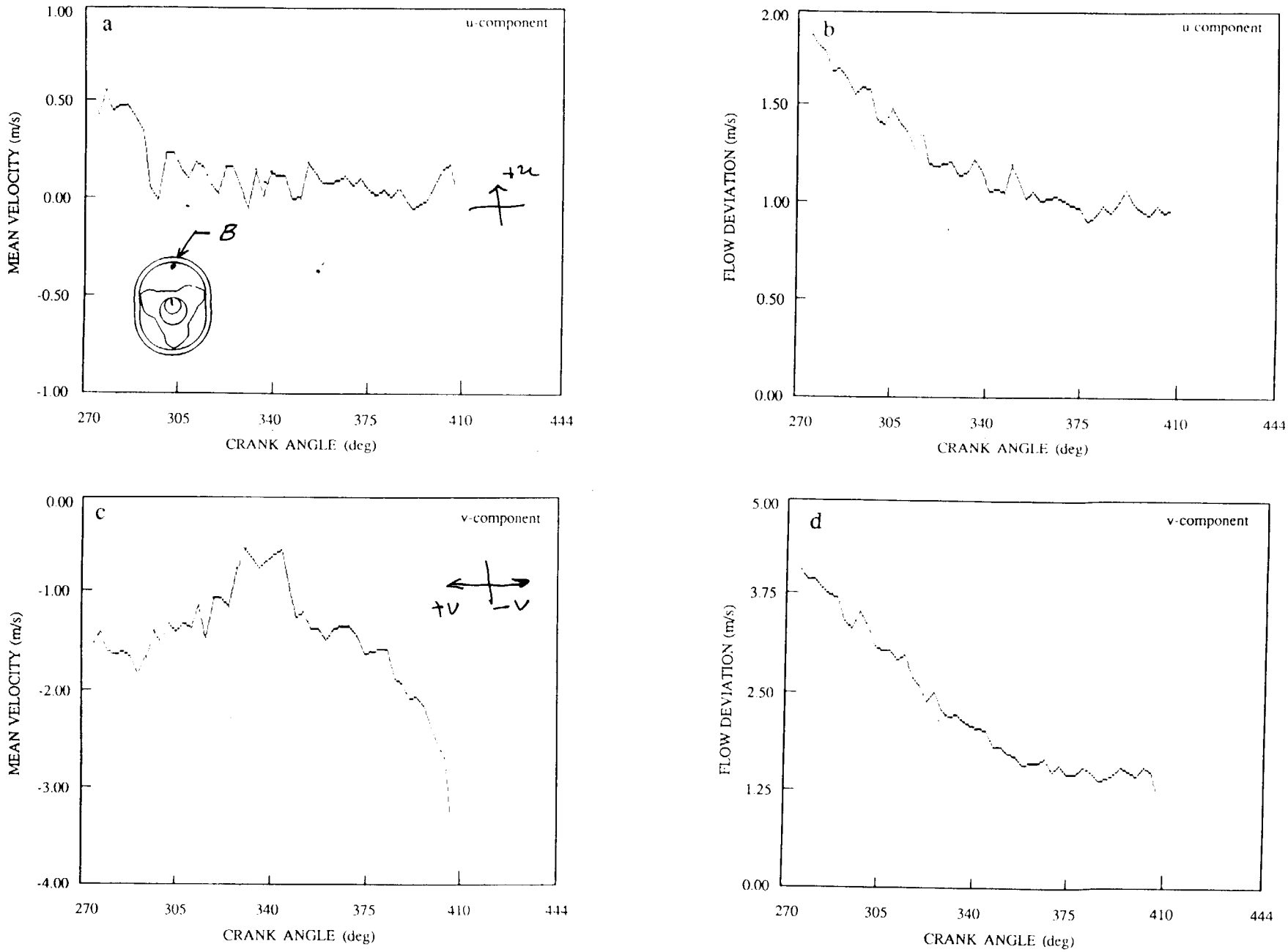

Figure 4-5 Velocity measurement in comperssion at 500 rpm at location (B) in a naturally aspirated rotary engine

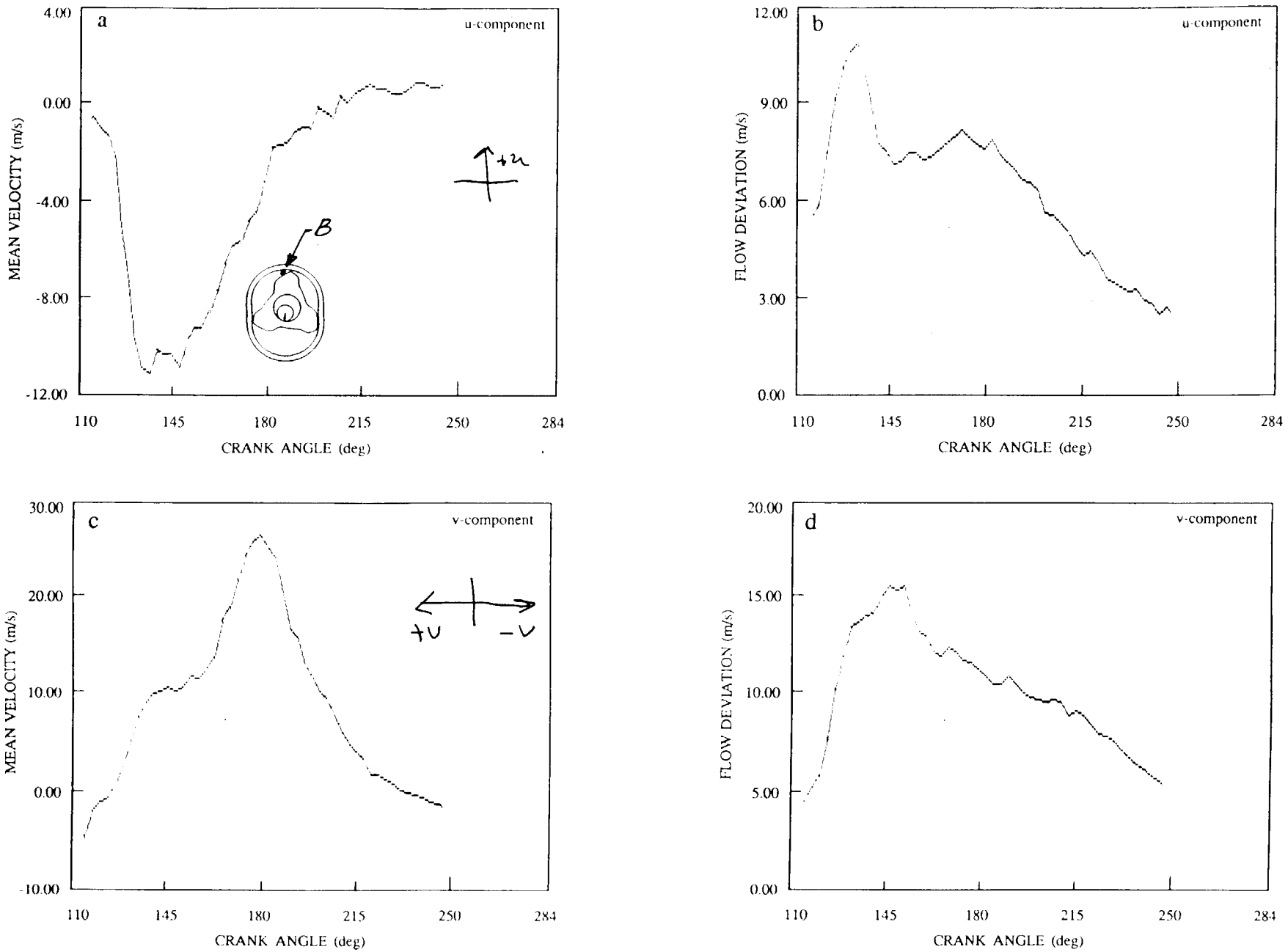

Figure 4-6 Velocity measurement during intake at 500 rpm at location (B) in a naturally aspirated rotary engine

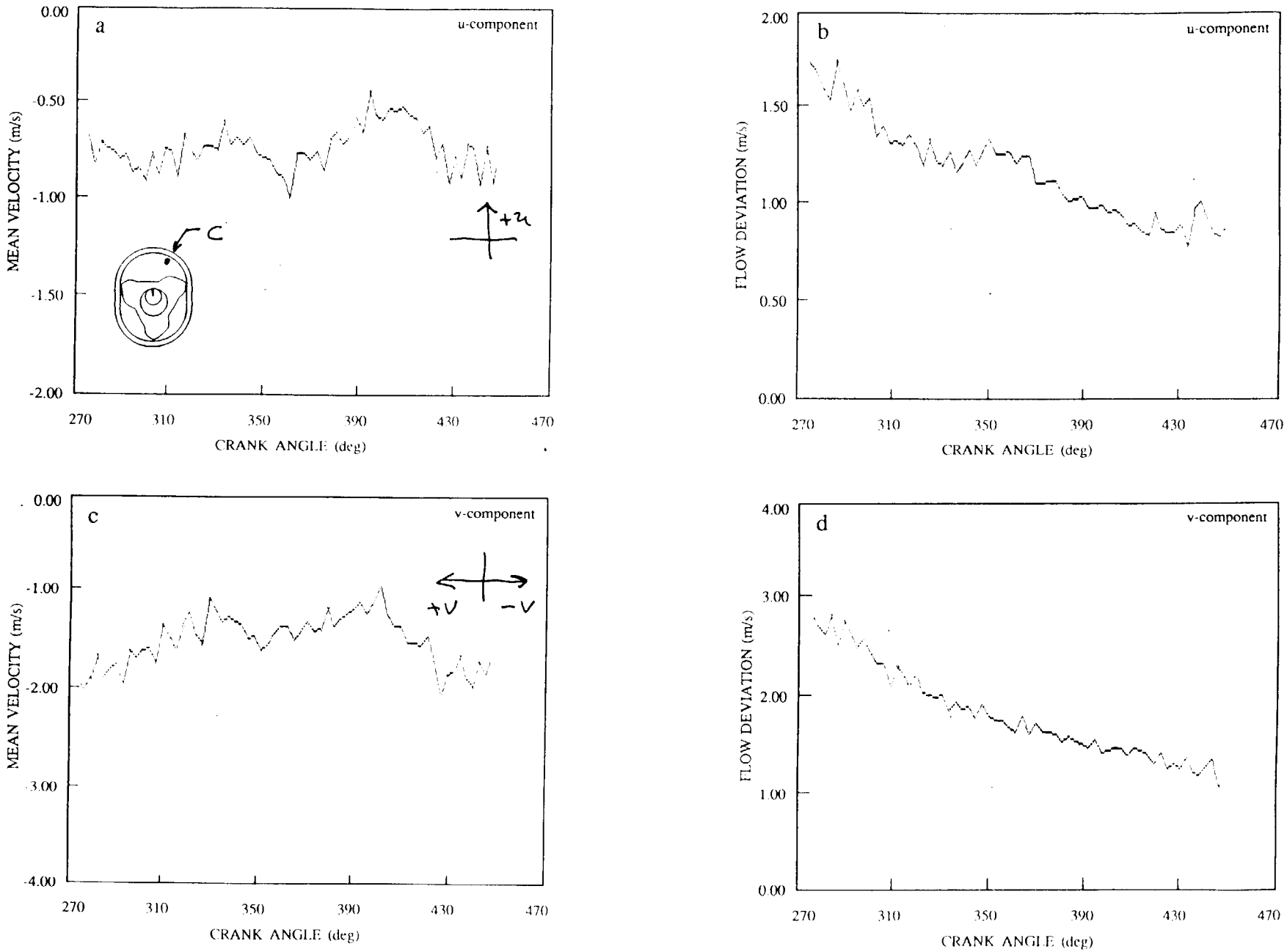

Figure 4-7 Velocity measurement in compression at 500 rpm at location (C) in a naturally aspirated rotary engine

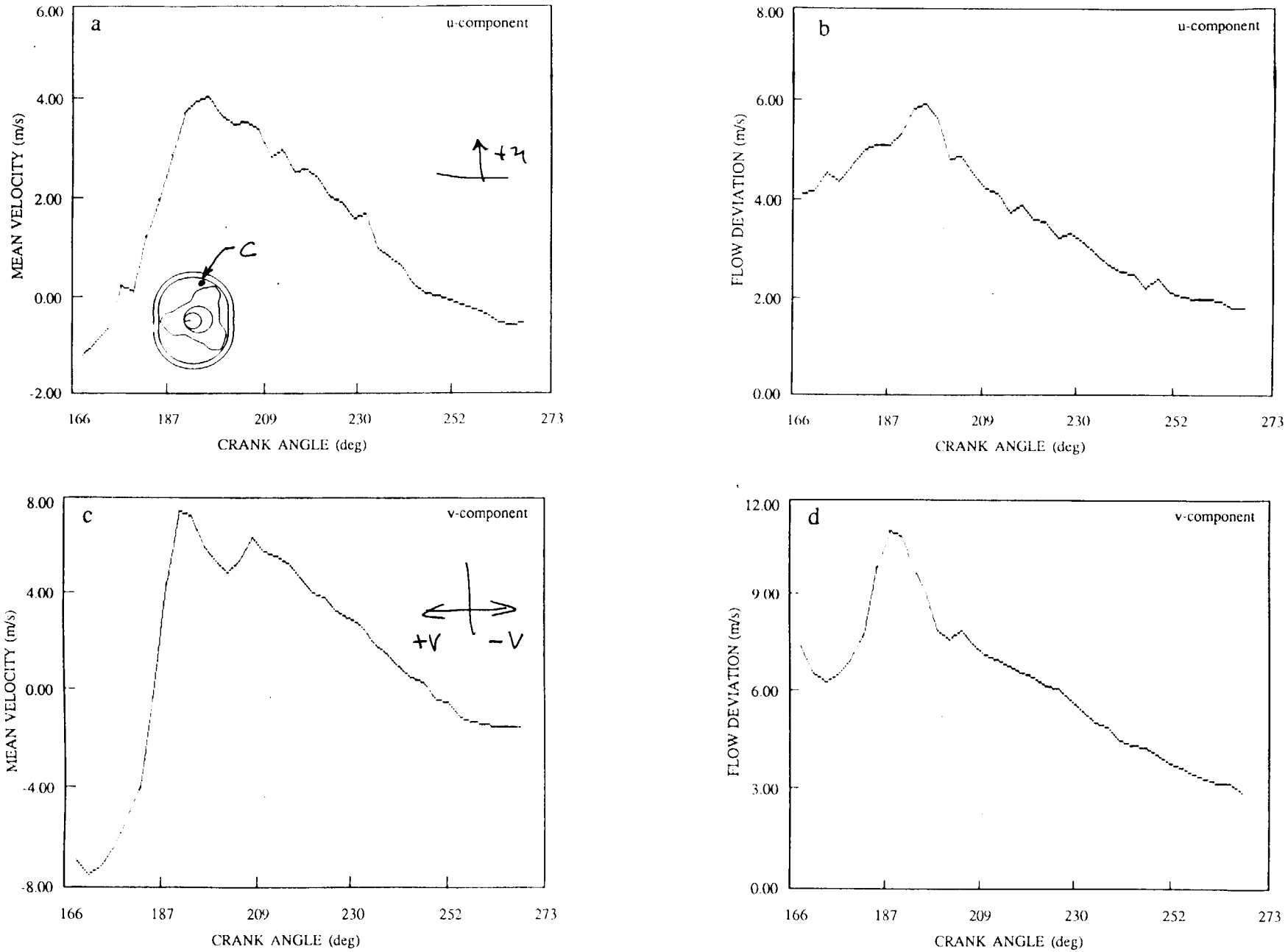

Figure 4-8 Velocity measurement during intake at 500 rpm at location (C) in a naturally aspirated rotary engine

plots again indicate that the compression cycle is dominated by " squish" flow that is pushed ahead of the leading rotor face. The u-component is now negative due to the leading apex passing the major axis.

The results for intake for location (C) are shown in Figures 4-9(a)- 4-9(d). The results are consistent with the results shown for location (B) in the intake. The blowby is clearly indicated and is the dominating feature close to the rotor housing.

4.5 Planned Work

The next step for the LDV system is to include pressure measuring capabilities. A pressure interface manufactured by TSI Inc. has been received. It will be used to measure pressure versus crank angle along with the velocity measurements. A pressure transducer by Validyne will be used in conjunction with the LDV interface to take the pressure measurements. The pressure measurements will be made for a shaft speed of 500 rpm for both supercharged and naturally aspirated configuations. Also of future interest is to determine how supercharging and other intake conditions affect the flowfield during compression. This will also serve as baseline for comparison with numerical simulations.

5.0 FRICTION STUDIES

Results in this section describe some of the important losses associated with the operation of internal combustion engines. Calculation of real engine efficiency must include items such as auxiliary components and frictional losses. The thermodynamic models currently available for the rotary combustion engine do not include these factors. Models must be formulated and converted to mathematical descriptions before they can be implemented in computer simulations. This section describes the work at the MSU Engine Research Laboratory whose objective was to develop a preliminary data base for friction and auxiliary component modeling. The efforts described in this section are primarily the result of short projects undertaken by undergraduate students at MSU in the spring term, 1989. Copies of these project reports can be found in Appendix C.

5.1 Numerical Simulation of a Thermodynamic Process

In 1987, Professor J. B. Heywood and his colleagues at the M.I.T. Sloan Automotive Laboratory completed the most extensive thermodynamic simulation of the operation of a rotary combustion engine to that date. As studies of bearing and seal friction require pressure loading data, this code was brought to operational status on the Sun 4/260 work station located at the MSU Engine Research Laboratory. Concurrently, Tom Bartrand of Svedrup Corporation has made extensive modifications of the code to improve its performance and stability.

Samples of tabulated input and output data used in the thermodynamic simulation can be found in Appendix C. There are several issues concerning the simulation that are worth noting. (1) For a number of conditions, errors prevented the computation of chamber pressures. Results of this work will be compared to the recent experience of Bartrand to deter-

mine the cause of the aborted calculations. (2) Seventeen simulations were conducted for a range of intake manifold pressures, speeds and equivalent ratios which were tolerated by the simulation. (3) It appears that for many conditions, proper pressure loading data will be available by using this simulation. (4) From experience, it is also clear that the use of this simulation is not a "turn key" operation. To obtain useful results, an experienced user knowledgeable in the codes, construction and operation must review predicted results.

5.2 Analysis of Bearing Friction

Bearing loading in an engine results from forces exerted on the rotor by compression and expansion of gases and by inertia forces. For this study, an analysis relevant to the rotor and main bearings (plain bearings) which are hydrodynamically lubricated was conducted. Although bearing friction is not believed to be a major source of energy loss in a rotary engine, an understanding of bearing loading is especially important from the stand point of reliability and life. The detailed analysis for this work is described in Appendix C. This simulation was conducted for a rotary engine with one rotor and two main bearings. These techniques can easily be extended to engines with multiple rotors and main bearings. The design parameters considered in the analysis were bearing diameter, axial length, bearing clearance and oil viscosity.

The following conclusions were made from this study:

1. Bearing frictional losses are affected more by engine speed than by engine loading.
2. Frictional losses increase with speed and power output.
3. Friction increases as bearing size increases.
4. Friction increases with increasing viscosity.
5. Friction increases as radial clearance decreases.

5.3 Apex and Side Seal Frictional Losses

Before starting a discussion about the factors involved with sealing a RCE it is helpful to examine the standard network of seals used in the RCE. Referring to Figure 5-1 which was taken from Ansdale, one sees the long curved side seals which are in contact with the end covers of the cylinder and three apex seals which separate the three working cells of the engine. Examination of this sealing network gives an appreciation of the additional difficulty involved in sealing RCEs. The long length of the side seals and the irregular path traversed by the apex seals present problems different from those encountered in sealing reciprocating piston engines. Documentation of the forces acting on these seals has not appeared in the literature to any appreciable extent. Jones shows an approximate breakdown of friction losses at 6000 rpm in a Curtiss-Wright RC1-60 engine. Here seal friction losses are reported to be about 1 1/2 times the losses in the bearings and gears. Yamamoto shows gas sealing losses to be over 50 percent of the total normalized frictional losses in an unspecified rotary engine.

Knoll et al. developed a theoretical model of the forces acting on the apex and side rotary engine seals. This model was combined with experimentally obtained cell pressures to

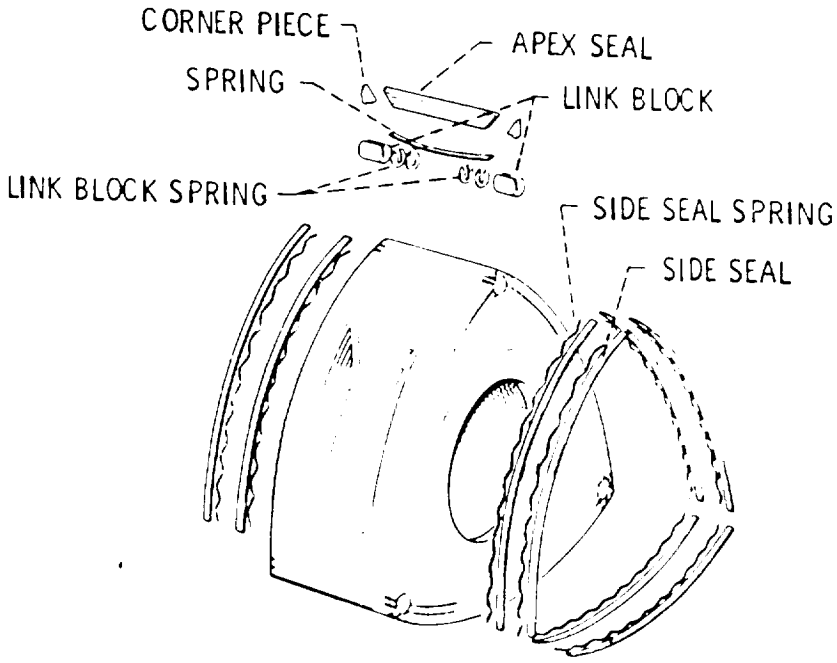

Figure 5-1 Typical sealing grid for a rotary combustion engine

obtain a friction model of a gas sealing system. In 1984 when this work was completed, a realistic thermodynamic model of the RCE such as the one described in Section 5.2 did not exist. The thermodynamics simulation now available can be combined with the apex and side seal friction models to obtain realistic evaluations of friction in gas sealing systems over a wide range of speeds and loads.

Knoll's theoretical model is a Fortran program which uses engine rpm and cell pressure of a typical rotary engine to calculate the work done by an apex seal during one cycle of the rotor. The program consists of four parts: the main program and subroutines "ONE," "VIB," and "SUBACC." The main program initially uses pressure points from a small file to create 2048 data points of cell pressure versus crank angle. This consistent input method facilitates program testing.

The backbone of the program is the set of equations describing the RCE's trochoidal bore. The shape of the trochoidal bore is described by geometric equations with the only variable being the crank angle. By differentiating the position equations, we obtain the velocity and acceleration of the apex seal. The velocity and acceleration components are then projected to a reference frame along the seal, giving the actual components of the apex seal.

The forces on the seal are from its loading and trailing cell pressures, apex spring, bore force and the acceleration. In calculating the moment about the center of gravity of the seal we can determine if the seal has pivoted to the leading or trailing side of the seal groove. The seal/bore contact force can be found by creating equations from a free body diagram, (FBD) of the apex seal. As long as the contact force (FC) of the bore on the seal is positive, the program's path stays in the main program. The work is calculated by multiplying the frictional force of the seal on the bore multiplied by the distance moved. Using Simpson's Rule, the work integral can be evaluated for an entire rotary cycle (2048 points).

If the apex seal loses contact with the bore (FC is less than or equal to 0) the subroutine "ONE" is called. "ONE" calculates the relative acceleration and position of the seal by calling subroutine "SUBACC" to find the true acceleration of the seal. This acceleration is calculated when the seal is not in contact with the bore. "ONE" will loop and increment data points until the seal returns to the bore.

Physical experiments show that when the seal returns to the bore, it bounces off the bore several times creating a vibrational effect. Due to this fact, after returning from "ONE", the subroutine "VIB" is called to loop until the seal stops vibrating. "VIB" also uses subroutine "SUBACC" to find the seal's position and acceleration.

The initial apex seal model is functional due to small changes in format and variable placing. The program produces an output declaring that the work of one apex seal during one cycle at 7000 rpm and 100% throttle is approximately 1600 in-lbs.

In reviewing the equations used in the initial program, errors have been found. Several components describing the trochoidal bore are missing. Sign errors were found in the differentiation of the x and y equations to achieve velocity and acceleration of the apex seal.

The program also has the ability to get caught in an infinite loop due to incorrect force and pivot equations. Furthermore, in calculating the work of the apex seal, the force on the apex seal from the bore was undefined at the points where the seal is no longer in contact with the bore.

The above changes have been made to the original program. The modified program is not operational due to faulty acceleration equations of the seal when it is not in contact with the bore. The incorrectly calculated acceleration never allows the seal to return to the bore. This problem is only temporary and the modified program will soon be operational.

5.4 Auxiliary Components

Modelers typically calculate indicated quantities when performing a numerical simulation of an engine cycle. The main reason for this is that information on friction and other loads, such as the alternator output, is generally not known. Frictional aspects were discussed in previous section. This section briefly summerizes the work described in Appendix C titled "Auxillary Components of an Aircraft Rotary Engine". The components considered in this preliminary design study include:

1. Electrical system (starter and alternator)
2. Cooling system (radiator and water pump)
3. Pumping sytems (oil pump and fuel pump)

Results of this design study are summerized as follows:

1. An optimized system design will yield significant battery weight savings in difficult-to-start engine application.
2. Significant starting-energy economics can be realized with an optimized system, allowing additional benefits to engine ignition operation and to component life of the battery, starter, contact points (if applicable), and engine.
3. It was found from the study that the pumping efficiency may be improved for a given flow rate if the rotor width is increased while the rotor radius and the rotation speed are reduced
4. The effect of the rotor diameter on the pumping efficiency is great, which is indicated by the relationship of r^5 for the fluid friction loss, and r^3 for the thrust friction loss.
5. The effect of the pump rotation speed (engine speed) is $n^{2.5}$ for the fluid friction loss, $n^{1.86}$ for the thrust friction loss, and nearly linear with speed for the other variables.
6. The liquid cooling offers definite advantages over air cooling in the areas of durability and performance. Other advantages such as lower operating costs and operational improvements are more subjective and can only be substantiated with service experience.
7. Some of the other benefits include: Absence of cooling airflow anomalies, better cylinder wear characteristics, increased power output, significant reduction in cooling drag, and greater tolerance to operational abuse.

6.0 COMPUTER CONTROLLED MAPPING

Numerical methods which have been used during the past year have pointed to control of the rotor pocket geometry as the most logical method of controlling turbulence and fuel air mixing n a rotary combustion engine. Quantifying this geometrically complicated configuration can be achieved with a device that uses laser triangulation for non-contact sensing. The "Z" axis sensing, together with the X and Y position of the translation stages, can be used to produce a three dimensional map of the rotor flank, including the rotor pocket. This device can be used to produce a tape for machining a particular surface which has been found to produce desired flow effects, such as with a wood model. It can be used to provide input to a numerical simulation for modeling purposes. The resolution of the point range sensor chosen for this work is twenty microns.

6.1 Description of Mapping System

The computer controlled mapping system is briefly described in this section., A complete description of the system can be found in Appendix C.

The system to perform this mapping consists of the following elements:

1) A point range sensor manufactured by Cyber Optics Corporation
2) A three dimensional traverse table with :
   - x - translation 960mm
   - y - translation 480mm
   - z - translation 480mm

   Other table characteristics can be found in Appendix C, Figure 5.

3) A Sony linear position encoder
4) A Zenith portable computer for system control

The position of the table is measured by the Sony linear position encoder which measures the position of the table relative to its absolute home and transmits this position to the Zenith computer. The point range sensor is conducted to the computer through a parallel interface card installed in the communication bus of the computer. The Sony encoder and the traverse table control are connected through RS-232-L port conversions. The Zenith computer reads the position of the table and the measurement from the point range sensor. It examines the data and determines the absolute position of the surface being measured. The computer moves the system over a predefined area to determine the absolute coordinate of this area. The result is a three-dimensional mathematical description of the object of interest.

6.2 Status of Computer Controlled Mapping System

The traverse table and its control computer are already in the MSU Engine Lab. The

point range sensor system has been purchased and received. The Zenith "Turbo Sport 386" has also been purchased and received. The necessary software components have all been purchased or written .

There are two remaining steps in the implementation of this system. The first involves debugging and rewriting parts of the control software. As is noted in Appendix C, the software packages were written in three different languages and must be combined to make the system operational. The second step is to accomplish the interface between the Zenith computer and the other three components of the system (PRS, Sony, Traverse Table). This will require the purchase of cables and serial interface cards that have not yet been obtained.

All the components are expected to be assembled with initial testing done by August 7, 1989. At that time, more precise testing will be done to enable the system to perform at its peak accuracy and maximum repeatability.

REFERENCES

Ansdale, R.F., "The Wankel RC Engine," South Brunswick, N.J. A.S. Barnes, 1969

Jones, C., "The Curtiss-Wright Rotating Combustion Engines Today," SAE Transactions, Vol. 73, 1965, pp. 127-147

Knoll, J., Vilmann, C.R., Schock, H.J., and Stumpf, R.P., "A Dynamic Analysis of Rotary Combustion Engine Seals," SAE Paper #840035 2/84

Yamamoto, K., "Rotary Engine," Hiroshima, Japan, Toyo Kogo, 1981

Appendix A

PRELIMINARY DRAFT

OPERATION OF THE BKM FUEL INJECTION SYSTEM FOR THE NASA ROTARY ENGINE

BY

JUDAH KOSTERMAN
UNDERGRADUATE RESEARCH ASSISTANT
ENGINES RESEARCH LABORATORY
DEPARTMENT OF MECHANICAL ENGINEERING
MICHIGAN STATE UNIVERSITY
EAST LANSING, MI 48824

For IC engines of any design, fuel injectors have several advantages over carburetors.[1] In terms of engine performance, use of a fuel injector combines the elimination of pressure losses and condensation at the throttle with an increase in cross-sectional area of the intake manifold (no narrowing at the venturri) to produce increased volumetric efficiency. This in turn produces increased power and torque. Since the fuel need not flow through a manifold, the injection can take place near or at the combustion chamber, allowing for faster acceleration and eliminating after-run from "stored" air/fuel mixture in a carburetor. Engine starts are quicker and the possibility of flooding reduced since fuel atomization with an injector is independent of crank speed. Some operational problems associated with IC engines involving carburetors can be reduced by use of fuel injection, namely throttle-plate icing, engine knock, backfires, and hydrocarbon emissions. The use of fuel injection also allows for some important design options. Since the distribution of the fuel is independent of vaporization and does not require the addition of heat, the range of usable fuels expands to include those less volatile and of a lower octane content than fuels usually used with carburetion. In addition, since the air/fuel mix ratio with a fuel injector is basically independent of injector position, engine motion, or operating temperature, the location of the injector is essentially unrestricted.

For the NASA rotary engine design, the injection will be directly into the combustion chamber. Two additional advantages of the injector bear mentioning in this application: the fuel spray will have a velocity field, allowing it to be directed towards a specific region of the combustion chamber, and the fuel spray will be concentrated in that region, which will prove beneficial for producing a more complete combustion in an asymmetric chamber.

Injecting the fuel directly into the combustion chamber is a significant design alteration from conventional IC engines where the fuel is injected into an intake manifold. Thus conventionally some air/fuel mixing occurs outside the combustion chamber and the fuel jet has the distance of the intake manifold in which to atomize. Although the lack of a homogeneous air/fuel mixture in the NASA rotary engine can in fact be beneficial, the restricted distance the fuel jet travels (less than 10 cm) requires very rapid atomization. Atomization is achieved through the decay of a high-velocity jet, which is produced in the fuel injector by obtaining a very high injection pressure. Due to the required pressure, an accumulator-type injector which pressurizes the fuel before injection was chosen over a conventional fuel injector which pressurizes the fuel as it is being injected.[2]

The electronically-controlled BKM Servojet fuel injector and supply system currently being tested is designed per NASA Contract No. NAS3-25166.[3] As it has been set up, the injector is connected to a closed-loop constant-pressure (rail-pressure) fuel supply system. The injector itself is composed of a supply port at the rail pressure, a solenoid-controlled 3-way ball-poppet valve[4], a hydraulic "slave" valve of the same 3-way ball-poppet design, spring-aided hydraulic intensifying pistons of area ratio 15:1[5], a vent port for the piston chamber, a spring-aided ball-closure valve to supply the intensifier chamber, a spring-aided check valve separating the intensifier and accumulator chambers, and a needle valve to control the flow of fuel through the apertures in the nozzle tip.

A simplified schematic diagram of the injector is shown on the next page. An injection event

proceeds as follows. Power to the solenoid is turned on, "attracting" the base of the solenoid-controlled valve and causing the ball at end H to move firmly against its bushing. This creates an open passage such that some fuel flowing in from the supply port A is diverted along branch C, past the solenoid-valve ball at end C, and - unable to flow past the ball at end H - along branch D. This fuel flow applies a pressure to the hydraulic slave valve, causing the ball at end D to move firmly against its bushing. With the hydraulic valve in this position, fuel flowing from A into branch B can now flow around the slave-valve ball at end B and - unable to flow past the ball at end D - into chamber E.

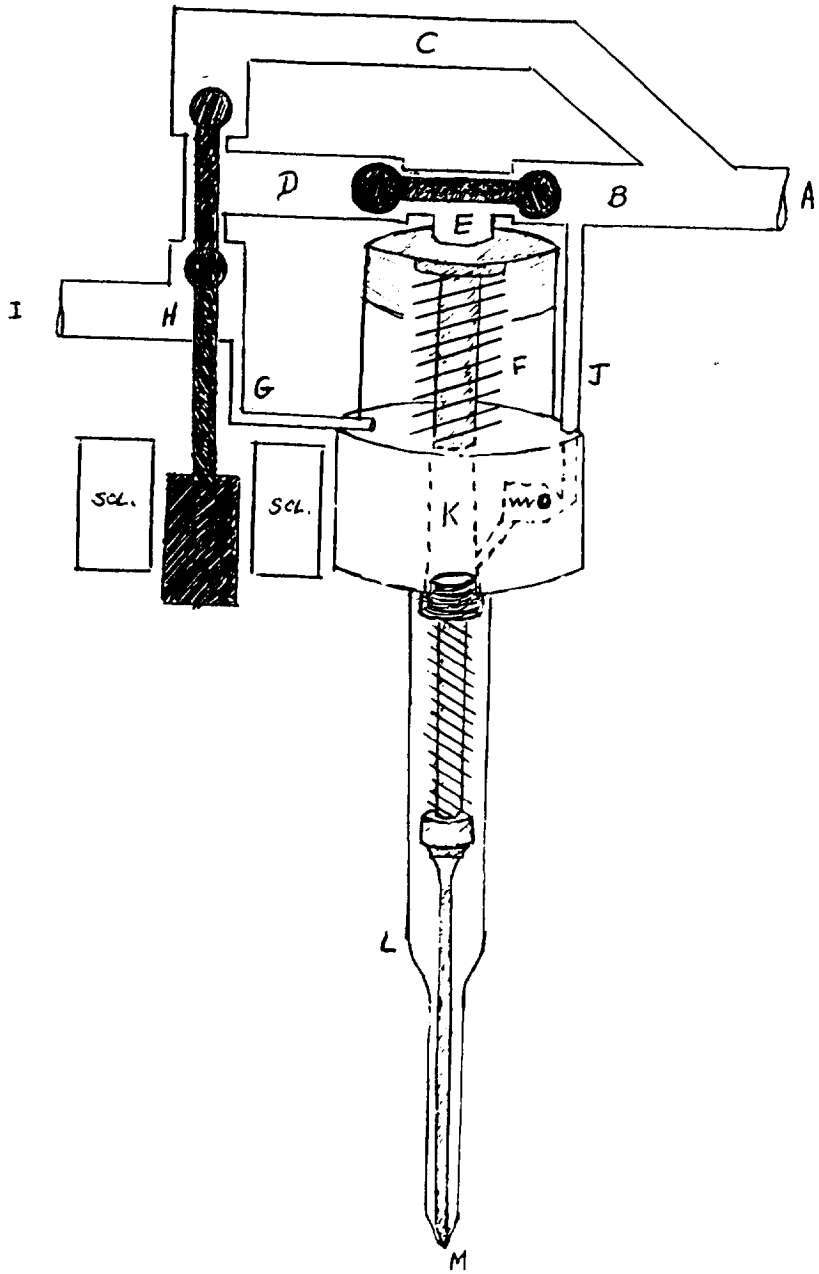

Chamber E is of variable volume and consists of a short passage from the slave valve to the chamber containing the intensifying pistons. And any "space" created above the low-pressure (large) piston by movement of the intensifying pistons away from their seating against passage E. As the pressure in chamber E builds, it begins to force the intensifying pistons away from their seat, which in turn compresses the spring in chamber F. Chamber F is also of variable volume and is composed of the "space" below the low-pressure (large) piston, bounded at the bottom by the body of the intensifier, K. The fuel in chamber F is compressed as the low-pressure piston moves towards the intensifier, creating a flow through branch G.

The fuel from chamber F flows into branch H and, all other pathways being blocked by the solenoid valve, out of the vent port I. Simultaneously, the fuel in the intensifier chamber, K, is also being compressed, creating a flow into branch J which keeps the ball-closure valve along this branch closed, thus cutting off the intensifier from the fuel supply. As the intensifying pistons continue the compressive stroke, there is an increasing pressure applied to side K of the check valve which is held against its bushing by a pre-load of the spring in chamber L. Once the pressure in the intensifier chamber, K, exceeds this spring force, the check valve (a stepped collar free to slide along the pintle base) is forced open and fuel from the intensifier, K, can flow into the accumulator, L. The compressive stroke will continue until the low pressure piston has displaced the desired volume of fuel to be injected, assuming a 75-80% volumetric efficiency. At this point, the springs in chambers F and L are at maximum compression and the pressure in the intensifier/accumulator chamber is at its maximum.

When power to the solenoid is turned off, the base of the solenoid control valve is "released" and the head-on stream pressure on the ball at end C forces this ball firmly against its bushing. With the flow through branch C cut off, all flow from the supply A is directed into branches B and J. The head-on stream pressure on end B of the slave valve forces the ball at the B firmly against its bushing. An open passage is thus created such that fuel in chamber E can flow past the slave-valve ball at end D, past the solenoid valve ball at end H and out through the vent port I. When this fuel from chamber E enters branch H, some of it will flow through branch G and into chamber F. Simultaneously the flow from the supply A will be directed entirely through branch J, forcing the ball-closure valve along this branch open and creating a passage for fuel to flow into the intensifier, K. The combined effects of the spring force in chamber F, a loss of pressure in chamber E, and increases in pressure in chambers F and K produce a very rapid movement of the intensifying pistons back to their seat. This rapid rise creates a pressure drop in chamber K. The combined effects of a loss of pressure on side K of the check valve and the spring force on side L of the check valve force this valve closed, thus separating the intensifier, K, and accumulator, L. Once the check valve is re-seated the spring in chamber L (the needle valve spring) is back to its original compression. There is, however, a "reaction force" that occurs such that the needle valve tip, having been increasingly forced against its seat at M, rebounds from the sudden loss of compression, causing the tip to lift from its seat M. This creates a passage for the high-pressure fuel in the accumulator, L, to flow past the needle tip and out the apertures of the nozzle at M. The fuel will continue to flow out until the pressure in chamber L drops below the pre-load in the needle valve spring, at which point the needle valve closes, ending the injection event. When the pressure in chamber K is equal to the pressure in branch J the ball-closure valve in branch J shuts and the injector has completed a firing cycle.

The following diagrams show a schematic progression of an injection event. Note that neither these diagrams nor that on the previous page are schematically exact - they are, however, functionally correct and should be used only to aid in understanding "How the thing works."

It should be noted that the physical set-up of the injector itself influences injector performance. Both the spring in the piston chamber, F, and the spring in the accumulator, L, are pre-loaded in compression.[6] The static deflection, X_O, of the spring in the piston chamber

with spring constant k_1 limits the net distance the pistons will travel, x. For a given rail pressure, RP, the low pressure piston will travel at most a distance x such that $k_1 (X_o + X) = RP$. The static deflection of the spring in the accumulator, d, is approximately 10x the needle lift during injection.[7] It is this deflection in combination with the spring constant, k_2, which determines the residual pressure, P_R, at which the needle valve will close; specifically, $P_R = k_2 d$.[8] (For our current set-up 3000 psi $\leq P_R \leq$ 4000 psi).[9] A given physical set-up also fixes the cross-sectional area of the supply and vent ports and the area and configuration of the apertures for injection. The discharge area has an effect on the rate of injection, namely that as the area increases, injection duration decreases and vice versa.[10] In our set-up a "Greerolator" (a bladder in a metal bottle) has been added to the supply line to dampen any fuel surges. It has been found, however, that this addition can lead to timing instabilities.[11] Finally, the choice of fuel sets the density and viscosity at varying temperature and pressure conditions.

The two major parameters affecting injector performance are rail pressure and energize time. The rail pressure is specifically responsible for the functioning of the ball-closure valve at J and limiting the maximum attainable pressure within the injector. The energize time controls timing stability and can limit the compression stroke and injection duration. The pressure attained within the accumulator, injection rate, mass of fuel delivered, and engine emissions are influenced by a combination of energize time and rail pressure.

The rail pressure by itself acts as a limiting factor. The ball-closure valve at J opens only when the pressure in branch J (the rail pressure modified by an area ratio) exceeds the pressure in the intensifier, K. The maximum attainable pressure within the injector is determined by the rail pressure since the ratio of the areas of the intensifying pistons, ϕ, is fixed and $P_{MAX} = \phi (RP)$.

The energize time by itself has effects which should be taken into account when adjusting the functioning of the injector. Cycle to cycle timing stability is maximized by "fine tuning" the energize time in calibration.[12] Since compression occurs only when the solenoid valve is energized, the injector's compression stroke can be shortened by reducing the energize time[13] such that the low pressure piston doesn't travel its full distance ($k(x + x_o) \neq RP$). Likewise, at a given frequency the duration of injection can be reduced by increasing the energize time since injection occurs only when the solenoid is de-energized.

The pressure attained within the accumulator, P_A, is a function of both rail pressure which is the starting pressure for compression and energize time which determines the length of the compression stroke. The rate of injection is a function of P_A coupled with the physical factors of needle valve lift and discharge area.[14] To deliver a set amount of fuel, an increase in P_A decreases injection duration and vice versa.[15] The quantity of fuel injected is controlled by P_A, specifically, as P_A increases the amount of fuel injected per unit of time in-

creases, and vice versa.[16] An increase in P_A was also found to decrease emission of smoke, hydrocarbons, and NO_X from a diesel engine.[17]

The actual P_A attained in the injector will reach 80-95% of its theoretical maximum ($0.80\phi(RP) \leq P_A \leq 0.95\phi(RP)$) if the ratio of the accumulation time to the injection time is much greater than one.[18] The details of injection termination are determined by the needle seating velocity which is in turn dependent upon the decay of P_A during the injection event.[19]

The overall performance of the BKM injector far exceeds that of conventional fuel injectors. A case in point is a trial run by BKM at 250rpm in which the average jet velocity was 10x that of a conventional fuel injector, producing a spray with much higher energy than could normally be attained.[20] The performance of this injector is, however, complicated by the interdependence of many factors, those which can be adjusted for our purposes (rail pressure and energize time) and those physical constraints of the system set-up which must simply be worked around.

One of the more troublesome physical constraints at present is the fit experienced between the needle valve and the nozzle tip. Appendix A details an analysis made of this fit from prints provided by BKM. It was noted that the purchase date of our BKM injection system preceded the release dates of the prints, necessitating some educated guessing.

The needle valve print (PN 606169) contained two sets of dimensions, a "-1" and a "-2" version. From the release dates of the annotated prints, it is assumed that we have a "-2" version. The critical dimensions are listed in Appendix A. From these dimensions we see that the "-2" is longer than the "-1" and has a much blunter tip. Assuming that the same nozzle tip was used with both valves, it was observed that the "-2" version mates very poorly with the nozzle tip, fully "sealing" only the extreme end of the nozzle tip between injections. From the machining instructions for the nozzle tip contained in PN 606451, it was assumed that the positions of apertures in multiple-hole tips were drilled with respect to a scribe mark on the nozzle tip. The location of this scribe mark is shown in Appendix A. This would place some of the apertures in a region of the nozzle tip which is not sealed between injections.

Evaluating the performance of the "-2" valve some problems come to light. The added length over the "-1" version coupled with an absence of "guides" within the accumulator cavity[21] leads to a non-uniaxial retraction of the needle valve, allowing for some apertures to "open" before others (non-simultaneous firings). The (assumed) failure of a full seal between injections could contribute to the phenomenon of trailing droplets. It is also possible that the "-2" valve itself is compressed by the high-pressure fuel in the accumulator, contributing to poor fit and droplet formation[22], although this has not been substantiated. In conclusion, the needle valve itself is probably the largest contributor to the non-uniformity of injection which we have observed.

FOOTNOTES

[1]Edward F. Obert, Internal Combustion Engines and Air Pollution (Harper & Row. Publishers, New York), p. 402.

[2]p.2, SAE paper # 840273

[3]p. 1, Calibration test report by BKM Inc.

[4]p.3, SAE paper # 840273

[5]p.3, SAE paper # 840273

[6]per Bill Johnson of BKM

[7]per Bill Johnson of BKM

[8]p. 5, SAE paper # 840273

[9]per Bill Johnson of BKM

[10]p. 5, SAE paper # 840273

[11]per Bill Johnson of BKM

[12]p. 9, SAE paper # 840273

[13]p. 4, SAE paper # 840273

[14]p. 4, SAE paper # 840273

[15]p. 5, SAE paper # 840273

[16]p. 6, SAE paper # 861098

[17]p. 7, SAE paper # 840273

[18]p. 7, SAE paper # 840273

[19]p. 4, SAE paper # 840273

[20]p. 8, SAE paper # 840273

[21]per Bill Johnson of BKM

[22]per Bill Johnson of BKM

1) Solenoid valve opens
Start to apply rail pressure to intensifying pistons
Fuel in piston chamber to vent
Check valve still closed

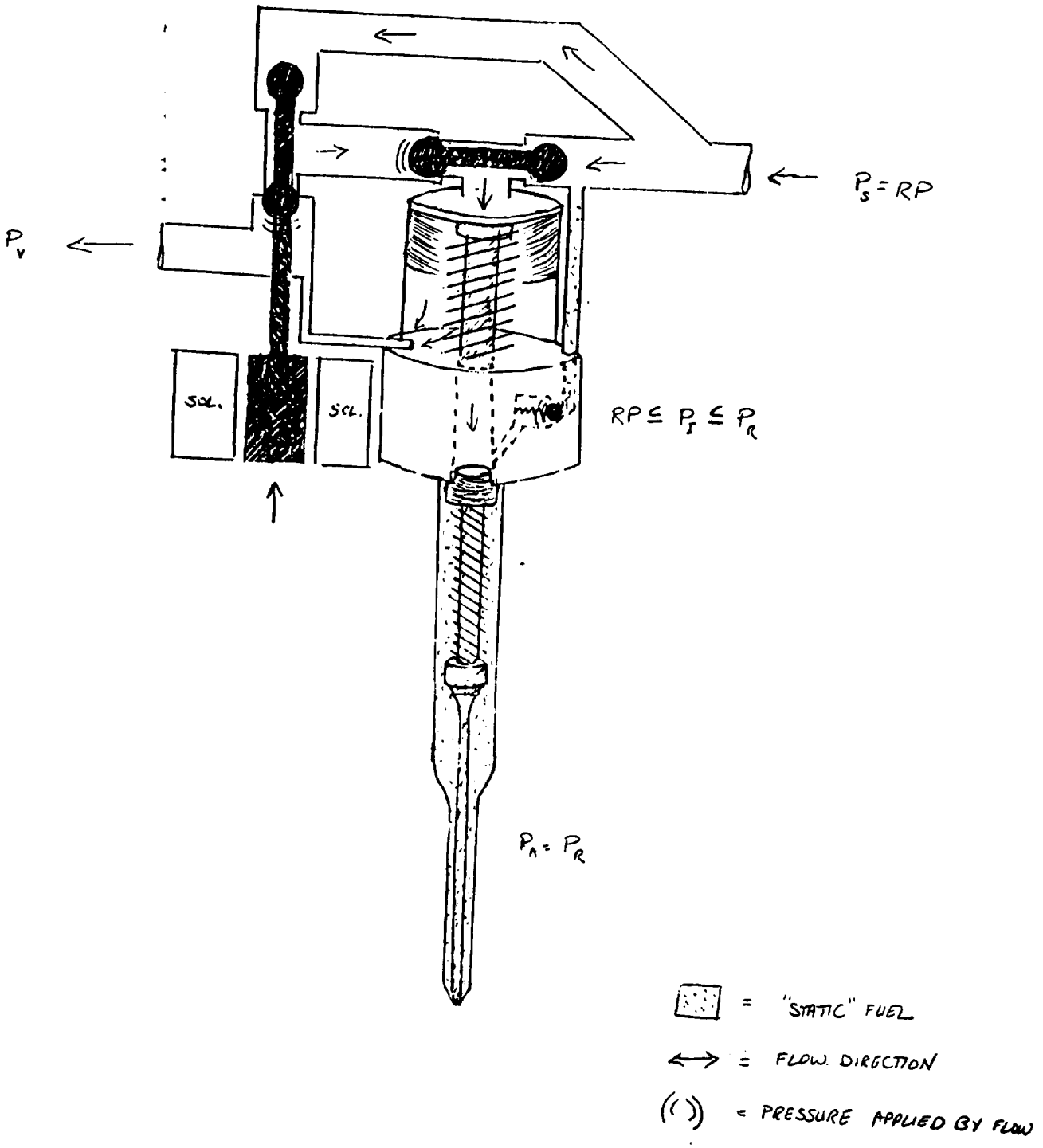

2) Solenoid still on
Compressive stroke in progress
Check valve opens

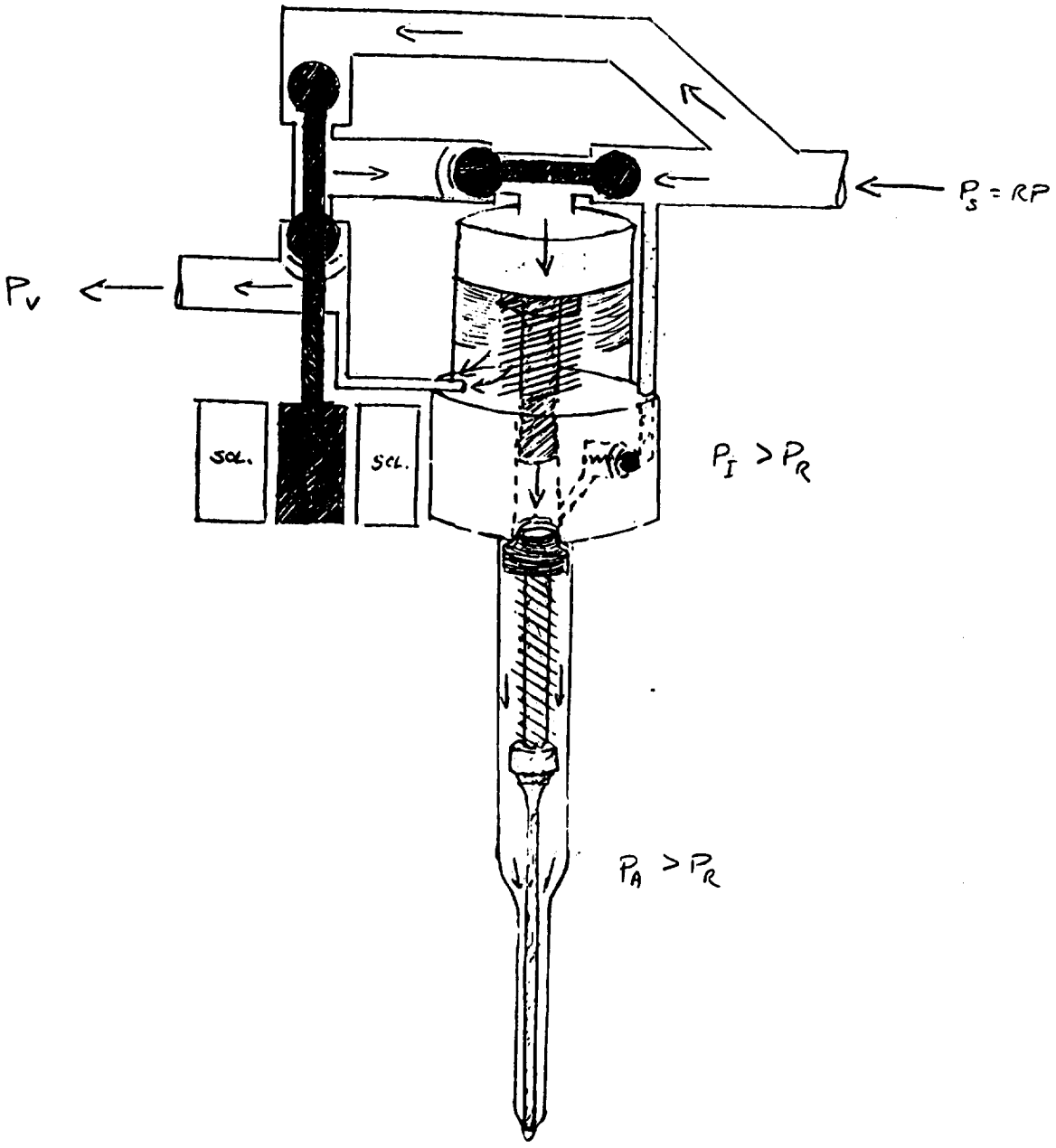

= "STATIC" FUEL

= FLOW DIRECTION

= PRESSURE APPLIED BY FLOW

3) Maximum compression of piston spring
Check valve fully open, maximum compression of valve spring
NOTE: The maximum compressive stroke of the pistons does not "bottom out" at the intensifier body

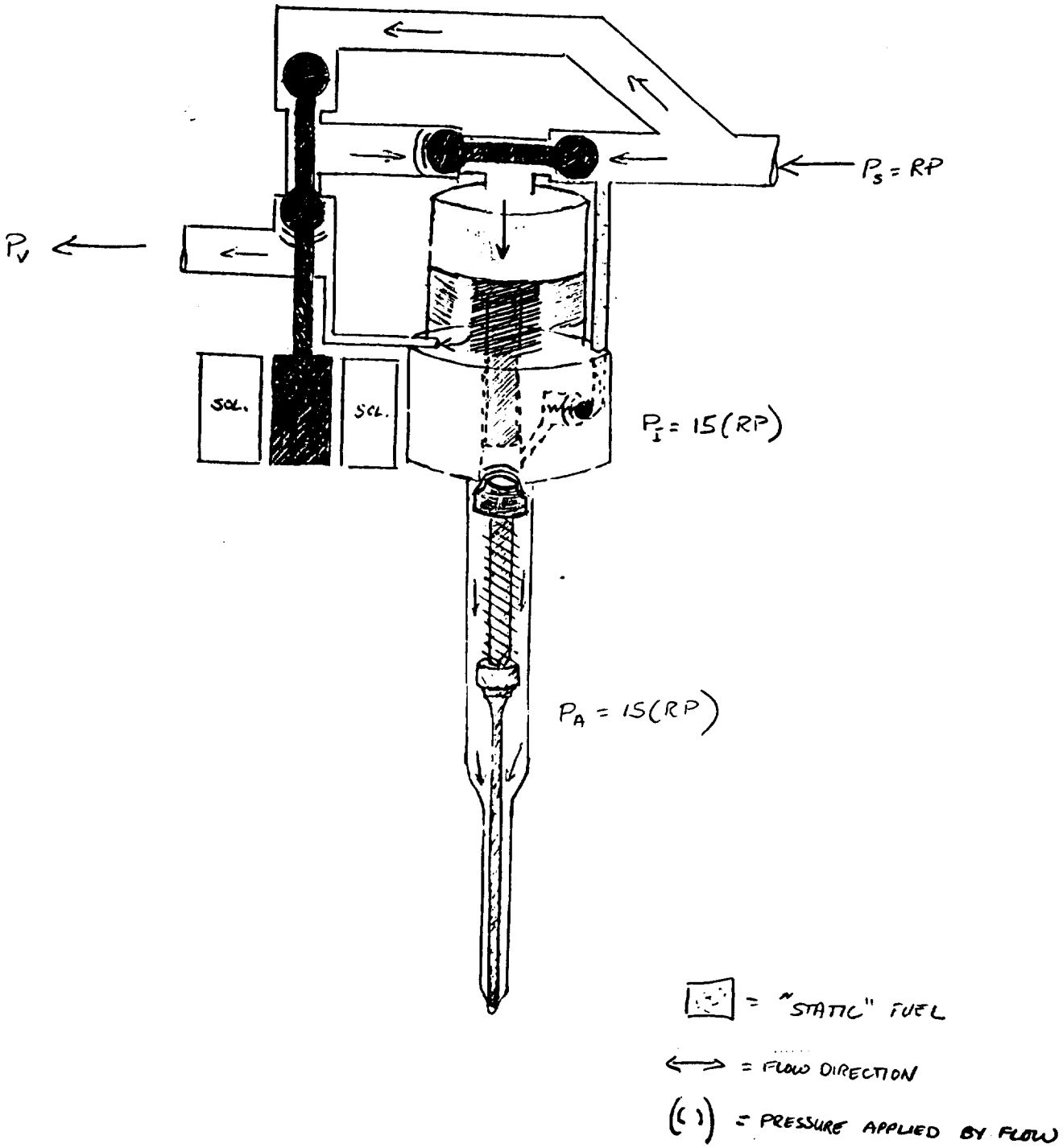

lve closes
t fuel compressing pistons
: closes
'e lifts due to reaction force, injection event
: valve forced open, fuel flows into intensifier for next injection (also raise pistons)
to vent diverted to piston chamber to help raise the low pressure piston

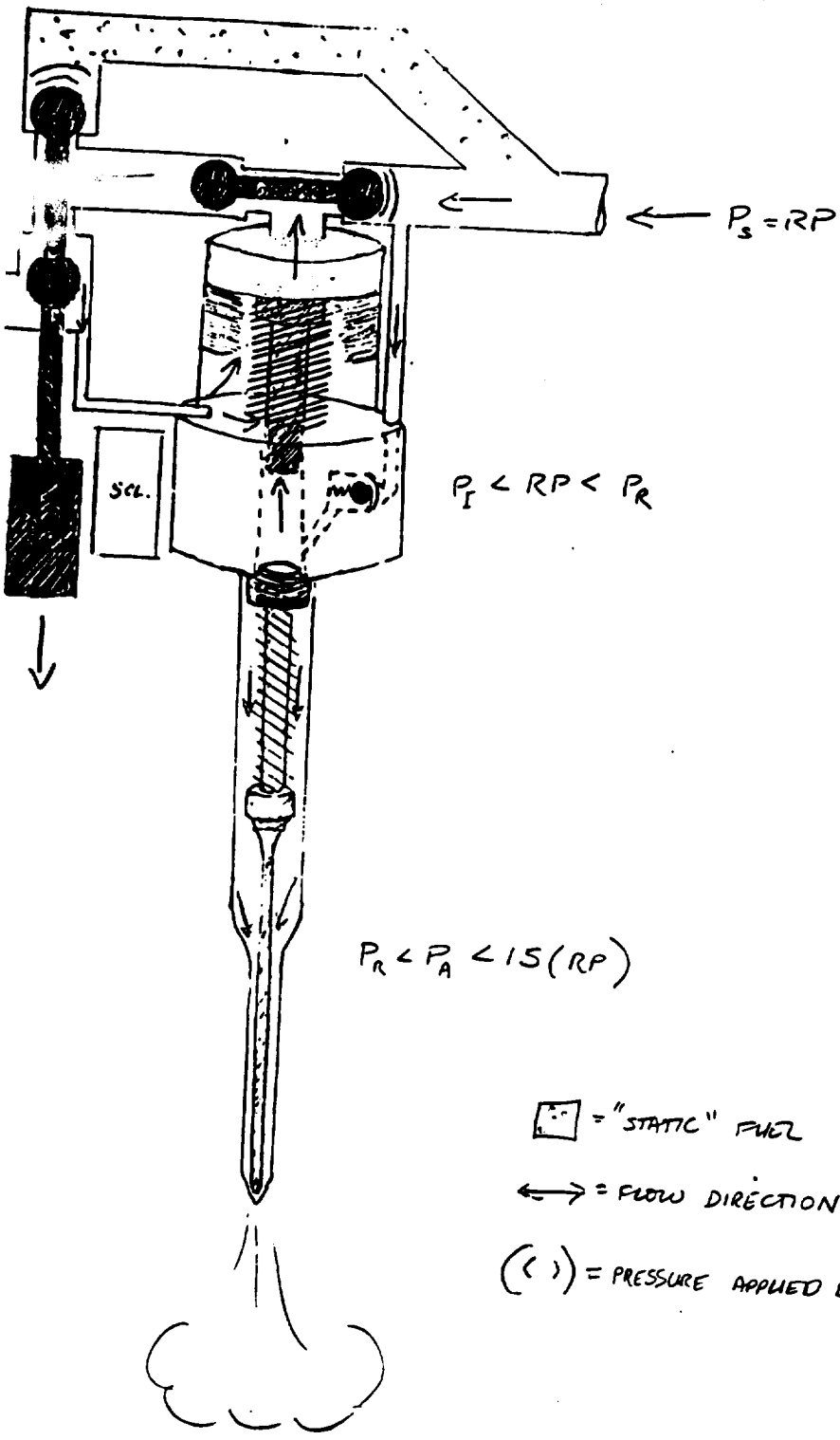

ORIGINAL PAGE IS
OF POOR QUALITY

5) "Static equilibrium position"
Needle valve closes
Intensifying pistons returned to original compression
Ball-closure valve closes

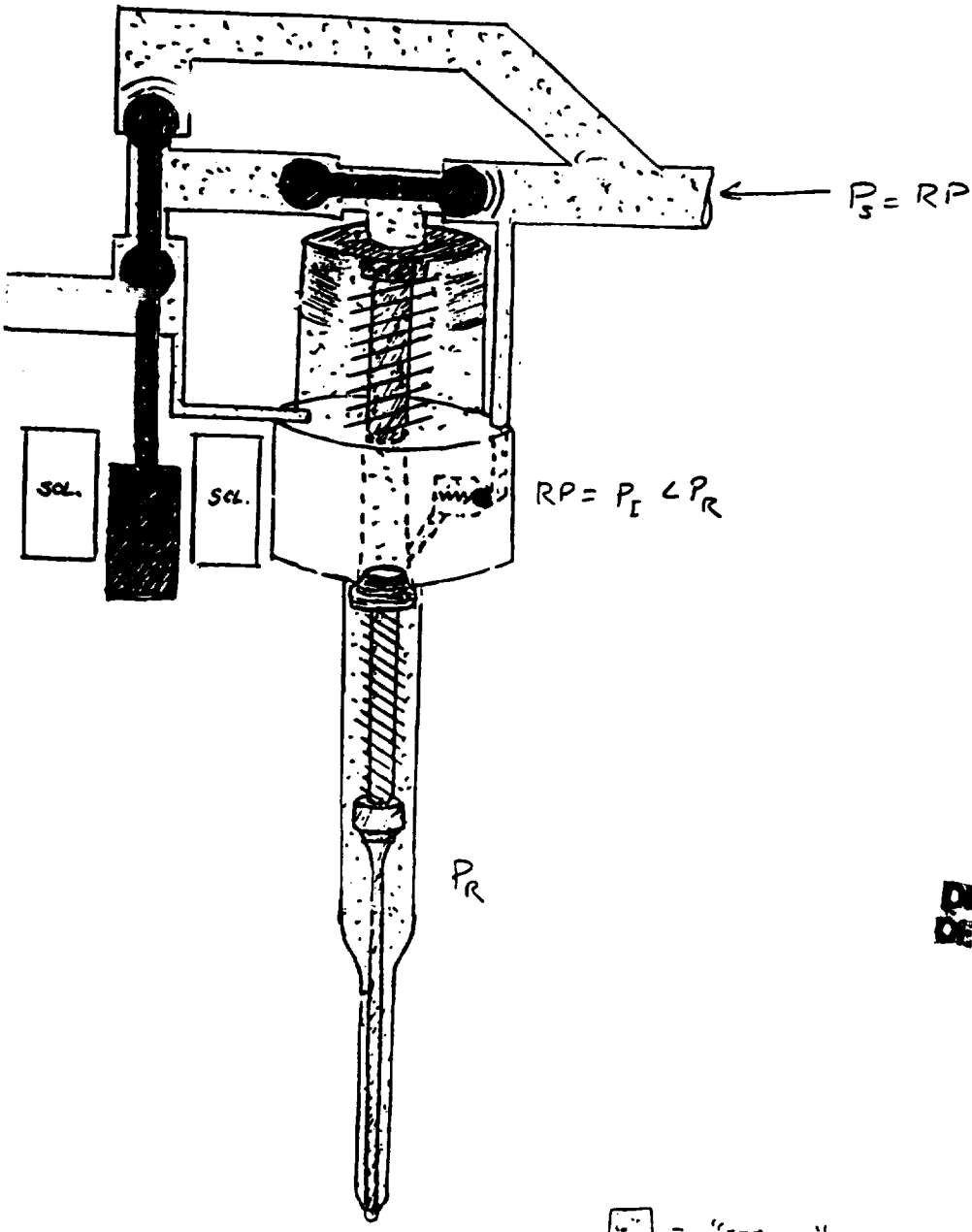

ORIGINAL PAGE IS
OF POOR QUALITY

= "STATIC" FUEL

⟷ = FLOW DIRECTION

(( )) = PRESSURE APPLIED BY FLOW

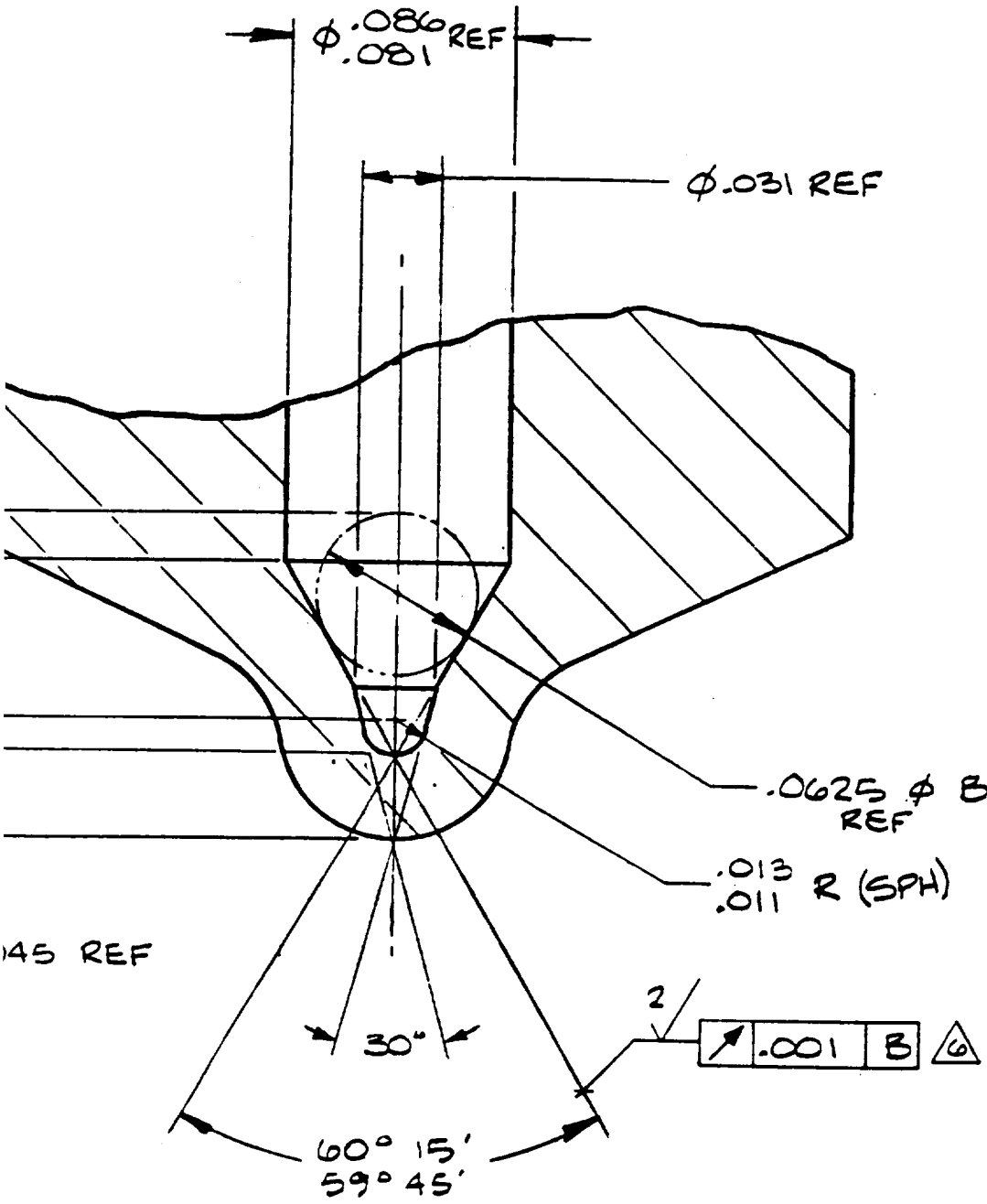

ORIGINAL PAGE IS
OF POOR QUALITY

Appendix A

Dimensional Analysis of Mating Parts in Injector Nozzle

PN 606169, Needle Valve

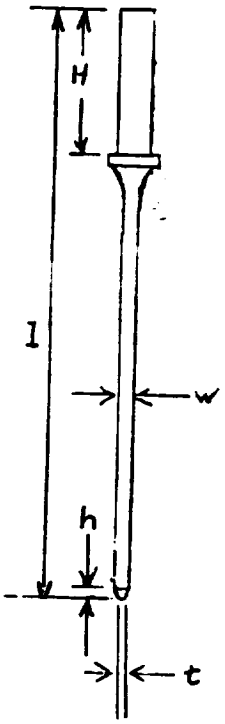

CRITICAL DIMENSIONS

DIMENSION	"-1" Model	
	Nominal (in.)	Tolerance (in.)
l	2.825	±0.010
h	0.041	±0.011
t	0.010	±0.001
w	0.059	[illegible]
H	0.890	±0.005

DIMENSION	"-2" Model	
	Nominal (in.)	Tolerance (in.)
l	3.307	±0.010
h	0.041	±0.011
t	0.0225	±0.0025
w	0.059	±0.001
H	0.910	±0.005

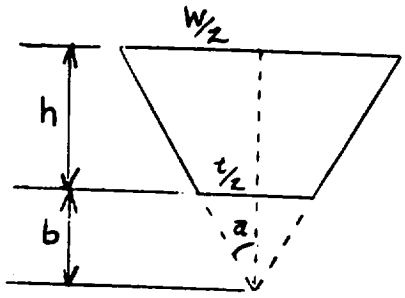

$$\frac{w/2}{t/2} = \frac{h + b}{b}$$

$$w/t = \frac{h + b}{b}$$

$$wb = ht + bt$$

$$b(w-t) = ht$$

$$b = ht/(w-t)$$

$$a = \arctan\left(w/2 \div (h + b)\right)$$

Results:

"-1" Model
b = 0.008 in.
a = 31.9°

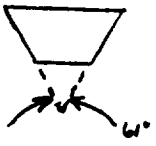

"-2" Model
b = 0.025 in.
a = 24.1°

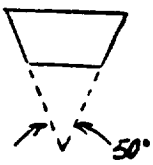

52, Nozzle Tip

alysis: 60° Internal Mating Angle
See p. A-3 for details
The nozzle tip is assumed the same for both mating cases

sults:

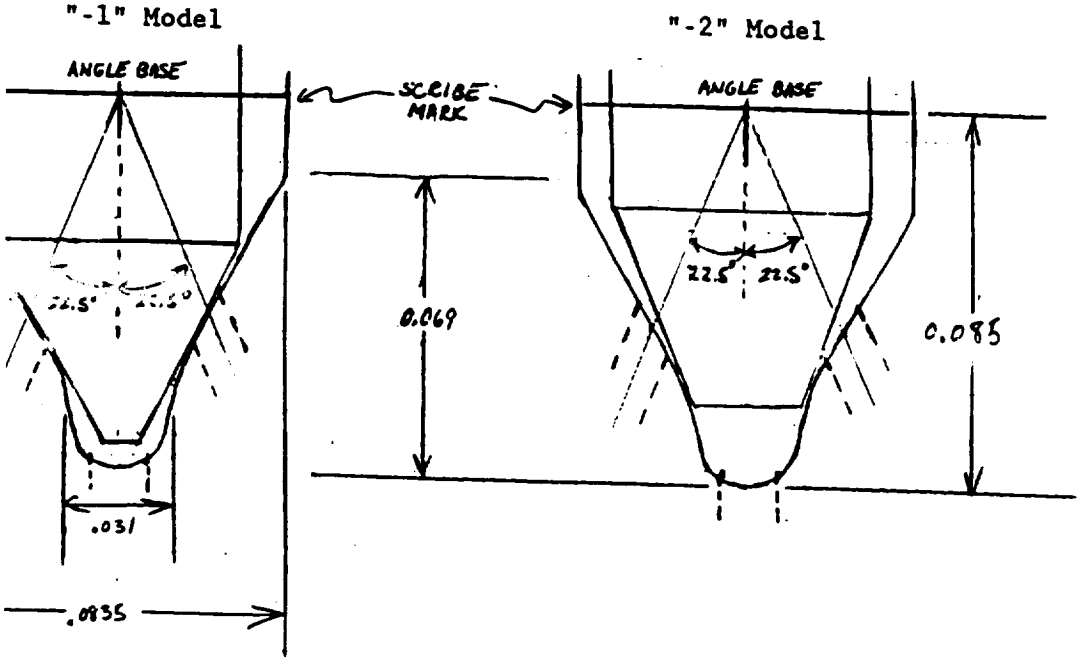

itions of 3 x 0.396mm holes shown for reference
dimensions in inches unless otherwise noted

ORIGINAL PAGE IS
OF POOR QUALITY

Appendix B

The Engineering Society
For Advancing Mobility
Land Sea Air and Space®
400 COMMONWEALTH DRIVE, WARRENDALE, PA 15096-0001 U.S.A.

SAE Technical Paper Series

890331

Stratified Charge Rotary Engine Internal Flow Studies at the MSU Engine Research Laboratory

F. Hamady, J. Kosterman, E. Chouinard, C. Somerton and H. Schock

Michigan State University

East Lansing, MI

K. Chun and Y. Hicks

NASA Lewis Research Center

Cleveland, OH

International Congress and Exposition
Detroit, Michigan
February 27 — March 3, 1989

890331

Stratified Charge Rotary Engine Internal Flow Studies at the MSU Engine Research Laboratory

F. Hamady, J. Kosterman, E. Chouinard, C. Somerton and H. Schock

Michigan State University
East Lansing, MI

K. Chun and Y. Hicks
NASA Lewis Research Center
Cleveland, OH

ABSTRACT

This study involves the development of high speed flow visualization and laser doppler velocimetry (LDV) systems which are used to study the fuel spray-air mixing flow characteristics within the combustion chamber of a motored rotary engine. A 40-watt copper vapor laser is used as the light source. Its beam is focused down to a sheet approximately 1 mm thick. The light plane is passed through the combustion chamber, which allows complete optical access, and it illuminates smoke particles which were entrained in the intake air. The light scattered off the particles is recorded by a high speed rotating prism camera. Movies are made showing the air flow within the combustion chamber. The results of a movie showing the development of a high speed (100 Hz) high pressure (68.94 MPa, 10000 psi) fuel jet are also discussed. The visualization system is synchronized so that a pulse generated by the camera triggers the laser's thyratron. The camera is run at 5000 frames per second; the trigger drives one laser pulse per frame.

THE ATTRACTIVE FEATURES of the stratified charge rotary engine have been documented in previous reports and are briefly reviewed here [1,2]. First, in terms of fuel consumption and specific weight, the rotary combustion engine seems to fit between the small gas turbine and the reciprocating piston engine. The rotary engine's fuel economy is slightly higher than that of the piston engine; however, it is substantially better than that of the simple small gas turbine. In terms of power-to-weight ratio and volume, the rotary engine has a higher power density than that of the piston engine and a poorer power density than that of the turbine engine. The rotary engine has two other important advantages: un-

0148-7191/89/0227-0331$02.50
Copyright 1989 Society of Automotive Engineers, Inc.

tions discuss the progress to date in bringing to operational status the equipment necessary to develop this experimental base and preliminary results of the flow visualization, LDV, and fuel injection studies.

DESCRIPTION OF THE ROTARY ENGINE ASSEMBLY

The rotary engine is composed of a Mazda 12A central housing (generating radius R= 105 mm and eccentricity e= 15mm) motored by a 7.5 kW (10 hp) constant torque electric motor. The rotor configuration has a Leading Deep Recess (LDR), which provides a rotor recess that is deeper on the leading side of the homogeneously charged engine.

For the purpose of this work, the side housings are modified to support adjustable air-tight window frames on the upper and lower sides, where four sapphire windows are mounted. This provides optical access for the laser doppler velocimetry measurements and flow visualization as shown in Figure 1. The central housing has also been modified by making a window through the perimeter of the housing wall so that a laser sheet of light can pass through. A plexiglas window is now in use, and flow tests have been conducted at shaft speeds of 168 and 230 rpm. In order to apply the visual study and avoid deformation of the plexiglas window due to high temperatures associated with the high energy laser beam, discussions are underway which involve fabrication of a sapphire window for the central housing.

Finally, the rotor land of the rotor has been removed to prevent the rotor and the side housing from sticking together. The land is a projection provided on the side face of the rotor to define the position of contact between the rotor and the side housing. It is generally located on the inner side of the oil seal where sufficient lubricating oil can be supplied in a firing engine. The clearance between the rotor land and the side housing is generally set at 0.1 ~ 0.2 mm.

AIR FLOW VISUALIZATION IN THE MOTORED SCRE

FLOW VISUALIZATION SYSTEM - In a complementary approach to the laser doppler velocimetry (LDV), the flow fields within a rotary engine have been photographed to integrate the qualitative visual observations with the quantitative measurements of the velocity in the flow field. Unique visual techniques and experimental methods were devised to analyze the process and provide information on flow patterns during the intake and compression stroke within the rotary engine. These methods are analogous to work done for a piston cylinder assembly by Regan et al. [7].

The flow visualization system developed for this study consists of a 40-watt copper vapor laser, mirrors, cylindrical lenses, a high speed camera, a synchronization timing system and a particle generator. A photograph of the visualization system is displayed in Figure 2.

The copper vapor laser (CVL) is very adequate for high speed visual techniques. It is a gas discharge device of 40 watt average output power. It emits short pulses at repetition rates of 5000 pulses per second (pps) and a pulse energy of 8 mJ in the green and yellow regions of the visible spectrum, at wavelengths of 510 and 578 nm. The pulse rate can vary between 4000-6000 pps for efficient laser operation. The pulse width

is approximately 30 ns and pulse jitter is 3 ns. The model 451 copper laser main components are a plasma tube, high voltage DC power supply and pulsed discharge system (thyratron driver and thyratron). The thyratron driver is a high voltage, high repetition pulse generator which provides trigger pulses to the thyratron. The driver can be operated using the internal 5 kHz oscillator or by applying the external pulse to the trigger select.

The laser beam (5.08 cm in diameter and of Gaussian power) is directed toward the rotary engine by a set of three circular mirrors 10.16 cm in diameter. These mirrors together provide high-resolution angular control with coplanar-orthogonal adjustments. Two cylindrical lenses 10.16 cm square, 2.54 cm thick, made of BK-7 optical quartz are used to focus the beam into a light sheet approximately 1 mm thick. Their focal lengths are 332 cm and 80 cm respectively.

A Nac E-10/EE 16 mm high speed rotating prism camera which offers a super fast f 2.5 optical system is used to film flow images on a Kodak film (7250 tungsten, ASA 400). The E-10/EE is equipped with a trigger pulse generator and optical pick-up to trigger the copper laser at 5 kHz and synchronize action with the film frame rate at 5000 frames per second (fps).

For the flow visualization, intake air is seeded using smoke produced by a generator. For the LDV measurements light is scattered by titanium dioxide particles which have been put in aerosol form using a TSI model 3400 particle generator. A cyclone has been installed at the outlet of the particle generator to remove particles above 5 μm in diameter.

An electronic timing system is used to switch the thyratron driver from internal to external mode. In the external mode the pulse generator of the camera triggers the laser during the filming process. At the end of the film the timing control switches the laser back to the internal mode. Also, the synchronization system will be used to control the operation of the solenoid valve for a preset number of crank angles. A more detailed description of the experimental setup and the electronic timing system is given in [7].

RESULTS AND DISCUSSION - In this section a preliminary visual study of the air flow field during the intake and compression strokes in the rotary engine will be presented at a shaft speed of 230 rpm and at film speed of 1700 fps. Intake and exhaust pressures were at ambient condition. A series of photographs have been taken from the 16 mm movie in a sequential order and are shown to facilitate understanding the air flow characteristics. Rotor angle information was not available for this series of tests.

Figures 3(a) and (b) show the flow behavior during the early stage of the intake process. At this rotor location it is noted that the fluid is entrained by the velocity field induced by the rotor and moving inward toward the rotor pocket. This fact is attributed to a low pressure dominating the intake region. The effect of the rotor position relative to the intake port on the flow field is illustrated in Figures 3(c) and (d). These figures indicate movement of the flow toward the boundary of the rotor housing, and the formation of the counter flow vortices. This is a consequence of the interaction between the rotor and the entrained fluid. Also, an

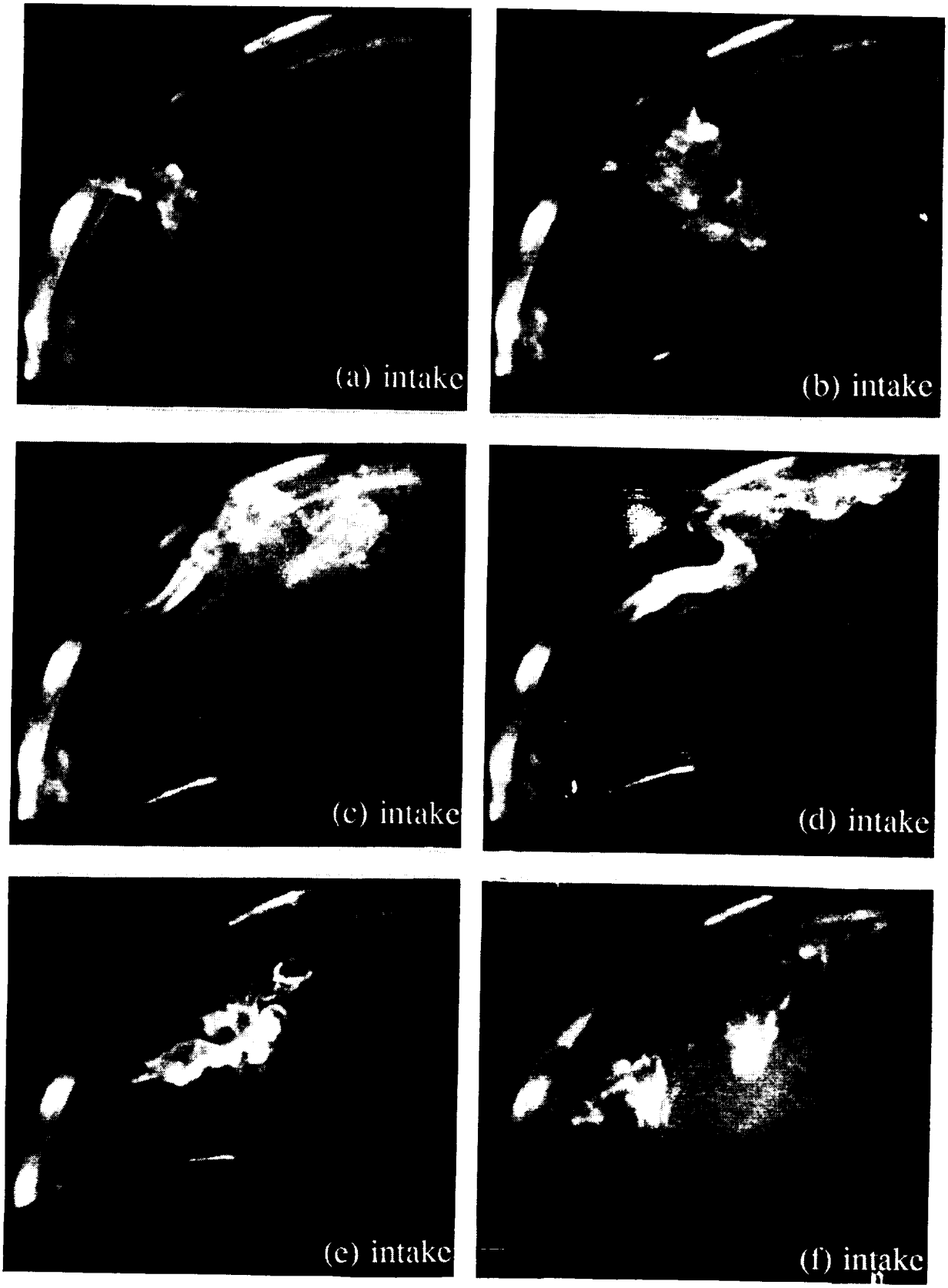

Figure 3 Flow pattern inside the rotary engine during the intake at 230 rpm

ORIGINAL PAGE IS
OF POOR QUALITY

Machinery Resolver (Model 1998), a counter type processor (Model 1990), and Master Interface (Model 1998A), all manufactured by TSI, Inc. The equipment collects and processes the data coming from the photomultiplier and sends the velocity and position data to the IBM PS/2 80, where it can be manipulated using the TSI Rotating Machinery Program (RMP). This program allows the display of velocity data with respect to encoder position, or the data can be displayed in histogram form at a specified encoder position. The current RMP program allows the calculation of the ensemble averaged measurement of the mean velocity and the turbulence intensity. Other statistics available are total number of points, standard deviation, 3rd and 4th moments about the mean, skewness, and flatness. The program also allows the setting of windows to avoid taking data when the control volume is being blocked by a mechanical part.

The sapphire windows being used to gain optical access to the chamber of the rotary engine have caused concern about future flow measurements. Sapphire possesses a single optic axis and the ordinary and extraordinary rays within the sapphire are each linearly polarized [9]. The polarization rotations experienced by the ordinary and extraordinary rays within the material are determined by the direction of the propagation of the incident light, the direction of the optic axis, and the direction of the normal to the window surfaces. They are independent of the polarization of the incident light. Thus, it is possible to orient the polarization of an incident laser beam so that within the sapphire its polarization direction is identical to the polarization direction of either the ordinary ray or the extraordinary ray. For such a matching of initial conditions, the light transmitted into the sapphire will have 100 percent of its amplitude fed into one of the two modes and 0 percent of its amplitude fed into the other of the two modes. Although both modes of propagation within the sapphire are mathematically and physically allowed, the initial conditions are arranged so that only one of them occurs.

This system is in the final stages of debugging. Data has been taken within the motored RCE assembly. Figures 6(a) and (b) show the mean and RMS velocity components u and v respectively, for a rotor speed of 230 rpm, and a measurement volume near the intake zone. Figure 7 gives the location of the LDV velocity measurement and the crank angle coordinate systems used for the results presented.

Both plots, Figures 6(a) and (b), indicate a high velocity during the early stage of the intake (to ~ 90 deg) with a drop in velocity as the intake process progresses. The results are in general agreement with what was seen in the flow patterns during intake at the same operating conditions. Figure 3(a) shows the flow pattern during the early stage of intake where the flow is dominated by the rotor motion and the velocity is maximum. Figure 3(b) shows the flow changing direction and moving toward the rotor pocket, due to a pressure gradient between the intake port and the leading apex, which is accompanied by a drcrease in velocity. This trend is shown in Figure 6(b), where the v-component of the velocity decreases sharply near 140 deg. Figures 3(c) and (d) show the induced flow becoming laminar near the intake port. Figure 6(b) indicates this behavior as the v-component reaches a local maxi-

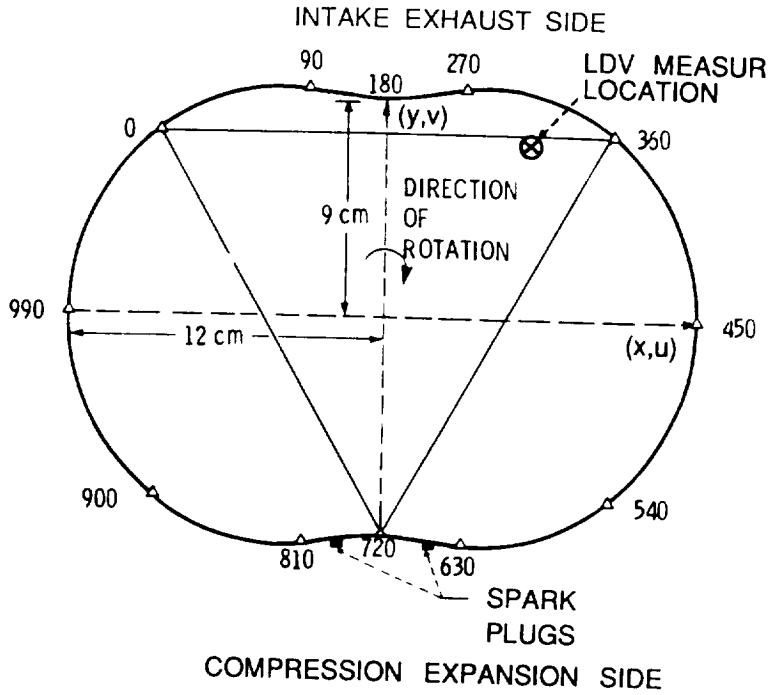

ORIGINAL PAGE IS
OF POOR QUALITY

Figure 7 Trochoidal characteristics dimensions and labeling

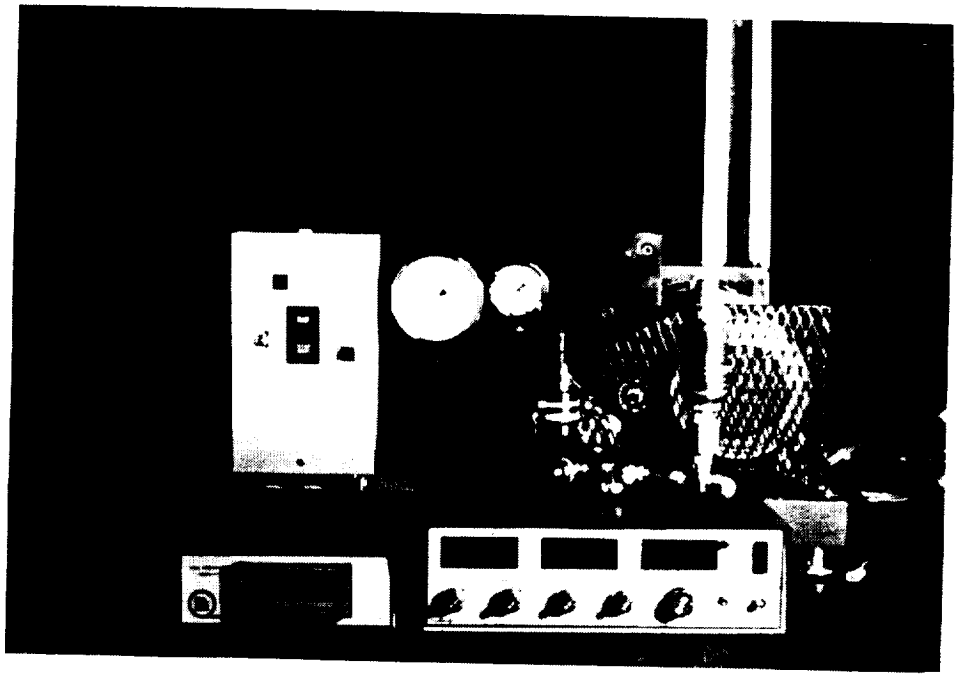

Figure 8 BKM servojet fuel injection system

made. The fuel injector was operated at 100 Hz. The period from the start of one injection event to the start of the next injection event is thus 0.01 sec. During this time 50 frames are exposed with the high speed camera operating at 5000 Hz. Figure 9 shows representative frames from two 50 frame injection events. The second event is designated with a ('). In Figure 9(a) one sees a bright area near the fuel injector which is the start of the injection event on labeled time = 0.0 ms. In the first frame of the two injection events, shown in Figures 9(a) and 9(a'), one also observes on the right hand side the previous injection event. Here the large particles are seen to follow the cloud of more dense small particles. Assuming that the scattered light is representative of the fuel mass, one clearly sees a difference in the structure and mass of the fuel at the end of injection event shown on the right hand side of 9(a) and 9(a') . Frames (b) through (g) show the development of the fuel spray with time. As the photographs use the same scale, again substantial spatial variations in the two injection events can be observed. The major part of the injection event was found to take place in about 1 ms. However, large fuel droplets continued to flow from the injector during the 9 ms immediately following the main part of injection. This could lead to incomplete or late combustion, resulting in excessive emissions and poor performance. Of particular relevance is the mass fraction of fuel that these particles represent. Observation of Figure 9(b) shows that while there is flow from all six nozzle holes, these flows did not begin simultaneously. As about 8000 frames were examined, the phenomenon of non-simultaneous (all six holes at once) firings was found to occur regularly. Throughout the development of the jet it is apparent that different physical phenomena are underway. An early estimate of the velocity of the particle in this jet ranges from 75 to 150 m/s within the same jet. This poses a serious question about the type of model which should be used to describe a fuel spray. This nonconsistency is due in some way to the mechanical phenomena which occur in the mechanical parts of the injector. Finally, from the film it is clear that the 8 mj pulse of the copper vapor laser will provide a properly exposed film.

The next major effort concerning fuel spray flow visualizations will be to adapt this system to visualize flows within the rotary combustion engine.

SUMMARY

Flow visualization systems which allow one to observe planar airflow patterns and high speed fuel jets have been demonstrated. The physical processes involved with the formation of the roll-up vortex during the compression will have an important effect on the level of turbulence in the combustion chamber of the engine during the initial combustion period. This roll-up vortex has not been observed numerically. Another result of this study has been to identify the fuel injector as an important possible source of cycle-to-cycle variability within the RCE. This will have significant influence on operational lean-limit of engines which use this type of injection system. Also, those who use numerical simulations to describe and predict the performance of I.C. engines must develop models which are representative of the physical characteristics of the injector. Future work at the MSU Engine Research Lab will integrate LDV measurements with the flow visualization described.

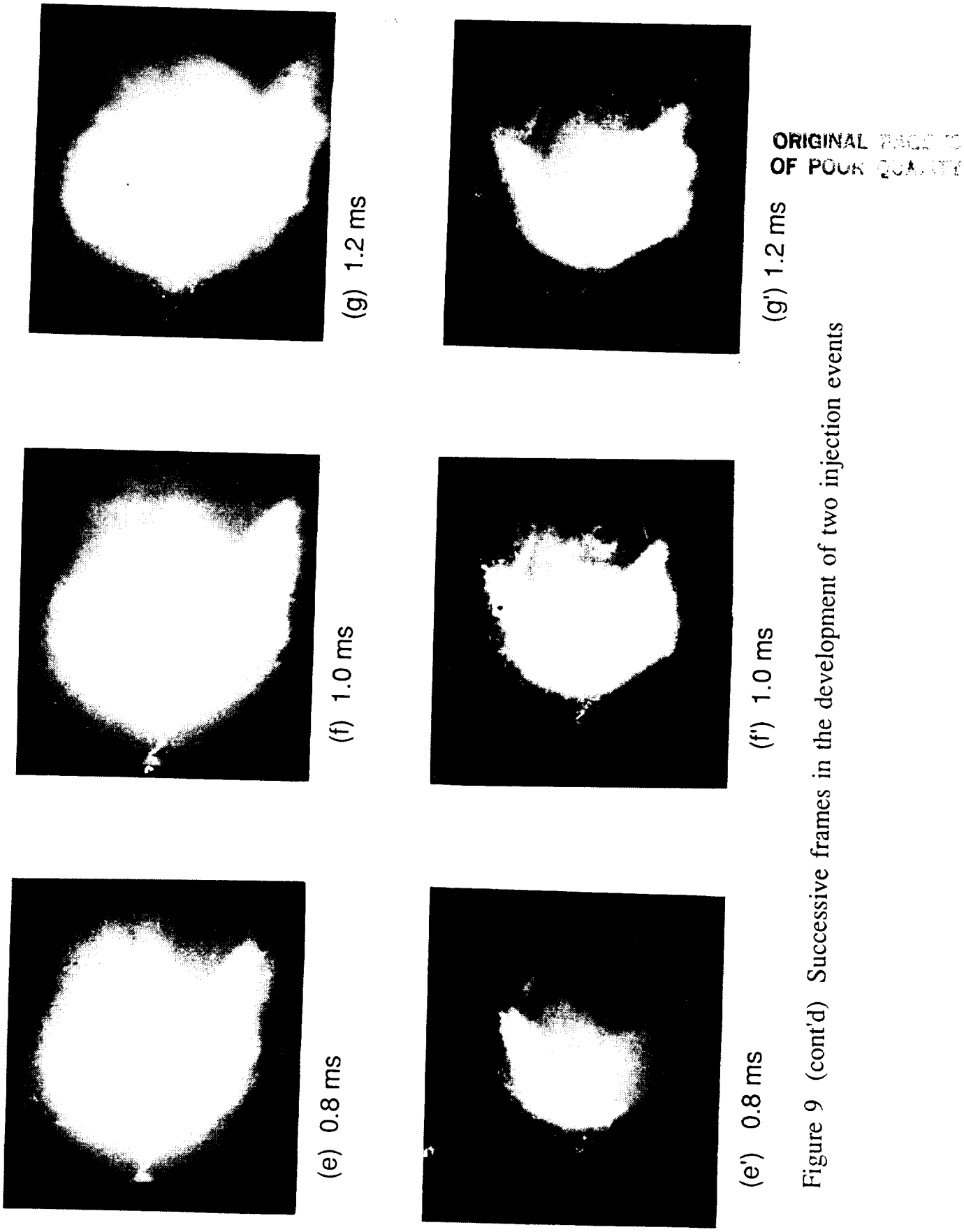

ORIGINAL PAGE IS
OF POOR QUALITY

Figure 9 (cont'd) Successive frames in the development of two injection events

Appendix C

LDV measurements are bound under a separate cover. The data includes:

U component of velocity for 9 locations

V component of velocity for 9 locations

Other statistical parameters: standard deviation, histograms, number of points per crank angle

Appendix D

SAMPLE INPUT AND OUTPUT USING A NUMERICAL SIMULATION OF A ROTARY COMBUSTION ENGINE

JAC ALAMEDDINE
WILLY BIBERSTEIN
ARNIE MUSCAT
June 2, 1989
ME 422

DESCRIPTION OF PROGRAM INPUT VARIABLES

Fire	.TRUE	Engine is firing
	.FALSE	Engine is motored
SPBURN	.TRUE	True for MIT computer version
IHTPRO	3	For heat transfere data
IRTPRO	1	For heat transfere data
FUELTP	1	Indicates fuel is isoctane
PHISTA	Var	OVERALL MASS EQUIVALENCE RATIO
ECCEN	1.542	Eccentricity
ROTRAD	10.64	Rotor radius
DEPTH	7.711	Chamber depth
VFLANK	64.07	rotor pocket volume
RPM	Var	ENGINE SPEED
TIPO	-626.3	Crank angle at which intake port opens
TIPC	-229.5	Crank angle at which intake port closes
TEPO	208.7	Crank angle at which exhaust port opens
TEPC	610.5	Crank angle at which exhaust port closes
TSPARK	-25.0	Crank angle at which spark fires
THIPO	37.0	Duration at which intake port is open
THEPO	42.0	Duration at which exhaust port is open
IPA	11.42	Intake cross sectional area
EPA	9.29	Exhaust port cross sectional area
XBZERO	0.0003	Arbitary, small value of burnt mass
XBSTOP	0.995	Percentage of mass fuel burnt (near 1)
TMAX	21.0	Crank angle at which the max heat rate occurs

DQDTMX	0.029	Max fuel heat release rate
PATM	1.014	Ambient pressure
TATM	300.0	Ambient temperature
PIM	Var	INTAKE MANIFOLD PRESSURE
TFRESH	315.37	Temperature of fresh air
TEGR	300.0	Temperature of recirculated exhaust gass
EGR	0.0	Percentage of recirculated exhaust gass
PEM	1.3	Exhaust manifold pressure
TROTI	300.0	Rotor temperature
TSIDE	436.48	Side housing temperature
THOUSI	436.48	Trochoid housing temperature
CONHT	0.0001	The constant c
EXPHT	0.08	The constant exponent e
TPRINT	20.0	Interval between outputs to file ROTARY.OUT
TPRNIX	2.0	Interval between filing combustion and expansion
ARETOT	0.002	Error tolerance used in subroutine ODERT
CIINTG	0.0001	Error tolerance used in subroutine ODERT
CCINTG	0.0001	Error tolerance used in subroutine ODERT
CBINTG	0.00005	Error tolerance used in subroutine ODERT
CEINTG	0.0001	Error tolerance used in subroutine ODERT
MXTRY	10.0	Currently not used
REL	0.002	Error tolerance used in subroutine ODERT
MAXITS	Var	NUMBER OF ITERATIONS

MAXERR	0.03	Max error in temp calculation of intake & exhaust
AREALK	0.01	Total leakage area per cylinder
CREVOL	0.573	Total crevice volume per cylinder
TCREV	500.0	Estimated average crevice volume temperature
CON1	0.4	Constant used to calibrate heat transfer rate
CON2	0.5	Constant used to calibrate heat transfer rate

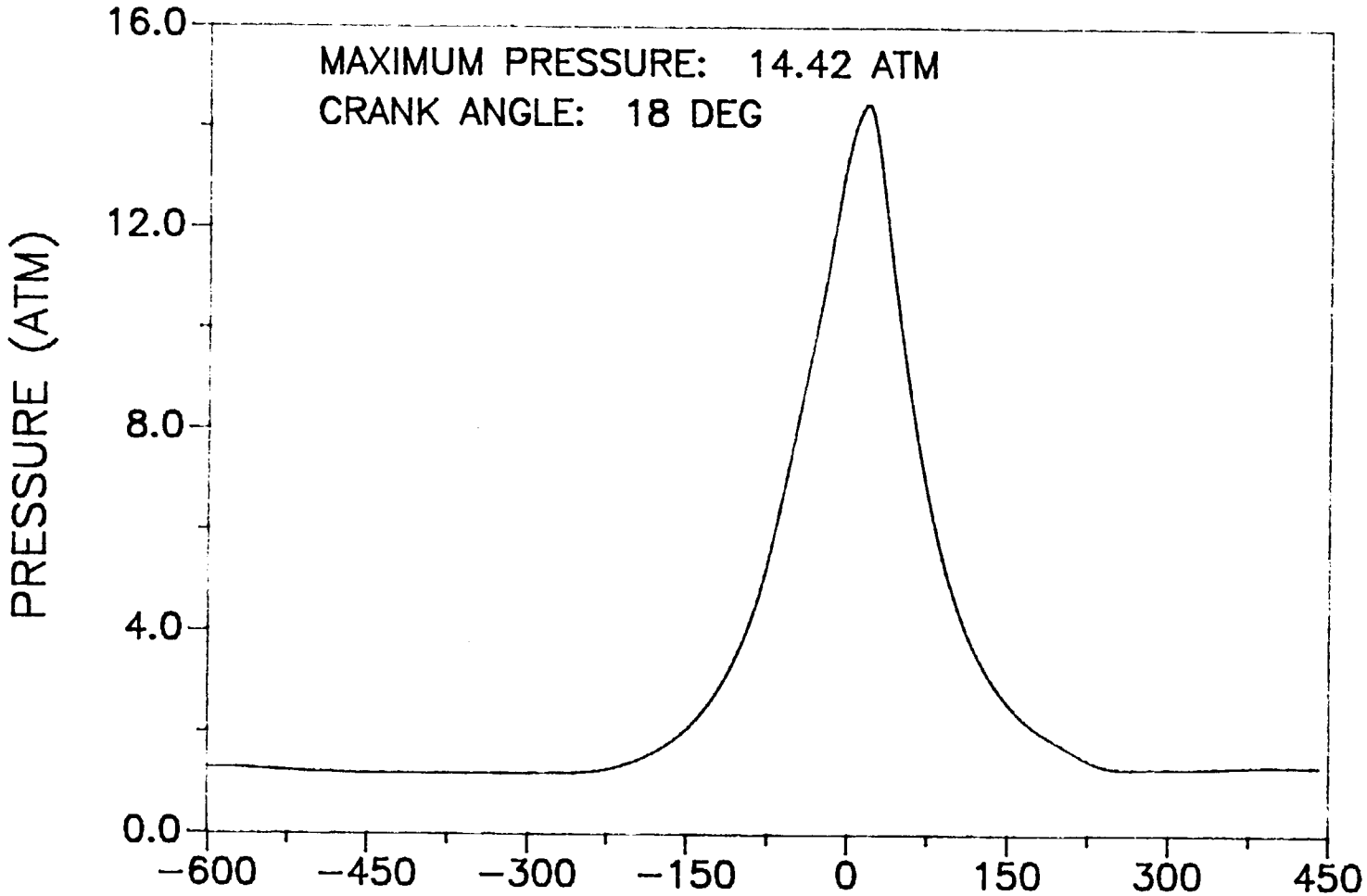

ENGINE SPEED = 4500 RPM
EQUIVALENCE RATIO = 0.85
INTAKE MANIFOLD PRESSURE = 1.2 ATM

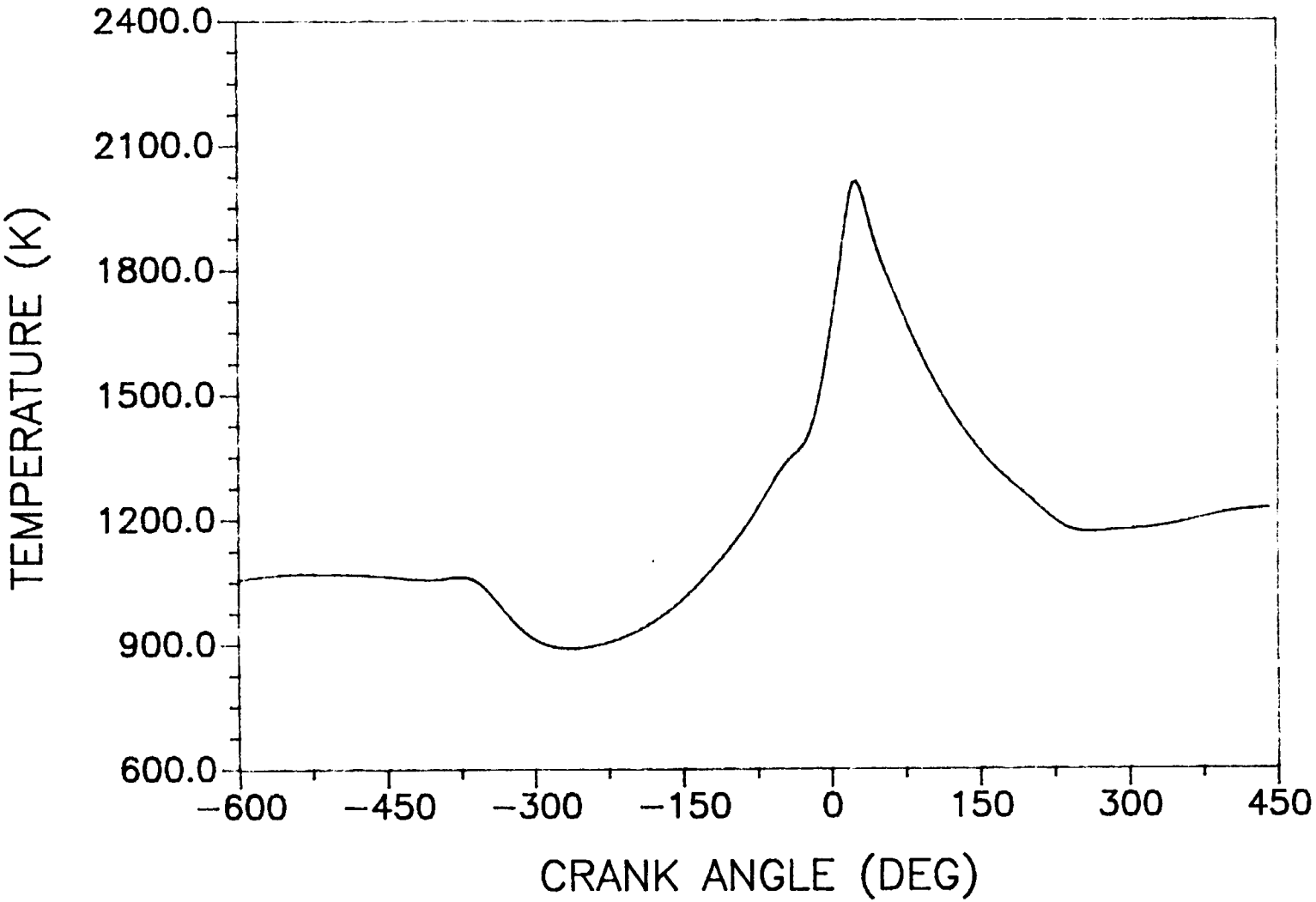

ENGINE SPEED = 4500 RPM
EQUIVALENCE RATIO = 0.85
INTAKE MANIFOLD PRESSURE = 1.2 ATM

Ø	P ATM	WORK KJ	HEAT KJ	T_{ex} °K	ISFC lbm/hp-hr	IMEP ATM	PMEP ATM	T_{MAX} °K	P_{MAX} ATM
.80	1.1	UNDERFLOW ERROR							
.85	1.1	"							
.90	1.1	"							
.95	1.1	"							
.80	1.2	"							
.85	1.2	"							
.90	1.2	"							
.95	1.2	"							
.80	1.3	.39954	.23097	1358.5	.422	6.910	-.027	2526.36	35.7
.85	1.3	.39710	.25465	1413.0	.433	6.867	-.026	2590.79	35.5
.90	1.3	.38832	.28386	1509.7	.450	6.720	-.03	2644.85	35.2
.95	1.3	—	—	—	—	—	—	—	—

ORIGINAL PAGE IS
OF POOR QUALITY

3500 RPM

Ø	P	WORK Joules	HEAT Joules	T_{ex} °K	ISFC lbm/Bhp-hr	IMEP ATM	PMEP ATM	T_{MAX} °K	P_{MAX} ATM
.80	1.1	NEGATIVE WORK							
.85	1.1	"							
.90	1.1	"							
.95	1.1	"							
.80	1.2	UNDERFLOW ERROR							
.85	1.2	"							
.90	1.2	"							
.95	1.2	"							
.80	1.3	43.78	21.88	1351.3	.406	7.58	-.038	2504.9	37.2
.85	1.3	439.0	241.21	1405.1	.415	7.60	-.037	2574.7	37.4
.90	1.3	436.7	275.4	1513.5	.426	7.5	-.042	2630.8	37.1
.95	1.3	KILL ÷ BY ZERO							

ORIGINAL PAGE IS OF POOR QUALITY

4000 RPM

Ø	P	WORK Joules	HEAT Joules	T_{ex} °K	ISFC lbm/Bhp-hr	IMEP ATM	PMEP ATM	T_{MAX} °K	P_{MAX} ATM
.80	1.1	KILL ÷ BY ZERO							
.85	1.1	"							
.90	1.1	"							
.95	1.1	"							
.80	1.2	UNDERFLOW ERROR							
.85	1.2	"							
.90	1.2	"							
.95	1.2	"							
.80	1.3	466.98	208.28	1346.7	.394	8.098	-.053	2498.44	38.4
.85	1.3	471.22	229.72	1399.8	.403	8.169	-.052	2563 30	38.5
.90	1.3	474.62	257.35	1458	.411	8.227	-.050	2619.63	38 6
.95	1.3								

ORIGINAL PAGE IS
OF POOR QUALITY

4500 RPM

Ø	P	WORK Joules	HEAT Joules	T_{ex} °K	ISFC lbm/hp-hr	IMEP ATM	PMEP ATM	θ_{dQ}^{MAX}	$\theta_{.}^{MAX}$ ATM
.80	1.1	UNDER-FLOW ERROR							
.85	1.1	"							
.90	1.1	"							
.95	1.1	"							
.80	1.2	53.75	83.35	1252.6	.654	1.064	-.138	2076.27	15.2
.85	1.2	40.32	80.57	1330.4	.750	.832	-.137	2050.16	14.4
.90	1.2	31.81	78.35	1403.5	.846	.685	-.137	2028.90	14.0
.95	1.2	27.50	77.43	1468.4	.921	.611	-.137	2027.37	13.8
.80	1.3	488.64	198.66	1343.5	.387	8.490	-.072	2488.98	39.3
.85	1.3	497.85	220.30	1396.8	.394	8.648	-.071	2555.31	39.6
.90	1.3	503.16	246.54	1454.0	.402	8.737	-.069	2611.51	39.8
.95	1.3	519.16	258.79	1466.2	.410	9.027	-.083	2655.45	41.6

ORIGINAL PAGE IS OF POOR QUALITY

DRAFT
7/6/89

A COMPUTER ANALYSIS OF BEARING FRICTION

DAVID CALDWELL 0957574
ERIC PEKRUL 1065934
TIM BURKE 0946873
KEVIN DOWDING 1002239

ABSTRACT

A Computer program was designed to simulate bearing loads and their contribution to friction for a Wankel rotary engine. A useful result of this simulation is the ability to compare the performance of a known engine with that of a new design. This simulation will indicate how well
a new design will perform without having to build expensive prototypes.
The loads imposed on the bearings will result from gas pressure variations and also form inertia forces caused by the eccentric rotation of the rotor itself. This report identifies methods used to simplify and model these loads. Once these loads are calculated, hydrodynamic lubrication can be used to ascertain the friction loss in the bearings.
Reductions in engine friction can, improve engine thermal efficiency and thereby reduce vehicle fuel consumption. The results of this study have shown that with this computer simulation, the design engineer can quickly vary the key parameters associated with bearing design, and ultimately attain a solution which minimizes friction loss.

TABLE OF CONTENTS

ABSTRACT
INTRODUCTION ..... Page 1
ANALYSIS ..... Page 2
PROCEDURE ..... Page 5
RESULTS ..... Page 6
DISCUSSION ..... Page 7
CONCLUSION ..... Page 8
REFERENCES ..... Page 9
APPENDIX A
APPENDIX B

INTRODUCTION

The term ' performance' for an engine has many implications. Power, fuel consumption reliability, weight, size, cost immediately come to mind. Friction, in one way or another effects or is effected by all of the above considerations. The study of friction in an engine is therefore an important design consideration from both a design or a performance stand point.

This report and program, which calculates friction losses in bearings, is part of a larger project to study the friction losses in a rotary I.C. engine. The report deals with rotor and main hydrodynamically lubricated bearings (plain bearings), and is not applicable to rolling element bearings (roller or ball bearings). This specific type of internal combustion engine has friction created by the apex seals, main and rotor bearing, and ancillitory losses. Although bearing friction accounts for a small fraction of the overall friction consideration of an internal combustion engine it should not be ignored completely in any calculation. The context of this program is to estimate the bearing friction of a rotary engine.

ANALYSIS

The program focuses on the output shaft, rotor, and there bearings. For internal combustion engines to be operated over a wide range of revolutions under severe load conditions, plain bearings of babbit metal or aluminum alloy that use hydrodynamic lubrication are generally used and this is the type of bearing which our program estimates. The frictional force in the bearings can be calculated using the following equation:

$$F = (2\pi\ U R L) / [(1+\epsilon)^{1/2} C] + [(Ce\ W) / 2R] \sin\phi \quad (1).$$

U = viscosity R = Journal radius L = Axial length
C = radial clearance

The typical range for these parameters can be found in appendix A.

Test have shown that temperature rise in reliable bearing design usually does not exceed 50^0 F, therefore, the viscosity of the oil in the bearing can be estimated. Knowing the viscosity, the bearing dimension, and the speed of the rotor we can calculate the film thickness.

$$h = (W A U) / F \quad (2).$$

With this fluid film thickness the eccentricity ratio can be calculated:

$$e = (C - h) / C \qquad (3).$$

All the parameters can be seen on figure 1.

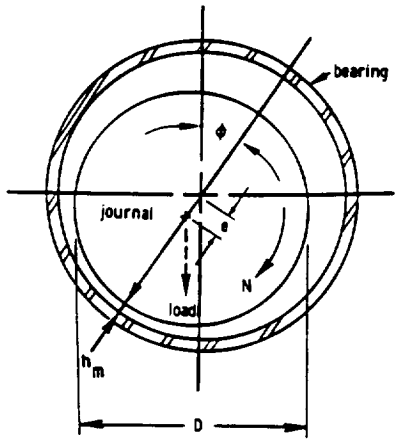

After studying an orbital diagram we were able to assume an attitude angle . Initially film thickness (h) was estimated as 25% of the radial clearance (C) and this was used in egs (2) to calculate eccentricity ratio (e) which was then used in eqs (1) to calculate friction (F). Then the equation for hydrodynamically lubricated contacts:

EQ 2 should be 2 $\qquad h = uAU/F$

to give the film thickness. An iterative process was then implemented to get values of friction (F) and film thickness (h) within 1% of the previous values.

The analysis of the frictional effects of the rotor and main bearings will remain the same due to similar design (hydrodynamic lubrication),the loading analysis, however will be different. To get the average gas loading on the rotor bearing for a given horsepower and rpm the annihilatory forces were first added . The torque was then calculated from the formula:

$$T = (hp \quad \frac{33,000}{\cancel{33,00}}) \; / \; (2 \; \pi \quad rpm)$$

(4).

Now the ave gas load on the rotor bearing can be calculated by dividing the torque by the crank radius (R) of the output shaft. To get the total load on the rotor bearing the magnitude of the resultant of the average gas loading and inertial loading was calculated. The only inertial load on the rotor bearing large enough to be of consequence can be obtained from the equation:

$$F_i = M R (w)^2 \quad (5).$$

M = mass of rotor assy. incl. oil
R = crank radius (ft)
w = absolute angular velocity of rotor

Because the analysis is using an assumed @ and an average gas load only the magnitude of the resultant force is of importance.

Since the rotary engine gas no reciprocating motion, only rotational, the inertial forces at the main bearings can be counterbalanced completely. Therefore, the only loading on the main bearing will be due to the average gas load.

PROCEDURE

The steps for the procedure were as follows:

1) Enter input parameters
   a) combined weight of rotor, oil, and seals. (lb. mass)
   b) crank radius (ft)
   c) viscosity of oil (lb/ft^2)
   d) rotor journal diameter (ft)
   e) main journal diameter (ft)
   f) axial length of main bearings (ft)
   g) axial length of main bearings (ft)
   h) radial clearance of rotor bearing (ft)
   i) radial clearance of main bearing (ft)
   j) assumed attitude angle (degrees)

2) Enter desired input, horsepower and revolutions per minute, of engine.

Typical values that are used in this report are in appendix B.

Mazda RX-7 Shop Manual 30 wt. o.i. } Journal sizes, clearance crank radius

Power curve taken from "Rotary Engine" Kenichi Yamamoto p. 38, fig. 4.3 (divided in half)

RESULTS

ORIGINAL PAGE IS
OF POOR QUALITY

The results of our simulation include the wide open throttle and 75% ~~throttle~~ power operation of a 537cc twin rotary engine of which we took 50% of the total power output to determine the frictional horsepower losses in the main and rotor bearings. The results of these simulations are shown in table 1.

Values found for Wide Open Throttle (a)
Values found for 75% Throttle (b)

RPM	* 1/2 of Values taken from power curve p.38 fig. 4.3 ↓	Estimated ~~Accessory~~ losses Ancillary	Main Bearing Friction Force M_{force} (lb)	Rotor Bear. Friction Force R_{force} (lb)	Total Friction Hp. in both bearing T (hp)
a) 7000	65	-+7	2.21	10.59	1.914
6000	63	-+6	2.01	8.63	1.354
5000	57	-+5	1.79	6.84	.907
4000	47	-+4	1.54	5.22	.563
3000	33	-+3	1.25	3.77	.31
2000	20	-+2	.95	2.51	.141
1000	9	-+1	.64	1.42	.041
b) 7000	49	~~65~~ - 7	2.12	10.58	1.903
6000	47	~~63~~ - 6	1.90	8.61	1.392
5000	43	~~57~~ - 5	1.67	6.81	.896
4000	35	~~47~~ - 4	1.42	5.17	.552
3000	25	~~33~~ - 3	1.14	3.70	.301
2000	15	~~20~~ - 2	.85	2.40	.134
1000	6	~~8~~ - 1	.56	1.32	.038

* Taken from "Rotary Engine" Kenichi Yamamoto

DISCUSSION

This computer program does have a limitation. It only considers a one rotor, two main bearing rotary engine. However, techniques associated with this computer program can be used for multiple rotors and main bearings. In this case the horsepower can be divided by the number of bearings.

It can be observed from the results that the first term in the friction equation (EQ.), is dominant. This means the shaft speed is more influential than horsepower.

The design parameters that were taken into consideration, and can be varied to obtain various results include:

1) Bearing Size
   a) diameter
   b) axial length
2) Clearance
3) Viscosity

CONCLUSIONS

The following conclusions can be drawn from the results of this study and numerous simulation runs.

1) Engine speed is dominant over horsepower on frictional losses.

2) Friction loss increases with increasing speed and horsepower.

3) Friction increases as bearing size increases.

4) Friction increases with increasing viscosity.

5) Friction increases as radial clearance decreases.

REFERENCES

Arnold O. Dehart and Duane H. Hqrwick,
" Engine Bearing Design: 1969", SAE paper 690008

Richard C. Rosenberg, "General Friction Considerations for Engine Design", SAE paper 821576

Kenichi Yamamoto, "Rotary Engine",
Sankaito Co. Ltd, 1981

APPENDIX A

ORIGINAL PAGE IS
OF POOR QUALITY

```
BURNS
PROGRAM BEARINGS
ANGLEM  - ATTITUDE ANGLE MAIN BEARING
ANGLER  - ATTITUDE ANGLE ROTOR BEARING
ANGVEL  - ANGULAR VELOCITY
AREA    - ACTUAL AREA OF BEARING SURFACE CONTACT
CRAING  - RADIAL CLEARANCE OF MAIN BEARING
CROTOR  - RADIAL CLEARANCE OF ROTOR BEARING
CRKRAD    CRANK RADIUS (ECCENTRICITY OF ROTOR)
DIARTJ  - DIAMETER OF ROTOR JOURNAL
DIAMNJ  - DIAMETER OF MAIN JOURNAL
ELASLM  - ELASTIC LIMIT (YIELD PRESSURE) OF BEARING MATERIAL
ERATIO  - ECCENTRICITY RATIO
FGAS      GAS FORCE
FINERT  - INERTIA FORCE
FLOAD   - TOTAL LOAD ON ROTOR BEARING
FRCTNM  - FRICTION FORCE IN MAIN BEARING
FRCTNR  - FRICTION FORCE IN ROTOR BEARING
HELP1 -4- SIMPLIFYING VARIABLES
HPANSL  - HORSEPOWER CONSUMED BY ANSILLARIES
HPROTR  - HORSEPOWER GENERATED BY ROTOR
HPSHFT  - HORSEPOWER GENERATED BY SHAFT
LNGTHM  - AXIAL LENGTH OF MAIN BEARING
LNGTHR  - AXIAL LENGTH OF ROTOR BEARING
MASS    - MASS OF ROTOR, OIL, SEALS, PUMPS, ETC.
RADMNJ  - RADIUS OF MAIN JOURNAL
RADRTJ  - RADIUS OF ROTOR JOURNAL
RPM     - REVOLUTIONS PER MINUTE OF ENGINE
THICKM  - FILM THICKNESS IN MAIN BEARING
THICKR  - FILM THICKNESS IN ROTOR JOURNAL
TRQSFT  - TORQUE GENERATED BY OUTPUT SHAFT
TRQTRU  - TORQUE GENERATED ON THE ROTOR
VELM    - SURFACE VELOCITY OF JOURNAL IN MAIN BEARING
VELR    - SURFACE VELOCITY OF JOURNAL IN ROTOR BEARING



      REAL RPM,HPSHFT,HPANSL,WEIGHT,CRKRAD,VISCOS,ANGVEL,MASS,PI,FTOTAL
      INTEGER CHOICE,DTEST,MAINHP


      OPEN(7,FILE='PRN')
10    CONTINUE
      PRINT*,'WELCOME TO THE BEARING FRICTION PROGRAM'
      PRINT*,'      '
      PRINT*,'*** BE SURE TO ENTER ALL NUMBERS AS REAL VALUES ***'
      PRINT*,'    '
      PRINT*,'ENTER THE ENGINE SPEED (RPM)'
      READ(*,*)RPM
      PRINT*,'ENTER THE SHAFT HORSEPOWER (HP)'
      READ(*,*)HPSHFT
      PRINT*,'ENTER THE HORSEPOWER LOST TO THE ANSILLARIES (HP)'
      READ(*,*)HPANSL
      PRINT*,'ENTER THE COMBINED WEIGHT OF ROTOR, OIL, SEALS (LB)'
      READ(*,*)WEIGHT
      PRINT*,'ENTER THE CRANK RADIUS (ECCENTRICITY OF ROTOR (IN)'
      READ(*,*)CRKRAD
      PRINT*,'ENTER THE KINEMATIC OIL VISCOSITY'
      READ(*,*)VISCOS

C     *** INITIALIZE VARIABLES ***
```

```
      PI=3.14159265
      ANGVEL=(2.0*PI*RPM)/60.0
      MASS=WEIGHT/32.174
C
7     CONTINUE

      PRINT*,'     '
      PRINT*,'(1)  SOLVE FOR THE ROTATING FRICTION PROBLEM'
      PRINT*,'(2)  CHANGE THE DATA ENTERED ABOVE'
      PRINT*,'(3)  QUIT THE PROGRAM'
      PRINT*,'     '
      PRINT*,'ENTER THE NUMBER OF YOUR CHOICE'

      READ(*,*)CHOICE
      IF (CHOICE.EQ.1) THEN
      CALL ROTOR(RPM,HPSHFT,HPANSL,RADIUS,RAD,VISCOS,PI,ANGVEL,MASS,FRCTNR,
     &   ROTRHP)
      CALL BERING(RPM,HPSHFT,HPANSL,RADIUS,RAD,VISCOS,PI,ANGVEL,
     &   MASS,FRCTNM,MPRSHP)

       CALCULATE TOTAL HORSEPOWER LOST IN FRICTION

      HPLOST = ROTRHP + MPMAIN

      PRINT*,'RESULTS OF TOTAL FRICTION ANALYSIS'
      WRITE(7,301)
      PRINT*,'     '
      WRITE(7,303)
      PRINT*,'     '
      WRITE(7,303)
      PRINT*,'THE HORSEPOWER LOST TO FRICTION = ',HPLOST
      WRITE(7,302)HPLOST
01    FORMAT(20X,'***RESULTS OF TOTAL FRICTION ANALYSIS***')
02    FORMAT(20X,'THE HORSEPOWER LOST TO FRICTION = ',F7.3)
03    FORMAT(20X,'     ')

         PRINT*,'     '
         WRITE(7,303)
         WRITE(7,303)
         PRINT*,'**********  ************************************'
         WRITE(7,304)
04       FORMAT(20X,'****************************************')
         PRINT*,'     '
         WRITE(7,303)
      ELSEIF (CHOICE.EQ.2)THEN
         GO TO 10
      ELSEIF (CHOICE.EQ.3) THEN
         PRINT*,'ARE YOU SURE YOU WANT TO QUIT (Y=6 - N=7) ?'
         READ(*,*)QTEST
         IF (QTEST.EQ.6) THEN
            GOTO 20
         ELSE
            GOTO 77
         ENDIF
      ELSE
         PRINT*,'PLEASE TRY AGAIN'
         GOTO 77
      ENDIF

      GO TO 77

C     CONTINUE
       END
```

ORIGINAL PAGE IS
OF POOR QUALITY

```
      SUBROUTINE ROTOR(RPM,HPSHFT,...,GSL,CRKRAD,VISCOS,PI,ANGVEL,
     C     MASS,FRCTNR,...,TRUF)
      DIMENSION FRCR(100)
      REAL LNGTHR,DIARTJ,CROTOR,...,TROSFT,TROTRU,HPROTR,FGAS,
     C  FINERT,FLOAD,CLRNSLN,AREA,...,HELPIR,HELPOR,HELPSR,
     C  HELPAR,VELR,FRCTNR,ERATIO,...,CONVRG,VISCOS,MASS,
     C  RPM,HPSHFT,HPANGL,CRKRAD,PI,...
```

ORIGINAL PAGE IS
OF POOR QUALITY

```
      PRINT*,'ENTER THE ROTOR JOURNAL DIAMETER (IN.)'
      READ(*,*)DIARTJ
      PRINT*,' ENTER THE AXIAL LOC... OF THE ROTOR BEARING (IN.)'
      READ(*,*)LNGTHR
      PRINT*,'ENTER THE RADIAL CL...RANCE OF ROTOR BEARING (IN.)'
      READ(*,*)CROTOR
      PRINT*,'ENTER THE ATTITUDE ...E FOR THE ROTOR BEARINGS (DEG.)'
      READ(*,*)ANGLER
      RADRTJ = DIARTJ/2.0

      CALCULATE THE GAS FORCE

      TROSFT  = (63000.0*HPSHFT)/...

         ADD HORSEPOWER LOST IN THE AUXILLARY COMPONENTS SUCH
             AS SEALS, GEARS, PUMPS, ETC.

      HPROTR    = HPSHFT  +  HPANGL

            CALCULATE ACTUAL TORQUE ON THE ROTOR ASSUMING NEGLIGABLE
                SHAFT DEFLECTION

      TROTRU = (63000.0*HPROTR)/R...

       CALCULATE THE LOAD ON THE JOURNAL

      ... = 3.14159/180.0

    NOW CALCULATE THE INERTIAL LOADING

      FINERT = MASS*CRKRAD*(ANGVEL/32.2)**2/12.0

          CALCULATE TOTAL AVERAGE LOAD ON ROTOR BEARING

      FLOAD =  SQRT((FGAS**2.0)+(F...ERT**2.0))
      PRINT*,'THE TOTAL LOAD IS',FLOAD

      CALCULATE  THE ...RICTION FOR... ASSOCIATED WITH HYDRODYNAMIC
      LOADING USING ITERATION LOOP

      ...RGA = LNGTHR*DIARTJ
      THIKR=.25*CROTOR
      HELPIR=4.0*(PI**2.0)*VISCOS*RPM*(RADRTJ**2.0)*LNGTHR/180.0
      I=1
      VELR=ANGVEL*RADRTJ

10    CONTINUE
```

```
      ENTTO=(CROTOR-TRIAL)/CROTOR
      HELP2R=CROTOR*((1.0+ERATIO**2.0)**0.5)
      HELP3R=FLOAD*CROTOR*ERATIO*(SIN(ANGLE))+(COS(ANGLE))
      HELP4R = HELP1R/HELP2R
      FRCR(I)=HELP3R(HELP4R
```

ORIGINAL PAGE IS
OF POOR QUALITY

```
      IF(I.ST.1)THEN
      ITEMP=I-1
      ENDIF
      IF(I.EQ.1)THEN
      CONVRG=1
      GO TO 35
      ENDIF

      CONVRG= (ABS(FRCR(I)-FRCR(ITEMP))/FRCR(I)

 5    CONTINUE

C          CHECK THE ITERATION FORMULA
           PRINT*,'THIS IS THE CONVERGENCE',CONVRG
           WRITE(*,*)CONVRG

      IF(CONVRG.LT..01)THEN
      GO TO 40
      ENDIF

      THICKR=(VISCOS*AREA*VELR)/FRCR(I)
      I=I+1

      GO TO 30

 0    CONTINUE

      FRCTNR=FRCR(I)

C CALCULATE THE HORSEPOWER LOST DUE TO FRICTION IN ROTOR

      ROTHP = (FRCTNR*RADRTJ*RPM)/33000.0

C PRINT OUT THE TOTAL FRICTION LOAD IN THE ROTOR BEARING

      PRINT*, '    '
      WRITE(7,104)
      WRITE(7,104)
      PRINT*, '********RESULTS OF ROTOR BEARING FRICTION*******'
      WRITE(7,101)
      PRINT*, '    '
      WRITE(7,104)
 01   FORMAT(20X,'***RESULTS OF ROTOR BEARING FRICTION***')
      PRINT*, '    '
      WRITE(7,104)
      PRINT*, 'ENGINE SPEED = ', RPM,'    HORSEPOWER = ', HPSHFT
      WRITE(7,102)RPM,HPSHFT
 02   FORMAT(20X,'ENGINE SPEED   =  ',F9.3,3X,'HORSEPOWER = ',F7.3)
      PRINT*, '    '
      WRITE(7,104)
      PRINT*, 'THE FRICTION FORCE =', FRCTNR,'LBS.'
      WRITE(7,103)FRCTNR
 03   FORMAT(20X,'THE FRICTION FORCE IS  ',F7.2,' LBS.')
      PRINT*, '    '
```

```
      PRINT*,
      WRITE(7,104)
      WRITE(7,104)
104   FORMAT(20X,'
      RETURN
      END

      SUBROUTINE BEARING(RPM,HPSHFT,...,HPANSL,CRKRAD,VISCOS,PI,ANGVEL,
     &  MASS,FRCTNM,HPMAIN)
      DIMENSION FRCTN(100)
      REAL DIAMNJ,LNGTHM,CMAINB,RADMNJ,TRQSFT,TRQTRU,HPROTR,FGAS,
     &  FINERT,HELP1M,HELP2M,HELP3M,HELP4M,VELM,FRCTNM,ERATIO,ANGLEM,
     &  CONVRG,VISCOS,MASS,RPM,HPSHFT,...,HPANSL,CRKRAD,PI,ANGVEL,HPMAIN
      INTEGER I,ITEMP
      PRINT*,'ENTER THE MAIN BEARING JOURNAL DIAMETER (IN.)'
      READ(*,*)DIAMNJ
      PRINT*,'ENTER THE RADIAL CLEARANCE OF MAIN BEARING (IN.)'
      READ(*,*)CMAINB
      PRINT*,'ENTER THE AXIAL LENGTH OF MAIN BEARING (IN.)'
      READ(*,*)LNGTHM
      PRINT*,'ENTER THE ATTITUDE ANGLE FOR MAIN BEARING (DEG)'
      READ(*,*)ANGLEM

      RADMNJ=DIAMNJ/2.0

      CALCULATE THE GAS FORCE

      TRQSFT=(63000.0*HPSHFT)/RPM
      HPROTR=HPSHFT+HPANSL
      TRQTRU=(63000.0*HPROTR)/RPM
      FGAS=(TRQTRU/(CRKRAD*2.0)


      CALCULATE  FRICTION FORCE ASSOCIATED WITH HYDRODYNAMIC
     LOADING USING ITERATION LOOP

      AREA=LNGTHM*DIAMNJ
      THIKM=.25*CMAINB
      HELP1M=4.0*(PI**2.0)*VISCOS*(RADMNJ**2.0)*LNGTHM/60.0
      I=1
      VELM=ANGVEL*RADMNJ

30    CONTINUE

      ERATIO = (CMAINB - THIKM)/CMAINB
      HELP2M=  CMAINB*(((1.0  - (ERATIO**2.0)))**.5)
      HELP3M=FGAS*CMAINB*ERATIO*(SIN(ANGLEM))/DIAMNJ
      HELP4M= HELP1M/HELP2M

      FRCTN(I)  = HELP3M+HELP4M
      PRINT*,'THIS IS THE FORCE',FRCTN(I)

      IF(I.GT.1)THEN
      ITEMP=I-1
      ENDIF
      IF(I.EQ.1)THEN
      CONVRG=1.0
      GO TO 55
      ENDIF


      CONVRG=(ABS(FRCTN(I)-FRCTN(ITEMP)))/FRCTN(I)

55    CONTINUE

      IF(CONVRG.LT.0.001)THEN
```

ORIGINAL PAGE IS
OF POOR QUALITY

```
      GO TO 20
      ENDIF


      VISC= (VISCOS*AREA*VELM)/(.0254*.1)
      I=1.1

                                                                  ORIGINAL PAGE IS
                                                                  OF POOR QUALITY
      GO TO 50


 5    CONTINUE

      FRCTNM= FRCN()

      HPMAIN= (FRCTNM*RADMNJ*RPM*6.28*2.0

      PRINT*, '     '
      WRITE(7,204)
      PRINT*, '********RESULTS OF MAIN BEARING FRICTION*******'
      WRITE(7,201)
      PRINT*, '     '
      WRITE(7,204)
      PRINT*, '     '
      WRITE(7,204)
      PRINT*, 'ENGINE SPEED =', RPM,    'HORSEPOWER = ', HPSHFT   '
      WRITE(7,202)RPM,HPSHFT
      PRINT*, '     '
      WRITE(7,204)
      PRINT*, 'THE FRICTION FORCE = ', FRCTNM, 'LBS.'
      WRITE(7,203)FRCTNM
      PRINT*, '     '
      WRITE(7,204)


201   FORMAT(20X,'***RESULTS OF MAIN BEARING FRICTION***')
202   FORMAT(20X,'ENGINE SPEED = ',F9.3,3X,'HORSEPOWER = ',F7.3)
203   FORMAT(20X,'THE FRICTION FORCE IS ',F7.2,'  LBS')
204   FORMAT(20X,' ')

      RETURN
      END
```

APPENDIX B

RESULTS OF ROTOR BEARING FRICTION

Engine Output

ENGINE SPEED = 1000.000 HORSEPOWER = 9.000

THE FRICTION FORCE IS 1.42 LBS.

← Rotor bearing friction

RESULTS OF MAIN BEARING FRICTION

ENGINE SPEED = 1000.000 HORSEPOWER = 9.000

Engine output

THE FRICTION FORCE IS 0.64 LBS

← Main bearing friction

RESULTS OF TOTAL FRICTION ANALYSIS

THE HORSEPOWER LOST TO FRICTION = 0.041 ← Total Hp. lost to friction

****

ORIGINAL PAGE IS
OF POOR QUALITY

RESULTS OF ROTOR BEARING FRICTION

ENGINE SPEED = 3000.000 HORSEPOWER = 20.000

THE FRICTION FORCE IS 2.51 LBS.

RESULTS OF MAIN BEARING FRICTION

ENGINE SPEED = 3000.000 HORSEPOWER = 20.000

THE FRICTION FORCE IS 0.95 LBS

RESULTS OF TOTAL FRICTION ANALYSIS

THE HORSEPOWER LOST TO FRICTION = 0.141

****

ORIGINAL PAGE IS
OF POOR QUALITY

RESULTS OF ROTOR BEARING FRICTION

ENGINE SPEED = 3000.000 HORSEPOWER = 33.000

THE FRICTION FORCE IS 3.77 LBS.

RESULTS OF MAIN BEARING FRICTION

ENGINE SPEED = 3000.000 HORSEPOWER = 33.000

THE FRICTION FORCE IS 1.25 LBS

RESULTS OF TOTAL FRICTION ANALYSIS

THE HORSEPOWER LOST TO FRICTION = 0.310

****

ORIGINAL PAGE IS
OF POOR QUALITY

RESULTS OF ROTOR BEARING FRICTION

ENGINE SPEED = 6000.000 HORSEPOWER = 47.000

THE FRICTION FORCE IS 5.22 LBS.

RESULTS OF MAIN BEARING FRICTION

ENGINE SPEED = 6000.000 HORSEPOWER = 47.000

THE FRICTION FORCE IS 1.54 LBS

RESULTS OF TOTAL FRICTION ANALYSIS

THE HORSEPOWER COST TO FRICTION = 0.563

****

ORIGINAL PAGE IS
OF POOR QUALITY

RESULTS OF ROTOR BEARING FRICTION

ENGINE SPEED = 5000.000 HORSEPOWER = 57.000

THE FRICTION POWER IS 5.64 LBS.

RESULTS OF MAIN BEARING FRICTION

ENGINE SPEED = 5000.000 HORSEPOWER = 57.000

THE FRICTION POWER IS 1.77 LBS

RESULTS OF TOTAL FRICTION ANALYSIS

THE HORSEPOWER LOST TO FRICTION = 0.907

****

ORIGINAL PAGE IS
OF POOR QUALITY

RESULTS OF ROTOR BEARING FRICTION

ENGINE SPEED = 6000.000 HORSEPOWER = 43.000

THE FRICTION FORCE IS 8.63 LBS.

RESULTS OF IDLER BEARING FRICTION

ENGINE SPEED = 6000.000 HORSEPOWER = 43.000

THE FRICTION FORCE IS 2.01 LBS

RESULTS OF TOTAL FRICTION ANALYSIS

THE HORSEPOWER LOST TO FRICTION = 1.354

****

ORIGINAL PAGE IS
OF POOR QUALITY

RESULTS OF ROTOR BEARING FRICTION

ENGINE SPEED = 7000.000 HORSEPOWER = 55.000

THE FRICTION FORCE IS 10.59 LBS.

RESULTS OF MAIN BEARING FRICTION

ENGINE SPEED = 7000.000 HORSEPOWER = 55.000

THE FRICTION FORCE IS 2.21 LBS

RESULTS OF TOTAL FRICTION ANALYSIS

THE HORSEPOWER LOST TO FRICTION = 1.914

****

ORIGINAL PAGE IS
OF POOR QUALITY

RESULTS OF [illegible] BEARING FRICTION

ENGINE SPEED = 1000.000 HORSEPOWER = 5.750

THE FRICTION [illegible] IS 1.52 LBS.

RESULTS OF [illegible] BEARING FRICTION

ENGINE SPEED = 1000.000 HORSEPOWER = 5.750

THE FRICTION [illegible] IS 0.56 LBS

RESULTS OF TOTAL FRICTION ANALYSIS

THE HORSEPOWER COST TO FRICTION = 0.038

****

ORIGINAL PAGE IS
OF POOR QUALITY

RESULTS OF MOTOR BEARING FRICTION

ENGINE SPEED = 3000.000 HORSEPOWER = 15.000

THE FRICTION FORCE IS 2.10 LBS.

RESULTS OF MAIN BEARING FRICTION

ENGINE SPEED = 3000.000 HORSEPOWER = 15.000

THE FRICTION FORCE IS 0.85 LBS

RESULTS OF TOTAL FRICTION ANALYSIS

THE HORSEPOWER LOST TO FRICTION = 0.124

****

ORIGINAL PAGE IS
OF POOR QUALITY

RESULTS OF ROTOR BEARING FRICTION

ENGINE SPEED = 9000.000 HORSEPOWER = 24.750

THE FRICTION FORCE IS 3.70 LBS.

RESULTS OF MAIN BEARING FRICTION

ENGINE SPEED = 9000.000 HORSEPOWER = 24.750

THE FRICTION FORCE IS 1.14 LBS

RESULTS OF TOTAL FRICTION ANALYSIS

THE HORSEPOWER LOST TO FRICTION = 0.391

****

ORIGINAL PAGE IS
OF POOR QUALITY

RESULTS OF MOTOR BEARING FRICTION

ENGINE SPEED = 6000.000 HORSEPOWER = 35.250

THE FRICTION FORCE IS 3.17 LBS.

RESULTS OF MAIN BEARING FRICTION

ENGINE SPEED = 6000.000 HORSEPOWER = 35.250

THE FRICTION FORCE IS 1.42 LBS

RESULTS OF TOTAL FRICTION ANALYSIS

THE HORSEPOWER LOST TO FRICTION = 0.552

****

ORIGINAL PAGE IS
OF POOR QUALITY

RESULTS OF ROTOR BEARING FRICTION

ENGINE SPEED = 5000.000 HORSEPOWER = 12.770

THE FRICTION FORCE IS 3.01 LBS.

RESULTS OF IDLER BEARING FRICTION

ENGINE SPEED = 5000.000 HORSEPOWER = 12.770

THE FRICTION FORCE IS 1.67 LBS

RESULTS OF TOTAL FRICTION ANALYSIS

THE HORSEPOWER LOST TO FRICTION = 0.896

****

ORIGINAL PAGE IS
OF POOR QUALITY

RESULTS OF [illegible] BEARING FRICTION

ENGINE SPEED = [illegible] HORSEPOWER = [illegible]

THE FRICTION [illegible] IS [illegible] LBS.

RESULTS OF [illegible] BEARING FRICTION

ENGINE SPEED = [illegible] HORSEPOWER = [illegible]

THE FRICTION FORCE IS [illegible] LBS

RESULTS OF [illegible] FRICTION ANALYSIS

THE HORSEPOWER LOST TO FRICTION = 1.342

**********[illegible]**********

ORIGINAL PAGE IS
OF POOR QUALITY

RESULTS OF ROTOR BEARING FRICTION

ENGINE SPEED = 7000.000 HORSEPOWER = 48.750

THE FRICTION FORCE IS 10.58 LBS.

RESULTS OF MAIN BEARING FRICTION

ENGINE SPEED = 7000.000 HORSEPOWER = 48.750

THE FRICTION FORCE IS 2.12 LBS

RESULTS OF TOTAL FRICTION ANALYSIS

THE HORSEPOWER LOST TO FRICTION = 1.903

****

ORIGINAL PAGE IS
OF POOR QUALITY

ANCILLARY COMPONENTS
OF AN
AIRCRAFT ROTARY ENGINE

DESIGN PROJECT

ME 422

JIM BEAGLE 0958108

MIKE CHMELKO 1015882

ROB LYNCH 1002770

Abstract

The purpose of this paper was to review ancillary components of a rotary engine in a small aircraft application.

The starting and generating system has demonstrated that benefits in weight, size and performance may be obtained through a total system approach. The types of information required and methods of analysis to design an optimal system is also described in this paper.

Air cooling versus liquid cooling of the engine was also investigated. Studies have shown that liquid cooling offers far more advantages and benefits.

Oil pump performance is discussed through a theoretical analysis. The investigator found that a trochoidal gear pump needs less driving force than that of the internal gear pump. Large rotor diameter, high pump rotation speed, and fluid friction were shown to have adverse effects on the pumping efficiency.

TABLE OF CONTENTS

	Page
NOMENCLATURE	2
INTRODUCTION	4
COOLING SYSTEM	
DISCUSSION	5
ANALYSIS	9
OIL PUMP	
ANALYSIS	18
DISCUSSION	30
FUEL PUMP	
ANALYSIS	32
CHARGING & STARTING SYSTEMS	33
BATTERY	37
ENGINE REQUIREMENTS	40
CONCLUSIONS	43
REFERENCES	45

NOMENCLATURE

b	=	face width, m
BHP	=	brake horsepower
BSFC	=	brake specific fuel consumption
e_o	=	no load voltage
E	=	terminal voltage at starter
E_{mp}	=	maximum terminal voltage
E_1, E_2	=	length of action of each gear
F_S	=	vertical load per unit profile, kg/m
F_B	=	vertical load applied to bearing, kg
GPM	=	gallons per minute
I	=	load current
I_{mp}	=	load current at which max. power occurs
I_{sc}	=	no voltage current
Lt	=	total driving force, kw
Lf	=	fluid friction loss, kw
L_M	=	mechanical friction loss due to rotor thrust, kw
L_S	=	intermeshing friction loss, kw
L_B	=	bearing unit friction loss, kw
n	=	rotation frequency of oil pump shaft, rpm
P	=	oil pump discharge pressure, kPa
P_M	=	thrust load applied to rotor, kPa

NOMENCLATURE (continued)

Qt	=	oil pump theoretical discharge rate (swept volume), m^3/sec
Qo	=	oil circulation flow rate, m^3/sec
Qb	=	oil relief flow rate, m^3/sec
Ql	=	oil leak flow rate, m^3/sec
r	=	radius of each rotor, m
R_e	=	effective internal resistance
RPM	=	revolutions per minute
s	=	difference between the maximum and minimum areas of tooth profiles, m^2
To_1, To_2	=	moment of fluid friction on inner and outer surface of rotor
Tc	=	moment of fluid friction working on outer rotor end surface
T_B	=	moment of friction at bearing unit, N.m
Z_1, Z_2	=	respective number of teeth of inner and outer rotors
ω_1, ω_2	=	angular velocities of inner and outer rotors, rad/sec
ζ	=	coefficient of fluid friction
μ_M	=	coefficient of friction at rotor towards thrust direction
μ_S, μ_B	=	coefficients of frictions at tooth profile and bearing
α	=	pressure angle of each gear

INTRODUCTION

For well over 40 years, general aviation aircraft have depended almost entirely upon the air cooled horizontally opposed piston engine as the primary means of propulsion. Although a dependable powerplant, this type of engine has seen little change over nearly half a century of usage. To meet the challenge of future general aviation requirements, a new liquid cooled aircraft rotary engine has been developed. This engine provides improved cooling, reduced cooling drag, lower fuel consumption, better wear characteristics, longer life and higher altitude capability. [8] — why not start with 1?

This paper will discuss the ancillary components and the effects these components have upon the aircraft rotary engine. Typical effects such as energy losses are shown for a typical automotive system (see Figure C-1). When designing an efficient engine system, one must minimize the energy losses attributed to the ancillaries to maximize performance. The following ancillary components will be considered during the design stages:

1. Electrical System (starter and alternator)
2. Cooling System (radiator and water pump)
3. Pumping Systems (oil pump and fuel pump).

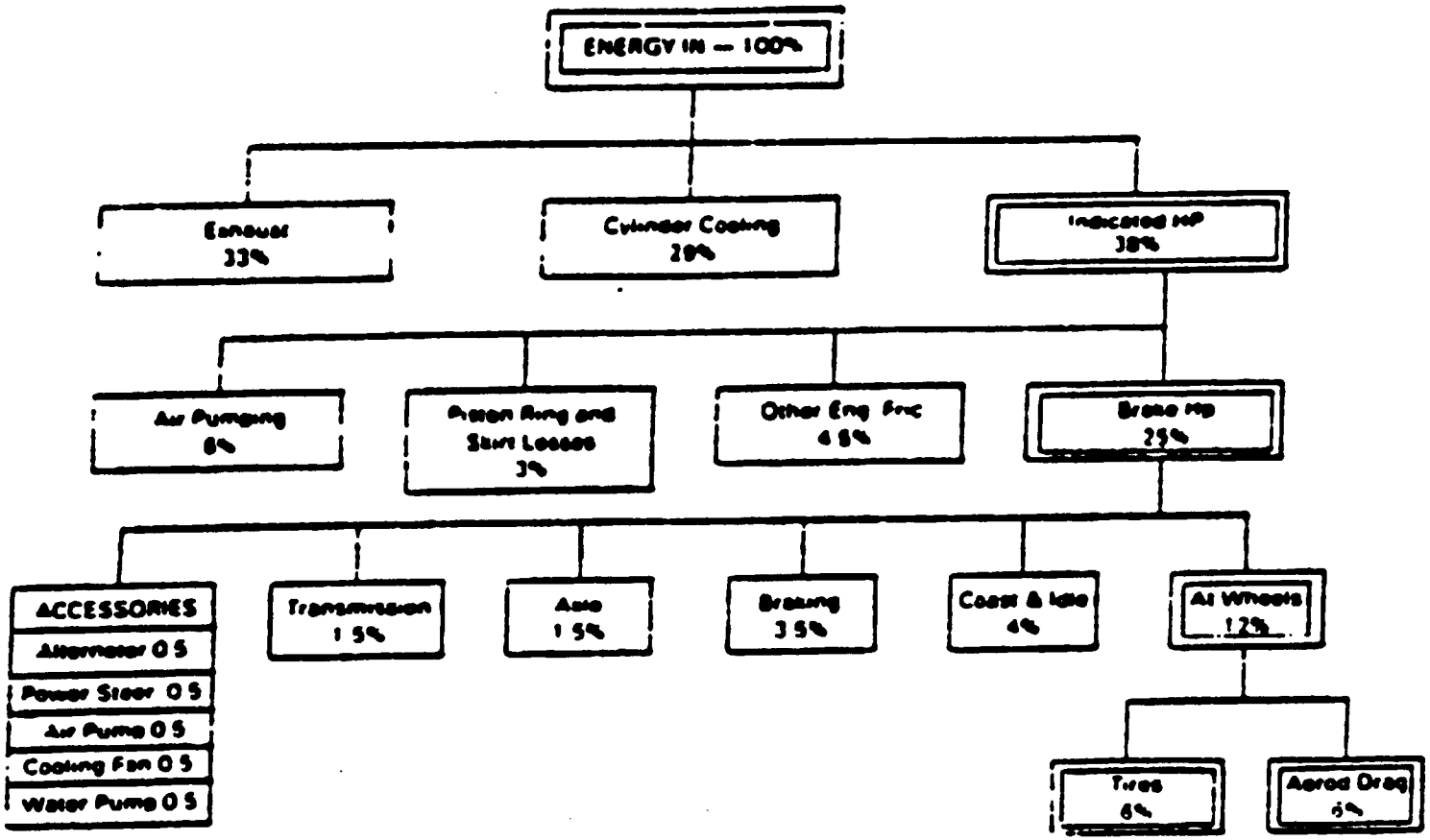

FIG. C-1 Energy distribution in passenger car during EPA Urban Schedule

ORIGINAL PAGE IS
OF POOR QUALITY

DISCUSSION

When designing a vehicle, one must consider the cooling system. This is obvious for several reasons: the vehicle must be able to operate in various atmospheric and service conditions without the temperature of the coolant rising too high or too low, either of which would have adverse effects on the engine.

In addition to this functional aspect, however, energy and ecological factors are also becoming more important with the passing of time. When refering to the power absorbed by the cooling system, one should keep in mind that the intake of outside air for cooling purposes has a negative effect on the energy balance of the vehicle.

Unfortunately, the optimum design of an engine cooling system is very difficult to achieve. The critical factor is the air circuit, because it is not possible to accurately predict its behaviour. The geometry of the system is often very complex as a result of different requirements such as size restrictions and cost factors. It is difficult to forecast the value of air flow parameters, such as system resistance, and aerodynamic efficiency of the air intake.

The Voyager engine development program has shown that it is possible to provide a liquid cooled engine with a dry weight equal to the dry weight of a comparable air cooled engine. A weight difference arises due only to the bulk coolant volume; specific weight of 60/40 ethylene glycol is 9 lbs/Gal at 60°F. However, this additional weight can be negated or minimized with reduced cooling drag. A well designed coolant to air heat exchanger, which is a more efficient heat transfer device than the finned multi-cylinder air cooled engine, requires substantially less cooling airflow. [8]

Liquid cooling was chosen because as the power output of an engine increases, air cooling becomes more difficult and the percentage of useful power that shows up as cooling power (or as parasitic drag) increases significantly. Efficient liquid cooling can result in roughly half the cooling loss of current air cooled reciprocating engines and also provide low metal temperatures in the highest heat zones. The liquid cooled engine can operate in an aircraft at the same specific fuel consumption figures that can be demonstrated on a test stand, whereas air cooled engines generally require a richer mixture to keep head temperatures to acceptable levels under cooling-limited power conditions. [10]

A significant factor that allows the liquid cooled engine to be a weight competitive option is the brazed aluminum plate/fin type heat exchangers. Liquid cooling alone does not provide improved fuel consumption; however, it does allow engine refinements previously not possible with air cooling.

A reduction in fuel consumption is made possible during takeoff and climb operation. Most air cooled engines are rated at a mixture strength richer than best power mixture in order to provide a fuel cooling effect during the low speed takeoff and climb. It is not uncommon to encounter a .700 BSFC on the larger air cooled turbocharged engines. The typical turbocharged air cooled engine would overheat at a best power fuel/air ratio during takeoff and climb. Liquid cooling allows the engine to be rated at best power mixture since the cylinder assembly is designed to cool adequately under these conditions with proper sizing of the liquid to air heat exchanger. [8]

The conventional air cooled engine is well known for its cooling anomalies. Many engines have a large temperature variance between individual cylinder heads. Non-uniform cooling airflow distribution within the engine compartment and the leakage associated with intercylinder and perimeter baffles are contributing factors. It is also difficult to achieve uniform cooling around the circumference of the head and barrel using the typical sheet metal baffles. Most automotive cooling systems utilize a series coolant flow circuit. Typical of these systems, coolant enters the block and flows first around the base of each cylinder before being directed to the cylinder head area. This approach tends to over cool the cooler bottom end and under cool the hotter head area with the cylinder heads increasing in temperature along the path as the coolant temperature rises. It is suggested that the rotary coolant be piped parallel to the drive shaft, this will enhance even temperatures.

Furthermore, the cylinder head metal temperatures may run hotter than when using a liquid cooled design. With more uniform temperature distributions, an engine will experience less distortion and better material strengths which result in lower wear rate and longer engine life. By designing an engine using liquid cooling, the engine manufacturer is able to effectively maintain control the engine temperature over its life span.

Significant reductions in cooling drag are also possible with the liquid cooled engine. Comparitive analysis indicates that a 30-50% reduction in cooling air massflow is possible for the higher output engines using a well designed and properly installed liquid to air heat exchanger. The lower cooling drag will yield higher aircraft flight

speeds or reduced fuel consumption for fixed flight speeds. For example, a 50% reduction in cooling airflow equates to a 2-3% increase in forward speed or optionally a 7-10% decrease in BSFC and BHP required, assuming cooling drag at 15-20% of total aircraft drag. With the more uniform cylinder cooling, cooler combustion chamber temperatures, absence of cooling anomalies, and better wear characteristics, significant improvements in engine durability are now attainable. These improvements result in a more reliable, highly efficient engine with longer engine life and reduced operating/maintenance costs. In addition, performance and operational advantages such as reduced fuel consumption, increased power output, and reduced cooling drag contribute to provide an advanced aircraft engine concept capable of meeting the challenges of future general aviation requirements. [8]

ANALYSIS

Internal combustion engine heat rejection characteristics are best evaluated on the basis of three qualitative parameters defined as follows:[9]

1. Percent of available fuel energy lost to cooling.
2. Heat lost to coolant and oil as a percentage of engine BHP output.
3. Specific heat loss defined as ratio of cooling heat load to engine BHP (BTU/Min/BHP).

Naturally aspirated liquid cooled automotive gasoline typically reject 20-25% of available fuel energy to cooling. The best high performance automotive engines dissipate as little as 16% at maximum power. Typical specific heat rejection values for automobile engines vary from 30-40 BTU/Min/BHP depending upon output. [8]

With the preceding background discussion in automotive rotary engines and liquid cooled aircraft engines, we are now able to make predictions concerning the aircraft rotary engine. We will examine an aircraft (eg. Cessna, Fig. C-1) powered by an RC2-60 rotary engine. This spark ignited carbureted gasoline engine is rated at 185 hp with a moderate sized two-barrel carbureter; is 18 inches long; and weighs 237 lb. A photograph of the engine is shown in Fig. C-2, and representative full throttle performance data are given in Fig. C-3. [10]

Fig. C-1 Cessna Cardinal airplane with RC2-60 engine double prop speed reduction

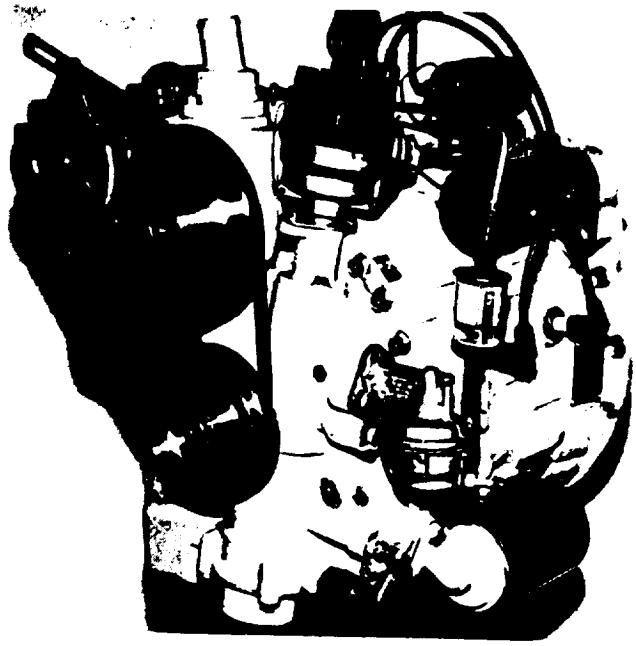

Fig. C-2 RC2-60 engine

ORIGINAL PAGE IS
OF POOR QUALITY

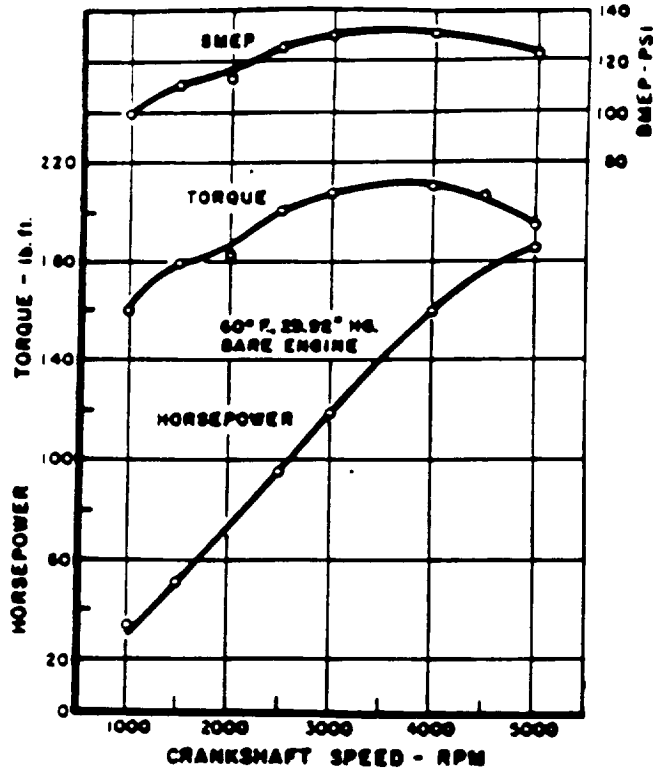

Fig. C-3 Initial test results RC2-60

Assuming a crankshaft speed of 4000 RPM, we have an engine power output of 160 HP. If 25% of this power is lost to cooling, then 40 HP or 30.4 kW of power must be dissipated. The Fig. C-4 shows that the water temperature is a balance between the dissipative power and the power to be dissipated.

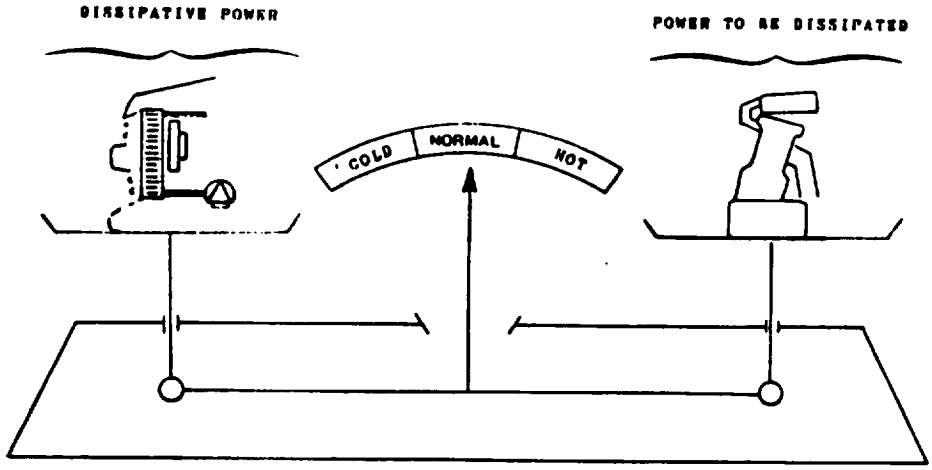

Fig. C-4 The water temperature is a balance between the dissipative power and the power to be dissipated

ORIGINAL PAGE IS
OF POOR QUALITY

The "Power that to be Dissipated" is the power supplied to the water by the engine which depends on the engine load and rpm. The Fig. C-5 shows the results of measurements taken on an engine equipped with a calorimeter. With the RC2-60 operating at 4000 RPM, approximately 30 kW are supplied to the water.

POWER SUPPLIED TO THE WATER in kW

Power on Engine Crankshaft kW \ Engine Speed in rpm		2000	2500	3000	3500	4000	4500	Max. Engine Speed 4000			
5,34		5,90	8,15	10,36	13,12	15,70	20,88	24,36			
10,67		8,89	10,42	12,22	15,09	18,04	22,33	25,70			
16,01		13,26	13,45	15,36	18,07	20,33	25,16	28,52			
21,36		-	17,61	19,16	20,68	23,52	27,80	32,04			
26,68		-	-	24,01	24,98	28,06	31,51	36,46			
32,02		-	-	-	29,96	31,96	35,76	40,06			
37,36		-	-	-	-	39,37	41,94	46,09			
FULL LOAD	Water P in kW	19,30	25,25	30,47	34,75	39,37	44,60	48,71			
	Engine P in kW	19,80	25,03	30,08	34,30	38,05	38,51	39,46			

Fig. C 5 Example of measurements of the power to be dissipated

ORIGINAL PAGE IS
OF POOR QUALITY

The "Dissipative Power" is the power dissipated by the radiator in driving conditions which varies with radiator operation. The radiator is not an isolated component and its operation directly depends on the water and air systems. With the above assumed value of 30 kW for the dissipative power, we now must assume a pressure drop for the airplane at the corresponding air speed. A minimum pressure drop of 45 PSIA (310 Pa) is required to prevent boiling and cavitation. Therefore, with Fig. C-6 as a reference, a water flow rate of 1800 l/h is required.

POWER DISRIPATRB (kW) at ΔT_i=70°C

Air flow rate / Water flow rate	40	70	100	200	300	400	700
900	11.7	16.2	18.7	23.0	25.2	26.6	29.0
1 800	12.3	10.0	21.2	27.2	30.5	32.9	37.0
3 600	13.0	19.6	23.4	31.0	35.0	38.0	44.0
4 800	14.0	21.0	25.5	35.1	41.0	45.5	54.2
7 200	14.6	21.5	26.5	37.5	44.8	50.2	62.0
8400	14.8	22.2	27.3	39.0	46.0	52.0	64.5

Fig. C-6 Experiment results of the radiator

ORIGINAL PAGE IS
OF POOR QUALITY

The water pump characteristics and hydraulic load losses of the water system components have to be taken into account. This results in a water pressure/water flow curve representing a dummy water pump located ay the edges of the radiator. The water flow in the radiator will result from the way the dummy water pump and the radiator are matched. The Fig. C-7 shows the chacteristics pressure/flow rate.

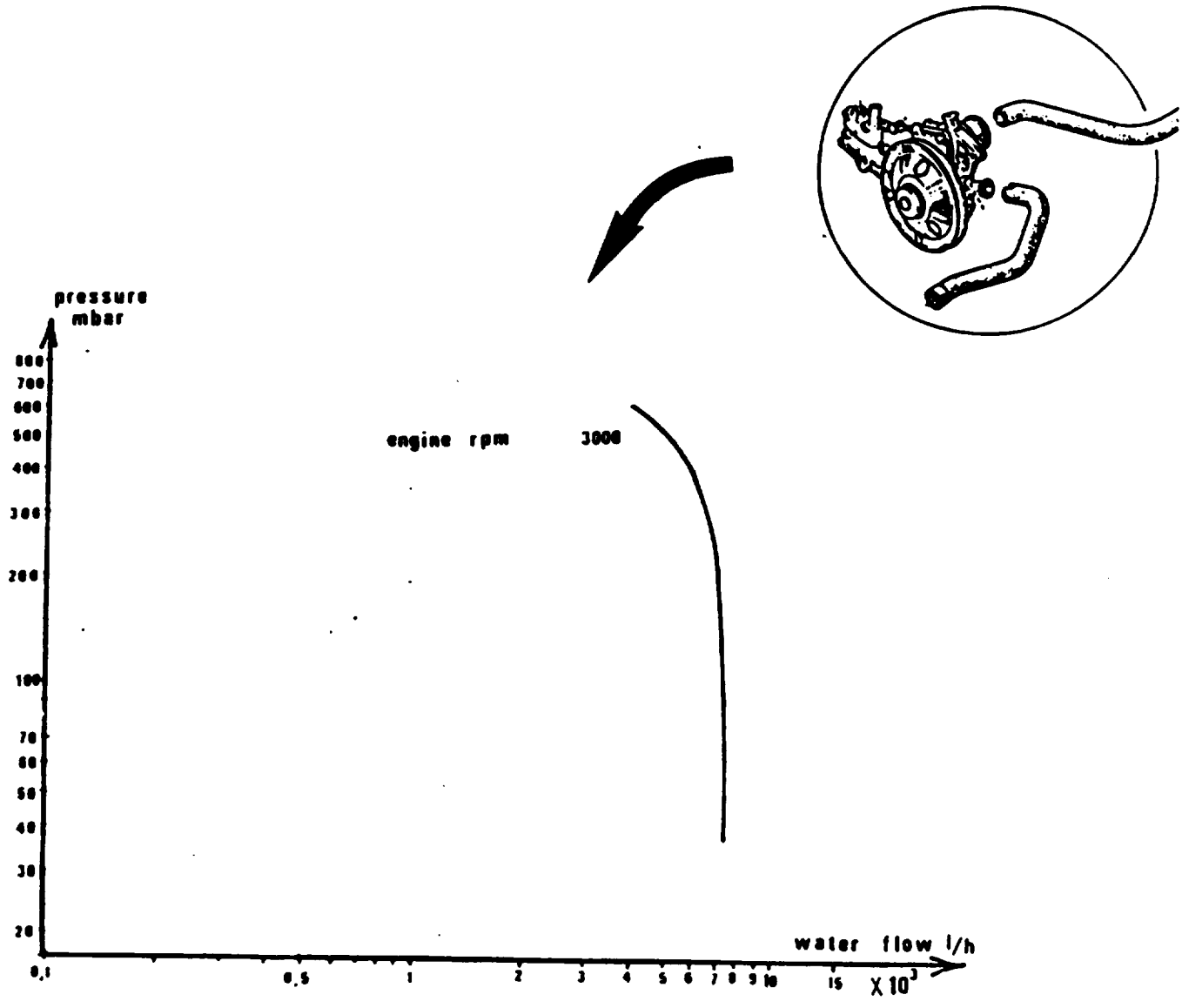

Fig. C-7 Characteristics pressure/flow rate

ORIGINAL PAGE IS
OF POOR QUALITY

A comparable aircraft engine is the Voyager 300 (IOL-300). This liquid cooled six cylinder 300 cubic inch engine is capable of being rated at 170-190 BHP at 2700-3000 RPM. Figure C-8 presents heat rejection rates for the IOL-300 engine at best power mixture in terms of specific heat loss and percent of available fuel energy lost to cooling as a function of BHP and engine speed.

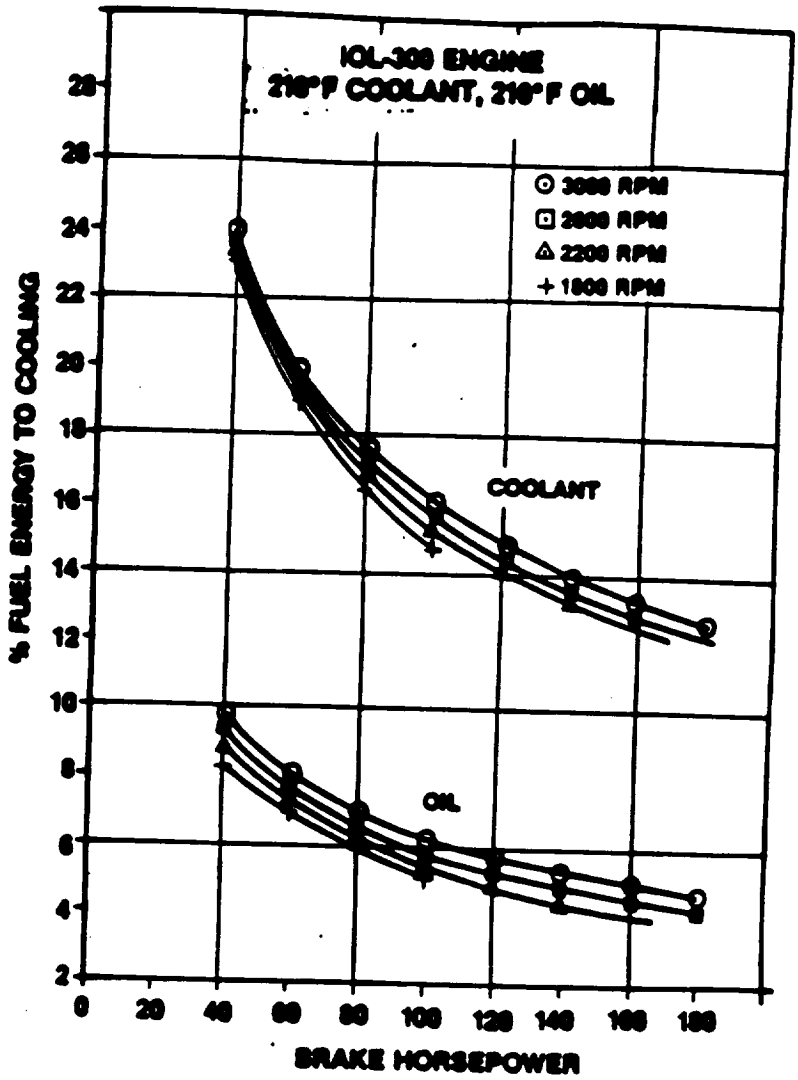

Fig. C-8 IOL300 Percent Energy to Cooling

The maximum operating coolant temperature into the engine is 250'F with a 20'F rise across the engine at maximum power. By designing for a high coolant temperature rise, the coolant flowrate is reduced which minimizes pump power and size. The high coolant bulk temperature serves to lower heat rejection which helps minimize heat exchanger size and weight. Coolant flowrate for the (IOL-300) at maximum power is 20 GPM with the 20'F rise.

The effect of higher coolant temperature is clearly apparent. A 40'F increase from 250'F to 290'F offers a potential 10% reduction in heat loss which would reduce the size of the coolant to air heat exchanger. Although the engine thermal loading and heat loss characteristics were evaluated with 290'F coolant, the maximum allowable inlet temperature to the engine is restricted to 250'F. This decision was made in consideration of the lack of test experience at the elevated temperature and the potential problems associated with the higher pressures (45 PSIA minimum) required to prevent boiling and cavitation.[8]

The RC2-60 rotary engine and the IOL-300 piston engine may be compared in relative terms. Both engines have comparable power outputs, and therefore comparable power is needed for dissipation. One would assume the cooling systems would be interchangable. Once again refering to Fig. C-8, we notice that at 180 BHP the IOL-300 has only 13% of the fuel energy lost to cooling. For the rotary RC2-60, we assumed a 25% energy loss to cooling. This difference originates from the engines themselves; the IOL-300 generates 180 BHP at 3000 RPM, while the RC2-60 requires a crankshaft speed of 5000 RPM to reach comparable horsepower output. Therefore, as expected, the energy losses are greater at higher engine speeds.

ANALYSIS ON DRIVING FORCES OF OIL PUMPS

A number of efforts to reduce friction losses in automobile, aircraft, and other engines have been made in order to save energy in recent years. Researchers have been and will continue to do extensive research on all components of an engine which require power to operate and therefore incur losses due to the lack of 100 % efficiency. As a part of such efforts, investigation and analysis have been done on oil pump driving forces. One such analysis was performed in 1986 and documented in SAE Paper number 860230 entitled "Analysis on Driving Forces of Oil Pumps for Internal Combustion Engines". The following analysis is an excerpt from the paper and is presented as follows:

Oil pump driving forces can themselves be broken down into a variety of sub-categories as seen in Figure P1. They consist of the following:

1) Mechanical friction loss
2) Work lost as a result of oil leakage
3) Fluid friction loss
4) Work to compress the oil

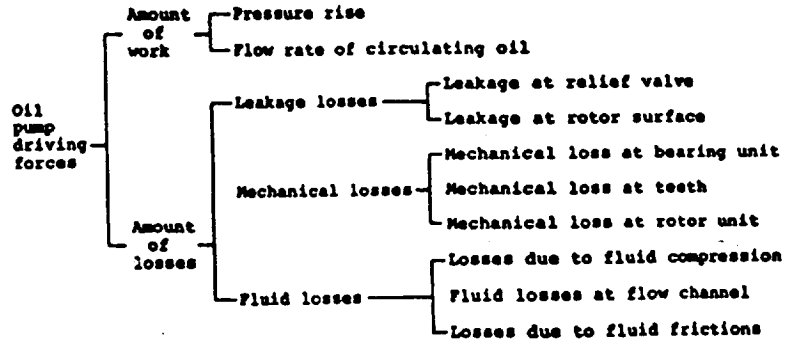

Composition of Oil Pump Drving Forces

FIGURE P1

ANALYSIS (continued)

Oil pumps used in the analysis and used in the experiment were internal gear type and trochoidal gear type pumps, both of which are commonly used in today's aircraft and automobiles. See Figure P2 .

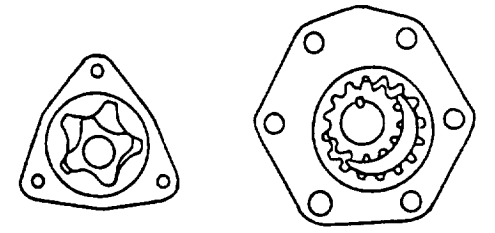

(a) trochoidal gear type (b) Internal gear type

FIGURE P2

OIL PUMP DRIVING FORCES:

The total driving force of such an oil pump consists of the following components:

$$Lt = PQt + Lf + L_M + L_S + L_B \qquad (1)$$

where **Lt** is the total driving force, **P** is the oil pump discharge pressure, **Qt** is the oil pump theoretical discharge rate, **Lf** is the fluid friction loss, L_M is the mechanical friction loss due to rotor thrust, L_S is the intermeshing friction loss, and L_B is the bearing unit friction loss.

ANALYSIS (continued)

The theoretical discharge rate may be expressed as follows:

$$Qt = S\,b\,Z_1\,n/60 \qquad (2)$$

where **S** is the difference between the maximum and minimum area of tooth profiles, **b** is the face width, Z_1 is the number of teeth on the inner rotor, and **n** is the rotation frequency of the oil pump shaft.

OIL PUMP WORK AND LEAKAGE LOSS:

The quantities **Qo, Qb,** and **Ql** make up the total oil pump flow rate, as shown in Figure P3. The theoretical discharge rate is expressed by the sum of these components as given below:

$$Qt = Qo + Qb + Ql \qquad (3)$$

where **Qo** is the oil circulation flow rate, **Qb** is the oil relief flow rate, and **Ql** is the oil leak flow rate.

The theoretical amount of oil pump work is, therefore, expressed as follows:

$$P\,Qt = P\,(Qo + Qb + Ql)$$
$$= P\,S\,b\,Z_1\,n/60 \qquad (4)$$

ANALYSIS (continued)

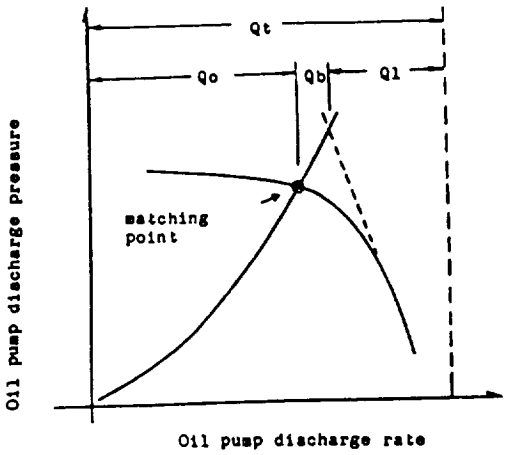

Oil pump discharge specification

FIGURE P3

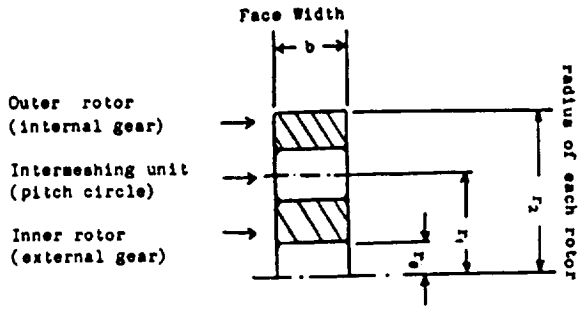

Oil pump assumed in the geometry of a disc.

FIGURE P4

FLUID FRICTION LOSS:

Assuming that the geometry of the oil pump is of disc shape as shown in Figure P4, the following equation may be written:

$$Lf = 2 (To_1 \omega_1 + To_2 \omega_2) + Tc \omega_2 \qquad (5)$$

where To_1 and To_2 are the moments of fluid friction working on the inner and outer rotor side surfaces, ω_1 and ω_2 are the angular velocities of the inner and outer rotors, and **Tc** is the moment of fluid friction working on outer rotor end surface.

ANALYSIS (continued)

Assuming now that the fluid friction force on the rotor surface is τf:

$$\tau f = \zeta \psi r^2 \omega^2 / 2 \qquad (6)$$

where ζ is the coefficient of fluid friction and r is the radius of each rotor.

Thus, it can be determined through further calculation,

$$To_1 = 2\pi r \tau f r \, dr$$

$$To_1 = 1/5 \, \pi \psi \zeta \omega_1^2 (r_1^5 - r_0^5) \qquad (7)$$

$$To_2 = 2\pi r \tau f r \, dr$$

$$To_2 = 1/5 \, \pi \psi \zeta \omega_2^2 (r_2^5 - r_1^5) \qquad (8)$$

$$Tc = 2\pi r_2 \tau f (r=r2) \, b \, r^2$$

$$Tc = \pi \psi \zeta \omega_2^2 r_2^4 \, b \qquad (9)$$

And therefore,

$$\omega_2 = \omega_1 \, Z_1 / Z_2$$

$$\omega = \pi n / 30 \qquad (10)$$

Namely, the total fluid friction loss is given by the following:

$$Lf = \pi \psi \zeta \omega_1^3 (.4 \, (Z_1/Z_2)^3 (r_2^5 - r_1^5) + .4(r_1^5 - r_0^5) + (Z_1/Z_2)^3 r_2^4 \, b) \qquad (11)$$

MECHANICAL FRICTION LOSS CAUSED BY ROTOR THRUST:

The mechanical friction loss due to rotor thrust (L_M) is given as/

$$L_M = (T_{M1}\,\omega_1 + T_{M2}\,\omega_2) \qquad (12)$$

Where, $T_{M1} = \mu_M\, r\, P_M\, 2\pi\, r\, dr$

$$= 2/3\,\pi\,\mu_M\, P_M\, (r_1^3 - r_0^3) \qquad (13)$$

$$T_{M2} = \mu_M\, r\, P_M\, 2\pi\, r\, dr$$

$$= 2/3\,\pi\,\mu_M\, P_M\, (r_2^3 - r_1^3) \qquad (14)$$

Now we can assume that P_M is proportional to the pump discharge pressure **P**, such that $P_M = B\,P$. Therefore, we have the following:

$$Lf = 2/3\,\pi\,\mu_M\, B\, P\, \omega_1 ((r_1^3 - r_0^3) + (Z_1/Z_2)(r_2^3 - r_1^3)) \qquad (15)$$

CALCULATION OF MESHING AND BEARING FRICTION LOSS:

The meshing friction loss for the internal gear is/

$$L_S = \mu_S\, \omega_1\, Z_1\, (1/r_1 - 1/r_2)\, (E_1^2 + E_2^2)\, F_S\, b / \cos\alpha \qquad (16)$$

The bearing friction loss for the internal gear is derived from the following:

$$L_B = \omega_1 T_B$$

$$T_B = \mu_B F_B r_o \ ,$$

Thus, $$L_B = \omega_1 r_o F_B \mu_B \qquad (17)$$

CALCULATION OF TOTAL DRIVING FORCE, Lt:

Putting together all of the above equations and calculating, a very complicated expression can be derived for the total driving force, **Lt**.

$$Lt = (n/60)\,(SbZ_1P + 3/4\,\pi^2\,B\,P\,\mu_M\,((r_1^3 - r_0^3) + (Z_1/Z_2)\,(r_2^3 - r_1^3)) + 2\pi\,(\mu_S\,F_S\,Z_1\,b/\cos\alpha(E_1^2 + E_2^2)(1/r_1 - 1/r_2) + \mu_B\,F_B\,r_o)) + 8\,\pi^4\,\psi\zeta\,(n/60)^3\,(2/5\,(Z_1/Z_2)(r_2^5 - r_1^5) + 2/5\,(r_1^5 - r_0^5) + (Z_1/Z_2)^3\,r_2^4\,b) \ , \qquad (18)$$

The above equations give a very accurate theoretical analysis of the friction, bearing, meshing losses, and total driving forces required to power an oil pump used in automobile and aircraft applications. To test the accuracy of the equations, various tests were performed on four different oil pumps. The characteristics of each pump are provided in Table T1 . A series of 4 tests were done, measurements were taken, and then all data was compared to the theoretical values obtained using Eq. 18.

ORIGINAL PAGE IS
OF POOR QUALITY

Table T1

Test No.		1	2	3	4
Type of pump		Internal gear		Trochoidal gear	
Face width		0.6 cm	1.0	1.4	0.9
Area between teeth		0.151 cm^2	0.260	1.025	1.025
No.of teeth	Inner z	23	23	4	4
	Outer z	27	28	5	5
Radius	Inner r	2.8 cm	3.0	1.3	1.3
	Outer r	3.5	3.7	2.0	2.0
	Bearing r	1.7	1.7	0.63	0.63

TABLE T1 needs a title

TEST RESULTS:

A summary of results using test pump number 1 is given in Figure P5. In Figure P5, the curve of (1) represents the total driving force, where both the outer and inner rotors were pushed completely against one side - that is, B = 1.0, the curve of (2) shows the test results for nearly the same condition. In performing the experiment, oil grooves were provided at both sides of the outer and inner rotors, so that the value of B would become smaller. As a result of this, the value of B was later determined to be .5. The curve of (3) represents the amount of work determined by the test results of oil pump discharge pressure and rate, while the curve of (4) represents the driving work, where the discharge pressure is determined by the measured value, and the discharge rate is determined by the sweep flow rate (**Qt**). The curve of (5) represents the meshing friction loss. As is determined from the graph, the driving work requires the most force and the meshing friction losses are the least significant.

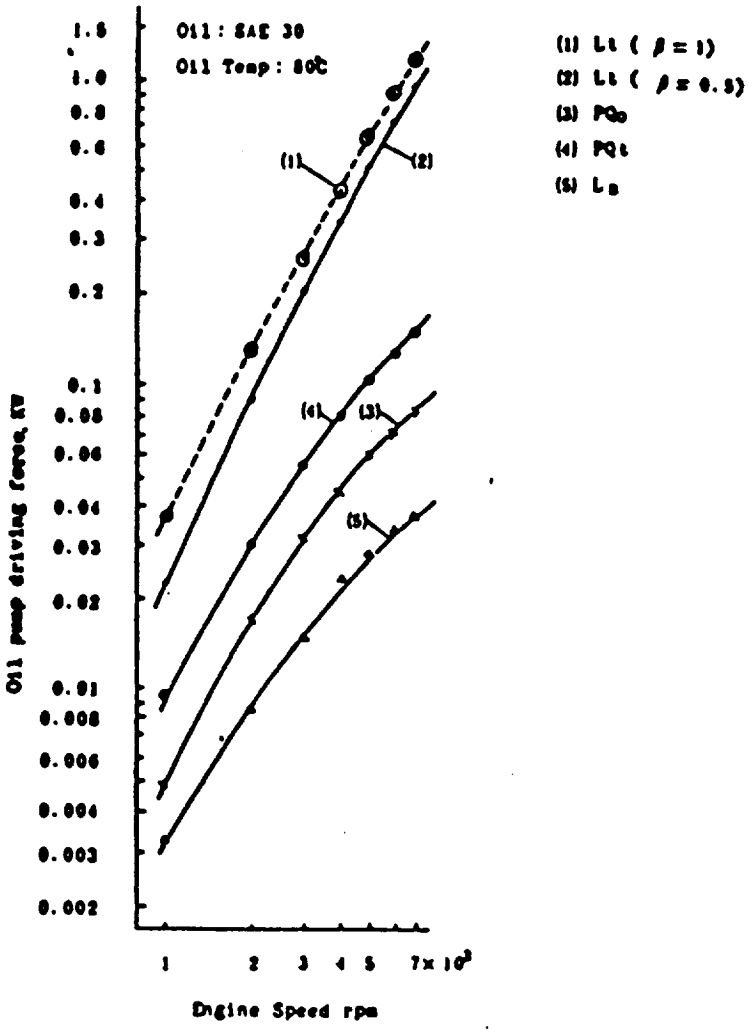

Test results for each driving force - No.1 pump

FIGURE P5

ANALYSIS (continued)

In analyzing the results of the experiment and making final determinations, the bearing friction loss is ignored since it was found to be 1% or less of the total driving force. From the previously listed results and findings, **Lf**, L_M and L_S may be determined by calculation. Figure P6 shows the results of the calculation.

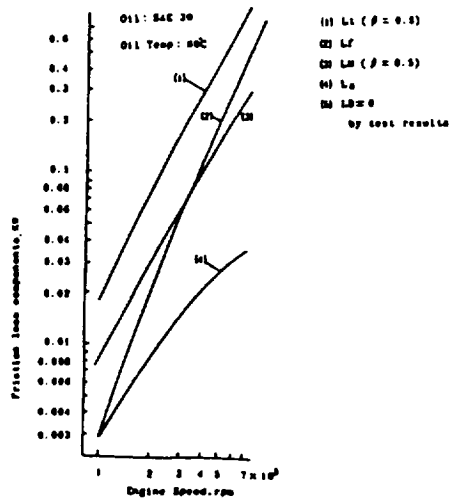

Friction Losses from No.1 pump specification

FIGURE P6

ANALYSIS ON FLUID FRICTION LOSS:

To determine the fluid friction loss for the oil pump, the following equations are obtained by substituting corresponding values into Eq. (11).

$$Lf = 0.100\,(n/10^3)^3\,\zeta \qquad (19)$$

From Figure P6, we can determine:

$$Lf = 0.0055\,(n/10^3)^{2.5} \quad (20)$$

And according to Eq. (19) and (20):

$$\zeta = 0.055\,(n/10^3)^{-0.5} \quad (21)$$

The coefficient of fluid friction obtained by Eq. (21) is appropriate assuming that it is the flow passing through the clearance between the rotor and the casing and housing. This assumption must be made to assure adequate values. In order to account for turbulent effects of the oil flowing through different parts of the oil pump, extremely complicated analysis would be required.

Next, a value of the thrust mechanical friction loss is obtained. By substituting related values into Equation (15) and taking the required values off of the Figure P6, a new equation for the coefficient of friction μ_M is developed:

$$\mu_M = 0.011\,(n/10^3)^{0.46} \quad (22)$$

μ_M has the characteristic to increase generally in proportion to the increase of $n^{0.5}$ at the Hydrodynamic Region seen on any Stribeck diagram. Therefore the result of calculation by Eq. (12) is appropriate.

RESULTS AND DISCUSSION OF OIL PUMP ANALYSIS

Figure P7 shows the comparison between measured values obtained by Tests No. 1 through No. 4, and theoretical values calculated by substituting corresponding values of specified dimensions given in Table II and calculated using the various equations derived in the given analysis. Obviously, the comparison reveals that the theoretical and experimental results agree very well with each other. Thus, through the given procedure, a fairly accurate determination can be made as to the losses incurred in a given pump design. Given this knowledge, engineers will be able to design and develop more inexpensive and efficient oil pumps to enable the rotary engines of future aircraft to be much more effective.

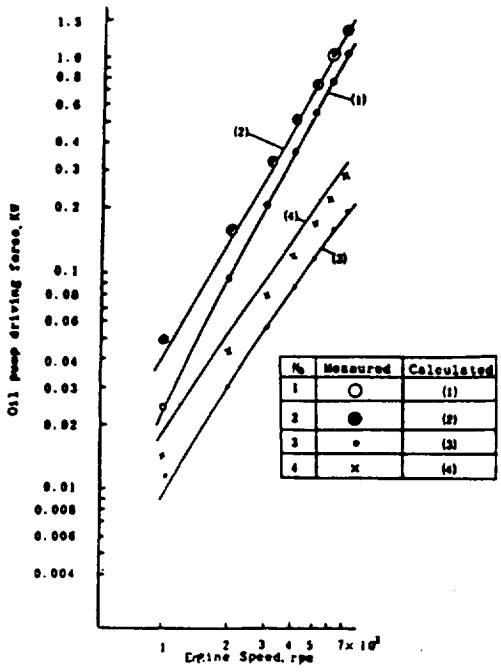

Comparison of each oil pump driving force between Measured & Calculated Values

FIGURE P7

RESULTS AND DISCUSSION (continued)

From the preceding analysis the following may be said concerning the performance of the oil pump:

----- It was found from the study that the pumping efficiency may be improved for a given flow rate if the rotor width is increased while the rotor radius and the rotation speed are reduced.

----- The effect of the rotor diameter on the pumping efficiency is great, which is indicated by the relationship of r^5 for the fluid friction loss, and r^3 for the thrust friction loss.

----- The effect of the pump rotation speed (engine speed) is $n^{2.5}$ for the fluid friction loss, $n^{1.86}$ for the thrust friction loss, and nearly linear with with speed for the other variables.

----- Since effect of oil viscosity is included in the coefficient of fluid friction, etc., variations in oil temperature and properties are evidenced as variations of respective coefficients of individual friction losses.

----- The total driving force of the internal gear pump is greater than that of the trochoidal gear pump. The fluid friction loss accounts for the highest rate, followed by the thrust friction loss. This is due to the large rotor diameter with the thin gear width.

A BRIEF FUEL PUMP ANALYSIS

In the past, most automotive electronic fuel pumps were controlled to turn on or off due to a mechanical relay. At least for this document, the same method is assumed to have been used for aircraft applications. Nevertheless, to keep up with the increasing power of engines, the output capacity of fuel pumps had to be increased. This resulted in higher electric power consumption and louder operating noise. To solve these problems over the years, Nissan Motor Company has developed a fuel pump driving voltage control system. The controlled average voltage to the fuel pump is determined by the control module according to the fuel consumption, the required amount of return fuel, and the temperature of the fuel supply units. The computer in the control module calculates the control duty ratio from engine revolution speed and the load condition from the crank-angle sensor and air flow sensor signals, along with other variables in the engine. The controlled voltage of the fuel pump changes basically in accordance with engine revolution speed (N) and injection pulse width TI, and is proportional to the engine load as shown in Figure P8. The fuel pump driving voltage control saves 40% of the electric power and reduces the noise from pump rotation by 5dB-A.

It must be noted, however, that this control system does not directly apply to our application of a rotary engine used on a small aircraft. However, with only a few modifications to the described system, a new control system could be easily developed to maximize the fuel pump efficiency of an electronic fuel pump used on a rotary engine in a small aircraft.

Components of Charging and Starting Systems

The electrical system of light aircrafts has developed from a magneto or a pair of magnetos. Today it is not uncommon for electrical and electronics equipment to cost up to half as much as the basic cost of the airplane. The devices that supply electric energy to this are costly and highly important are therefore equally important to the airplane. In light commercial airplanes, the primary electric energy source is the engine d-c generator , or more recently the self-rectifying alternator. The lead-acid storage battery can no longer be considered a source of abundant electric energy. (1)

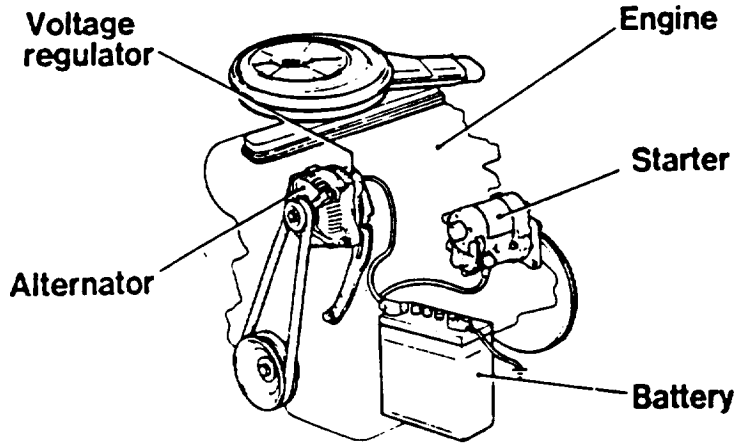

Components of charging and starting systems

Components of Charging and Starting Systems

The charging and starting systems are made up of an alternator, starter, battery and related components, and are all mounted around the external part of the engine.

The charging system is centered around the engine, and is composed of the alternator, voltage regulator (to be referred hereinafter as the "regulator"), and the battery.

To begin with the components of the charging system, the alternator is driven by the engine through the use of a belt, and it's rotational energy is converted to electrical energy. The electrical power that is generated in this manner is supplied to electrical load components such as the ignition system, lighting, air conditioner clutches, and is also used to charge the battery.

The regulator regulates the voltage generated by the alternator in such a way that the voltage applied to electrical load and the battery will remain at their optimal levels.

To move the starting system, the starter is connected to the battery by electrical wiring and receives a large supply of current from the battery in a short period of time, then converts this current to a rotational torque. This rotational torque is converted into a large amount of initial breakaway torque and transmitted to the engine by the starter

ORIGINAL PAGE IS
OF POOR QUALITY

pinion and the engine ring gear (flywheel), where it generates the rotations necessary to start the engine.

Performance Requirements of the Charging Components

Ideally, alternator output should be higher than the electrical load throughout the entire range of engine speeds. To accomplish this, it is necessary to give the alternator an extremely large capacity, and to increase load applied to the engine as well.

Generally speaking, the approach has been to select an alternator capacity that will allow a balance output and load at a given engine speed. At speeds below this balance point the insufficiency in alternator output is made up for by contributions from the battery to loads. At speeds above the balance point, the alternator contributes current to the load as well as providing charge to the battery. Selection of the speed at which this balance is to be obtained is largely dependent on the type of power requirements of the particular system.

The electrical load of the airplane, however, increases each year, due to the factors such as improvement of "fly-ability", the increasing of comfort and new conveniences of the airplane. In addition, their has been an increase in the demand for alternators which are both smaller and lighter in weight, and it has been necessary to devise ways by which both of these conflicting demands could be met.

ORIGINAL PAGE IS
OF POOR QUALITY

Performance Requirements of the Starting System

Engine cranking torque is generated from friction resistance in the engine sliding parts, oil viscosity, compression pressure and other factors. At low temperatures, it is increased by increases in oil viscosity. On the one hand, engine cranking speed is determined by the balance achieved between engine cranking torque and the torque that is obtained from the combination of starter and battery. For this reason, the major performance requirement of the starting system components is the obtaining of a cranking speed at low temperatures sufficient to fire the engine. The engine speed requirement at this time is influenced by the factors such as engine ignition performance, properly adjusted fuel intake, i.e., a well tuned engine.

These factors mean that the improvement of system performance balance is a basic requirement for starting system components, and that reduction in size and weight is tied to improving the performance of the starter and improving the discharge characteristics of the battery.

The purpose of the following section is to analyze the performance characteristics of batteries along with those of starters and alternators.

Batteries

ORIGINAL PAGE IS
OF POOR QUALITY

Most aircraft using electrical engine starting systems utilize on-board nickel-cadmium batteries as a power source in order to avoid dependence upon ground service and thereby increase the aircraft's usage to it's operator. This is particularly significant to the owners of aircrafts who find it necessary to operate away from an airport where ground-support facilities do not exist.

The charging performance of the battery fluctuates greatly depending on factors such as battery temperature and charging voltage. In particular, one of the most important pre-requisites for the use of a small capacity battery was the charge acceptance characteristic at low temperatures. Improvement of the charge characteristics of the system so that there is adequate charging output, even under low temperature conditions, is a basic important problem in the development process.

At temperatures below 32 F, battery electrolyte becomes more viscous and internal cell resistance begins to increase significantly. The use of larger batteries will help out in cold weather battery-starting conditions; however, there exists a point at which the battery weight necessary to provide this additional support is out of proportion to the desirability of the service it offers. In addition, the additional associated weight and size of a larger battery are major design considerations.

FIG. E1 SOURCE E VS. I CHARACTERISTICS

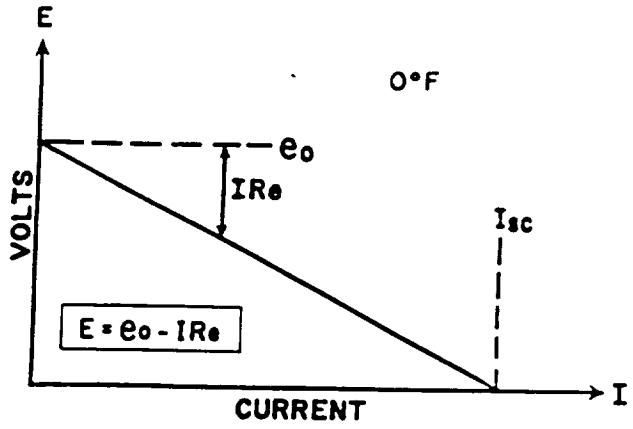

FIG. E2 SOURCE POWER VS E OR I

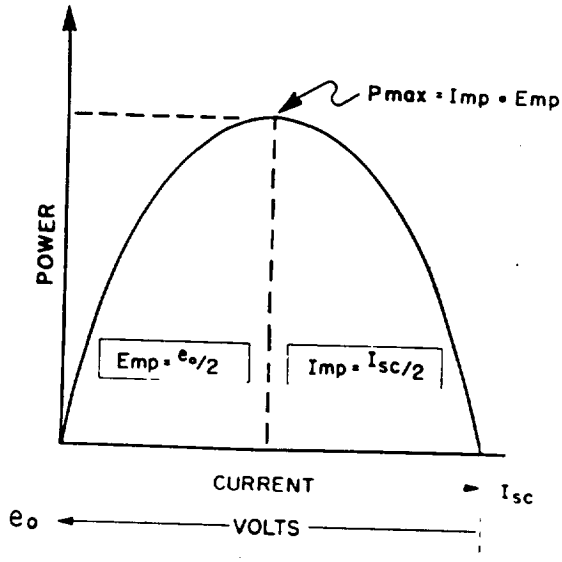

e_o - NO LOAD VOLTAGE
I_{sc} - NO VOLTAGE CURRENT
R_e - EFFECTIVE INTERNAL RESISTANCE
E - TERMINAL VOLTAGE AT THE STARTER
I - LOAD CURRENT
E_{mp} - MAX TERMINAL VOLTAGE
I_{mp} - LOAD CURRENT (MAX POWER TRANSPER)

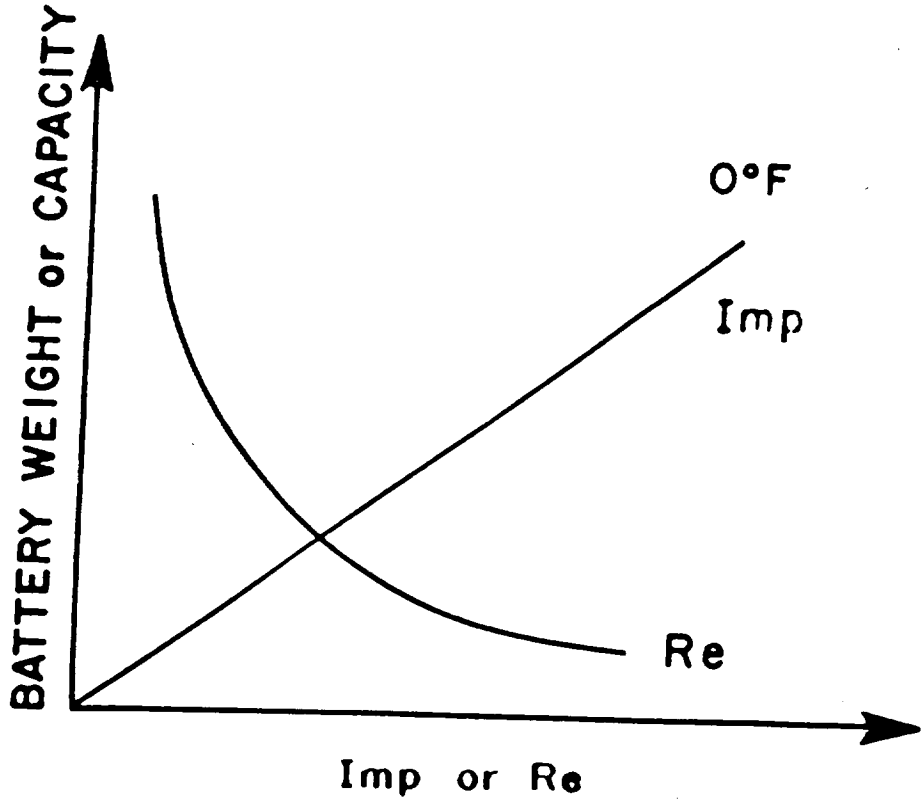

FIG. E3 BATTERY PARAMETRIC RELATIONSHIPS

ORIGINAL PAGE IS
OF POOR QUALITY

It has been a general aircraft industry standard to design for 0 F engine start capability with batteries. In this manner, the extent of its capabilities has usually offset the weight/cost factors required to provide it. This, of course, depends upon the degree of starting difficulty presented by the engine in question. When engines are difficult to start, there is a tendency to seek a compromise with this criteria by raising the minimum temperature acceptable for battery starts in order to avoid large weight penalties for the airplane. This has resulted in marginally acceptable starting systems, which have been an irritation to pilots and have resulted in either engine stress and/or severely shortened battery life because of the large depth of charge/discharge and thus the associated thermal stress from lengthy and repeated start-up attempts.

At the other end of the spectrum is the aircraft design approach, which results in the use of much higher capacity batteries than are really needed to satisfy emergency power demands, in order to achieve the starting performance desired.

The solution lies somewhere between these two extremes so that Re (effective internal resistance) will be at the optimum level while providing acceptable starting performance and maintaining a sufficient capacity for emergency power. In order to do this at the lightest battery weight possible, it is necessary that battery Pmax (maximum power delivered to the starter) be transferred to the engine during the start

cycle when the engine start-power demand is the greatest.

Generally speaking, nickel-cadmium batteries posses the characteristics described in Figs. 11 and 12. At any particular temperature of interest, the relationship between weight, Re, Imp (load current at which maximum power transfer occurs), and battery capacity can be represented as in figure 13. It is assumed here that the voltage rating (that is the number of cells) and temperature is held constant. In a 19-cell battery, e(o)-(no load voltage), is 23.5 V (d-c) at room temperature; however this drops off as electrolyte temperature is reduced and is typically 22.5 V (d-c) at 0 F. (3)

Engine Requirements

The well known method for describing engine starting power requirements is called the "drag-torque curve." This is a plot of the drag and assist torque versus speed seen by the engine at its starter accesory-pad during the start cycle. A typical example of such a curve is shown in Fig. .

The torque peak value and the curve vary with temperature and engine design. It is important to know both the specific drag-torque characteristics of the engine at the temperature under consideration. Most engine manufacturer's specify the minimum acceptable acceleration times that must be produced to avoid possible "hot-starting" problems.

The peak drag-torque (occurring at the point of ignition during the compression cycle) usually, although not always, represents the maximum power requirement for starting. If excess values of drag-torque remain during the post-ignition phase, starting power requirements can peak at a point in speed other than the maximum torque speed. It is important to know in this case, in order to assure that the starter power is sufficient to accelerate the engine beyond ignition without inducing a "hot start" condition. This can be easily determined by converting the drag torque curve to a plot of demand and supplied power versus speed. In the example illustrated in Fig. 14, such a curve would follow a pattern similar to that of the drag-torque curve showing a peak start power demand of 9 hp occuring at 1350 rpm. (4)

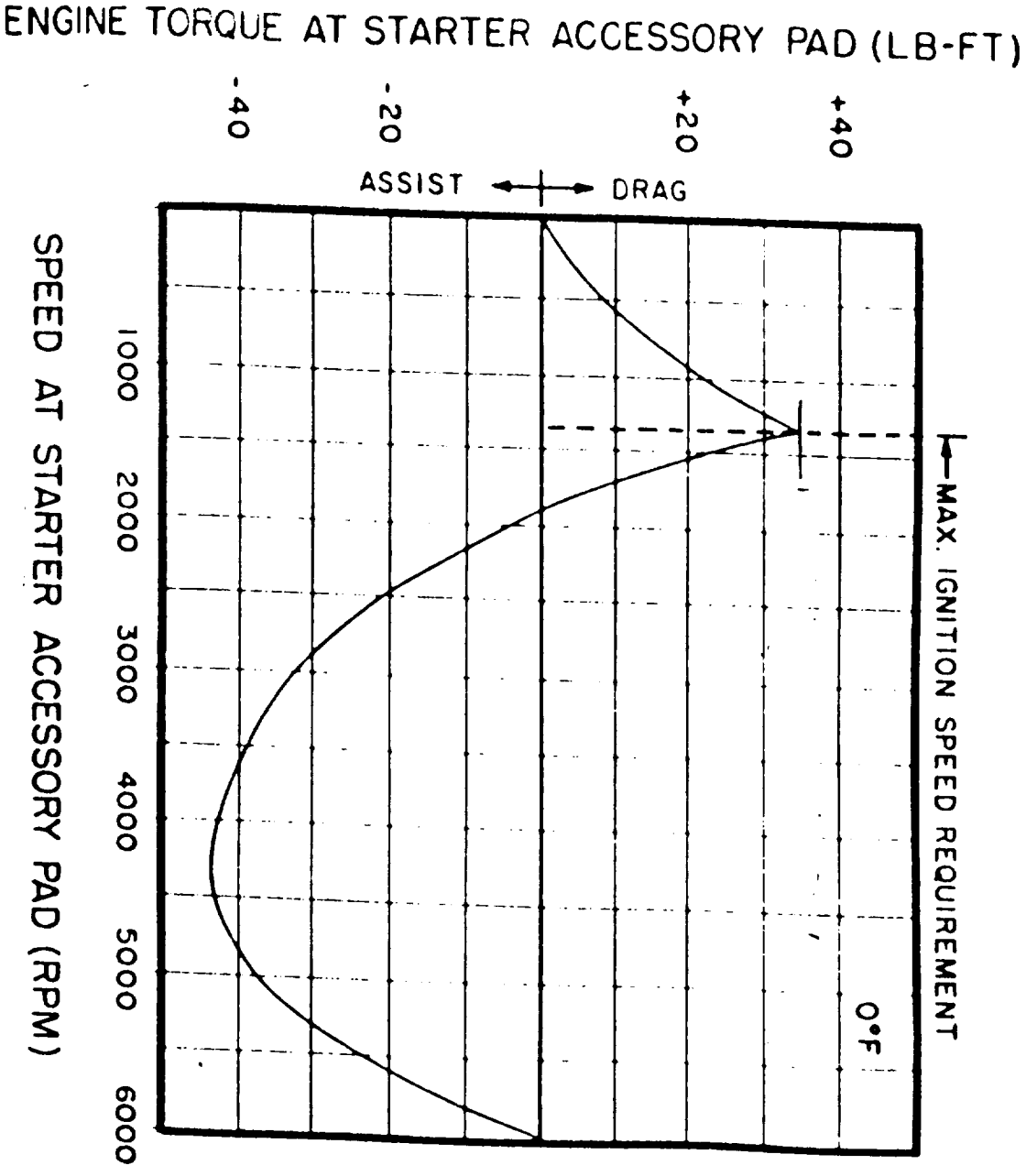
ENGINE TORQUE AT STARTER ACCESSORY PAD (LB-FT)
-40
-20
+20
+40
ASSIST
DRAG
SPEED AT STARTER ACCESSORY PAD (RPM)
1000
2000
3000
4000
5000
6000
MAX. IGNITION SPEED REQUIREMENT
0°F

FIG. E4

CONCLUSIONS

The following conclusions are derived from the contents of the paper concerning the power requirements and losses of various ancillary components of the rotary engine for a small aircraft:

---- An optimized system design will yield significant battery weight savings in difficult-to-start engine applications.

---- Significant starting-energy economics can be realized with an optimized system, allowing additional benefits to engine ignition operation and to component life of the battery, starter, contact points, and engine.

---- It was found from the study that the pumping efficiency may be improved for a given flow rate if the rotor width is increased while the rotor radius and the rotation speed are reduced.

---- The effect of the rotor diameter on the pumping efficiency is great, which is indicated by the relationship of r^5 for the fluid friction loss, and r^3 for the thrust friction loss.

---- The effect of the pump rotation speed (engine speed) is $n^{2.5}$ for the fluid friction loss, $n^{1.86}$ for the thrust friction loss, and nearly linear with with speed for the other variables.

---- The liquid cooling offers definite advantages over air cooling in the areas of durability and performance. Other advantages such as lower operating costs and operational improvements are more subjective and can only be substantiated with service experience.

---- Some of the other benefits include: Absence of cooling airflow anomalies, better cylinder wear characteristics, increased power output, significant reduction in cooling drag, and greater tolerance to operational abuse.

REFERENCES

1 Seilly, A. H., Ridel W. R., Advance in Cranking Motors, SAE Paper 821272, Warrendale PA, 1982

2 Scheidler M. S., Exploring Changing System Potentials, SAE Paper 841009, Warrendale PA, 1984

3 Gibson G. F., ME 406 - Automotive Engines (class notes), Michigan State University, East Lansing MI, Winter 1988

4 Eckert, A. F., Structural Requirements for Aircraft Engine, Main Fuel Pumps and Controls, SAE Paper 680058, Warrendale PA, 1968

5 Moss, N., An Optimized Engine Oil Pump, SAE Paper 851672, Warrendale PA, 1985

6 Higashiyama, K., Yamaguchi, H., Oshiage, K., Nissan's Present and Future Electronic Concentrated Engine Control Systems, SAE Paper 860596, Warrendale PA, 1986

7 Corbe, J. C., An Original Simulation Method for Car Engine Cooling Systems: A Modular System, SAE Paper 870713, Warrendale PA, 1987

8 Wilkinson R., Design and Development of the Voyager 200/300 Liquid Cooled Aircraft Engine, SAE Paper 871042, Warrendale PA

9 Jones C., The Rotating Combustion Engine - Compact, Lightweight Power for Aircraft, SAE Paper 670194, New York NY, 1967

10 Jones C., A Review of Curtis-Wright Rotary Engine Developments with Respect to General Aviation Potential, SAE Paper 790621, Warrendale PA, 1979

Appendix E

COMPUTER CONTROLLED MAPPING

OF

THREE DIMENSIONAL SURFACES

CRAIG OLBRICH
ME 499 DESIGN PROJECT
ADVISOR: DR. SCHOCK
JUNE 5, 1989

Table of Contents

Section		Page
1.	Introduction	1
2.	Methodology	2
3.	System Components	3
3.1	Point Range Sensor	3
3.2	Traverse Table	3
3.3	Portable Computer System	6
3.4	Object Mounting System	6
4.	Software	9
5.	Project Status	9
6.	Implementation Concerns	9

Figures

Figure		Page
1.	System Schematic	2
2.	Point Range Triangulation	4
3.	Surface Microstructure Effects	4
4.	Traverse Table	5
5.	Traverse Table Specification	6
6.	Zenith Portable PC specifications	7
7.	Bracket Design	8
8.	Software Control Diagram	10

2. Methodology

The system components consist of the point range sensor manufactured by CyberOptics Corporation, the table and controller computer manufactured by TSI, Inc., and the Zenith portable computer used to coordinate the sensor and the table movements. See Figure 1. The position of the table is measured by a Sony linear position encoder which measures the position of the table relative to its absolute home and transmits the position to the Zenith Computer. The Point Range Sensor is connected to the computer through a parallel interface card installed in the communication bus of the computer. The Sony encoder and the control for the Traverse Table are connected through RS-232-C port connections. The computer reads the position of the table and the measurement from the Point Range Sensor, it examines the data and determines the position of the surface being measured. The computer does this over a preset area and gathers the data for a computer generated surface.

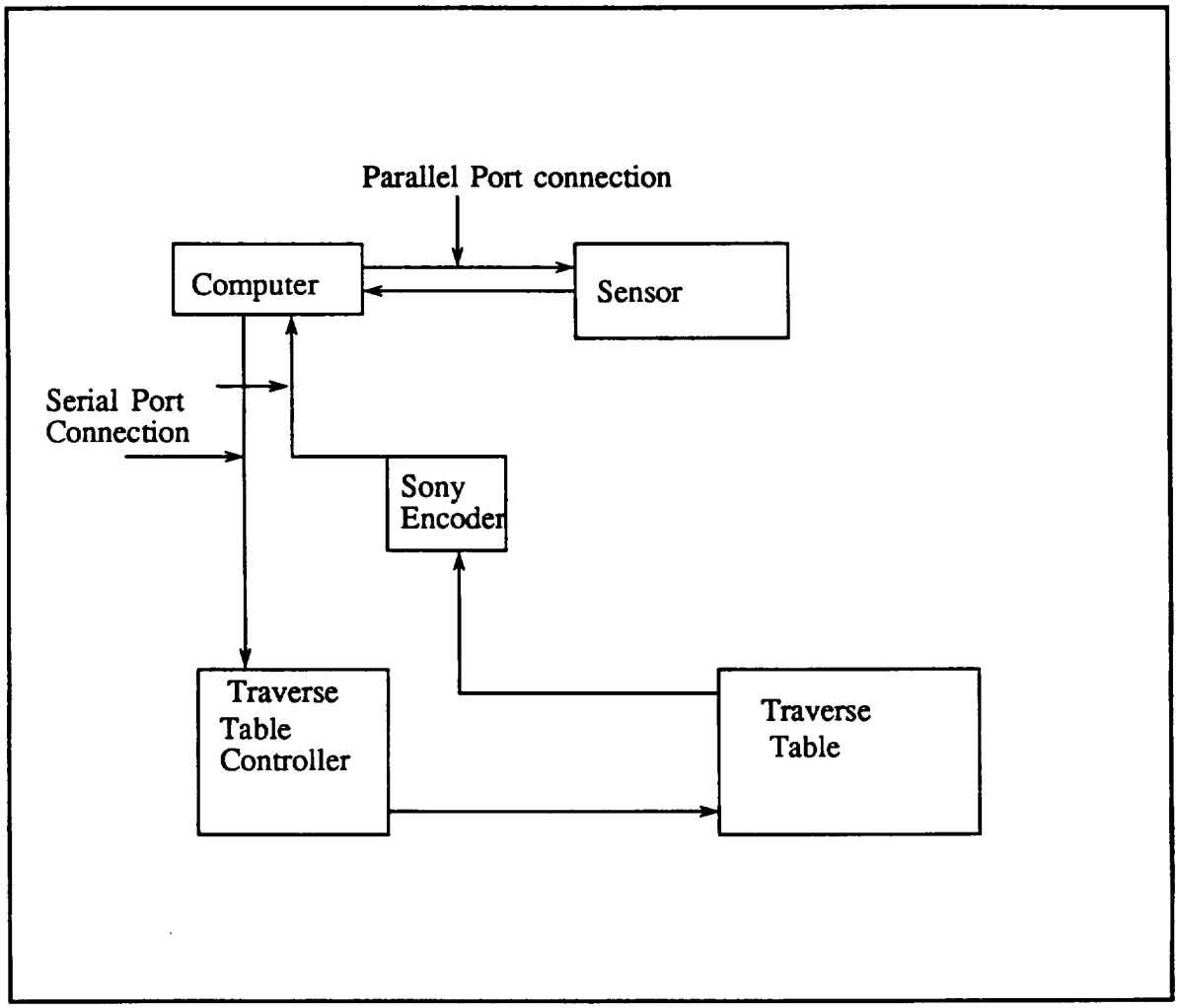

Figure 1
System Schematic

3. System Components

3.1 Point Range Sensor: (PRS)

The Point Range Sensor itself consists of several components. The sensor head contains the laser and the optical components used in the measurement of range data. The sensor is connected via a cable to the multiplexer/driver device. The multiplexer contains the actual electronics for controlling the sensor head and it is connected to the interface board installed in the computer. The computer controls all the parameters that affect the PRS through the device driver software written by CyberOptics Corporation.

The PRS sensor works by projecting and intense spot of near-infrared visible radiation onto the surface. A two-dimensional detector array gathers the reflected light and the data is transferred digitally to the computer. The computer processes the imaged data to determine the position of the centroid of the spot. This position allows for the calculation of range information due to the trigonometric relationship between the centroid position and the range. See Figure 2.

PRS performance can be measured by examining two items; the resolution and the accuracy of the sensor. The resolution of the sensor is the smallest change in Δz that can be measured by the sensor. See Figure 2. This is a function of how the sensor was designed, and is limited by the types of measuring intended for the sensor. The sensor chosen for this design is the PRS-800 sensor. This sensor has a resolution of twenty microns over a range of eight millimeters. The accuracy of the range data is dependent upon both sensor design and the surface microstructure details. The illumination spot has a Gaussian intensity profile. However non-uniform reflectivity may cause the image measured by the detector array to appear non-Gaussian and even non-symmetric. See Figure 3. Since all real surfaces have non-uniform reflectivity there may be a discrepancy between the actual intensity profile and the ideal profile used to calibrate the system. This will create an error in the measured centroid location. The absolute accuracy depends upon the surface being measured since all parameters are under the operators control. The operating range of the PRS-800 is eight millimeters and CyberOptics manufactures several other sensors with different ranges and resolutions. For this design, the smallest change in surface height attainable by this sensor is twenty microns, and the largest is eight millimeters.

3.2 Traverse Table System:(TTS)

The Traverse Table System manufactured by TSI, Inc. consists of three main components. The table upon which the PRS will be mounted, the control computer and the Sony encoder readout. See Figure 4. The Traverse Table System uses a computer to control the movement in the three axis directions. This computer, called the Modulynx, is interfaced with the PC and provides the input to the stepper motors that control movement. The control computer receives ASCII codes from the PC and translates the codes into a pulse train. The pulse train signal is sent to the stepper motors which then move the required distances. The position is measured by the encoders in each axis. This position is sent to the Sony readout which can display the position in either metric or English units. The range of movement of the table is 960 millimeters for the 'x' axis and 480 millimeters in the other two. See Figure 5 for the specifications of the table. It is important to note that the largest area that can be

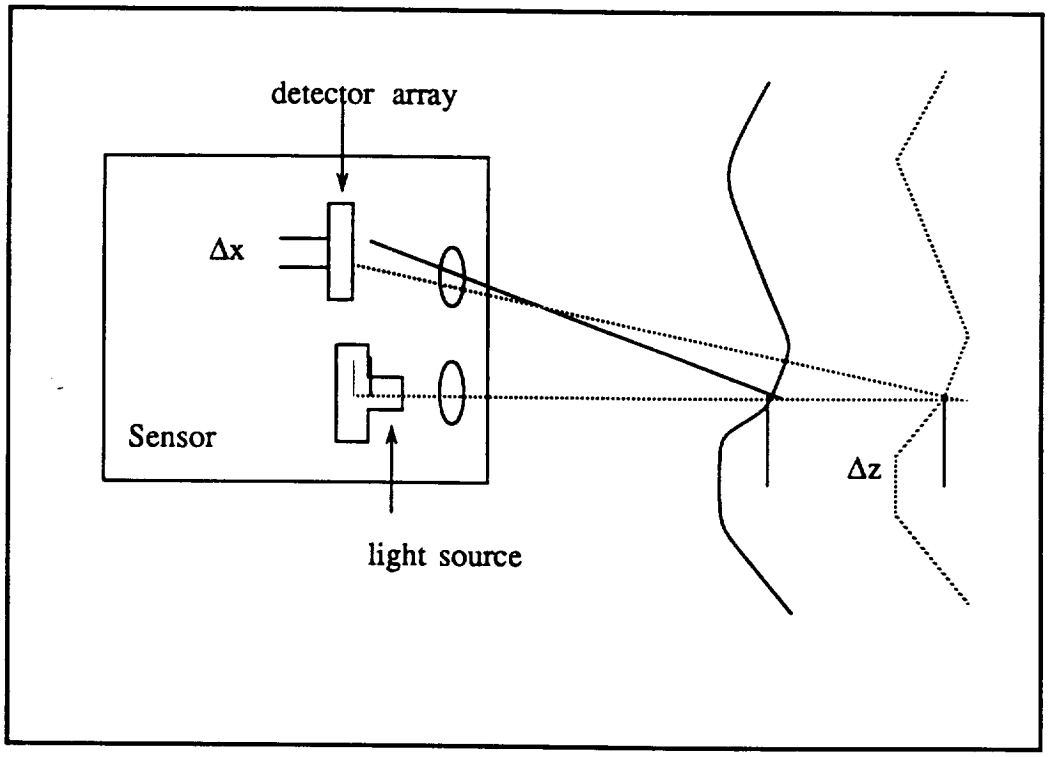

Figure 2.

Point Range Triangulation

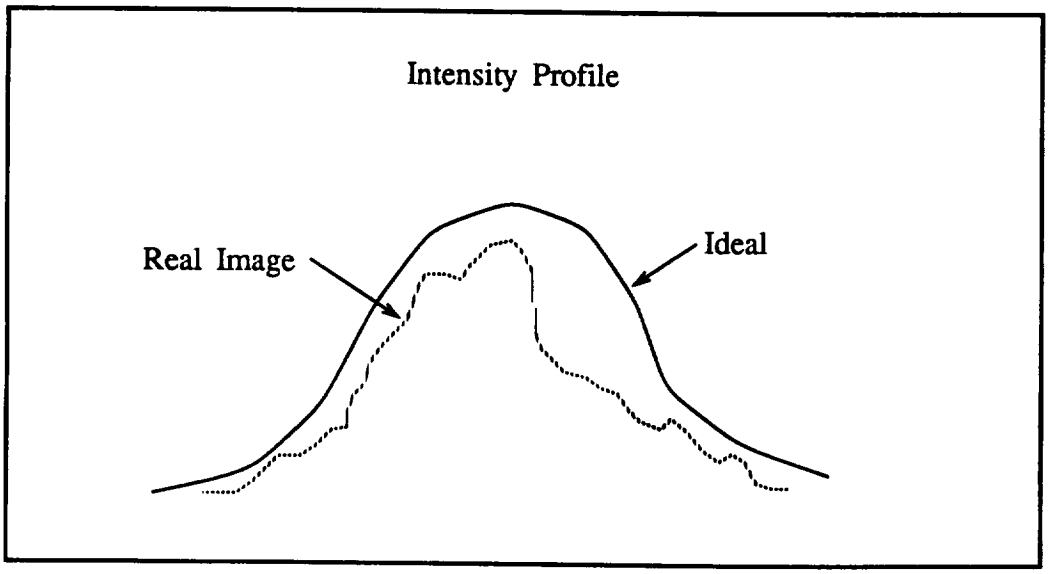

Figure 3.
Surface Microstructure Effects

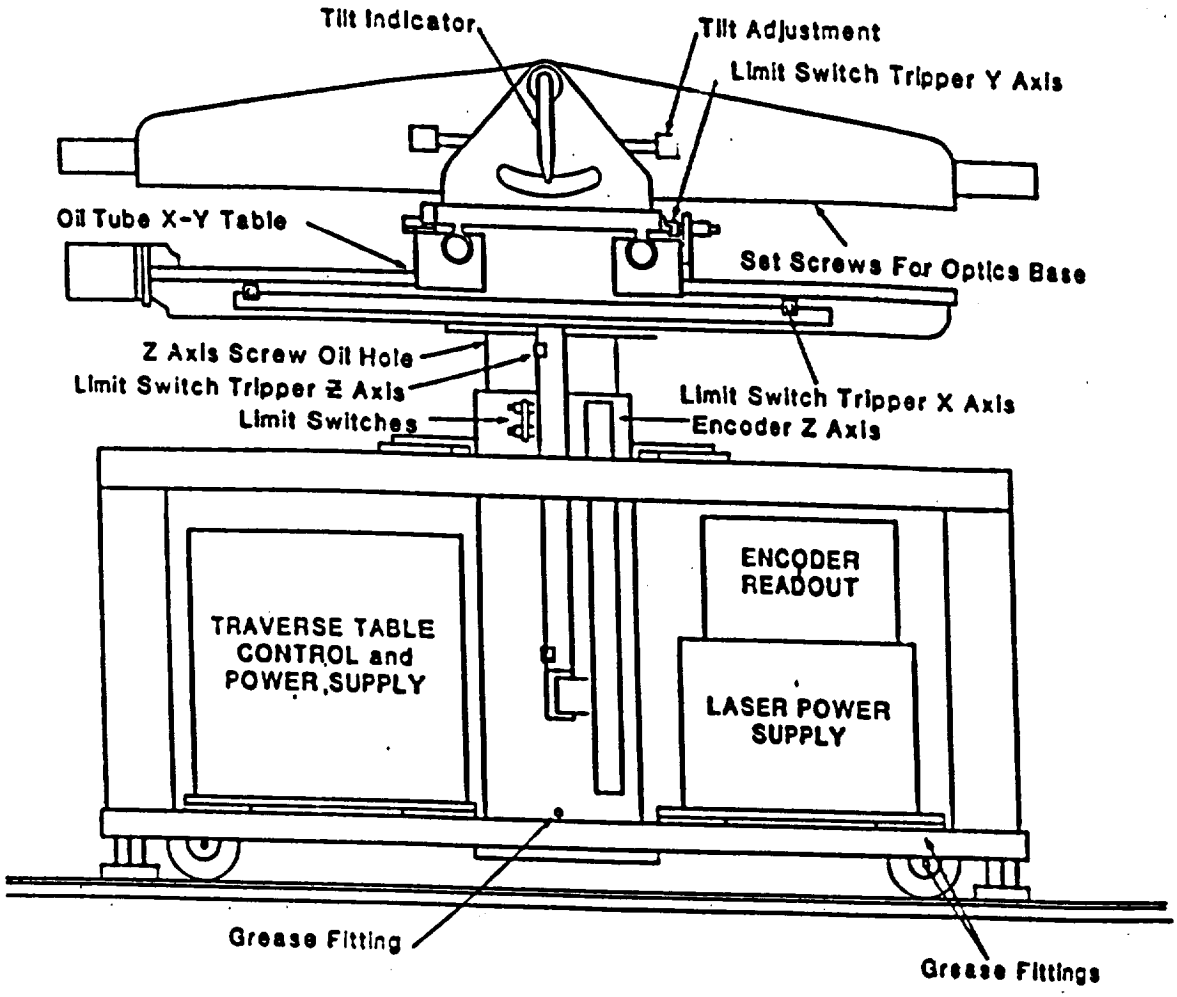

Figure 4.
Traverse Table

traversed for the purpose of PRS input is 960 x 480 millimeters. Of course it is possible to extend this limit slightly.

3.3 Portable Computer System:

A Zenith portable computer was purchased to control the entire system. See Figure 6 for the specifications. This computer interfaces with the Sony encoder readout, the Table modulynx control, and the PRS system. This is accomplished through two serial ports and one parrallel port. The PRS system is installed into the computer through a parallel interface card. The Sony is connected to one of the communication ports, called a serial port. This communication is accomplished through the use of RS-232 connectors and appropriate protocols. Another serial port is connected to the Modulynx. See Figure 1.

3.4 Object Mounting System:

The last two items which need to be mentioned are the mounting bracket for the sensor head and the stand for the object being measured. The mounting bracket need only hold the sensor head and not interfere with measurement. The bracket projects the head out from the table to allow for more flexible measurement. See Figure 7. This extension will allow limited mapping of concave objects as long as the sensor head will fit inside the opening. The stand for the objects themselves is dependent upon the object being measured.

TSI Traverse Table specifications:

Translation

x-axis	960 mm
y-axis	480 mm
z-axis	480 mm

Tilt of base	9 degrees
Minimum movement	2.5 μmeters
Readout Resolution	2.5 μmeters
Repeatability	2.0 μmeters
Nominal Traverse rate	5mm/sec
Load capacity	100 kg

Figure 5.
Traverse Table Specifications

Zenith TurbosPort 386

Processor - 80386 with 80387
numeric coprocessor

Speed - 12 or 6 MHz switchable

Drives - 40 MB hard drive and
3-1/2 inch disk.

Modem - 2400/1200/300 Hayes
compatible .

I/O ports - 1 Serial and 1 Parallel
plus expansion box for
three full size cards.

Memory - 2MB Ram

Power - Battery or 110v AC adapter/charger

Graphics - 640 x 400 pixel resolution

Figure 6.

Zenith Portable PC specs

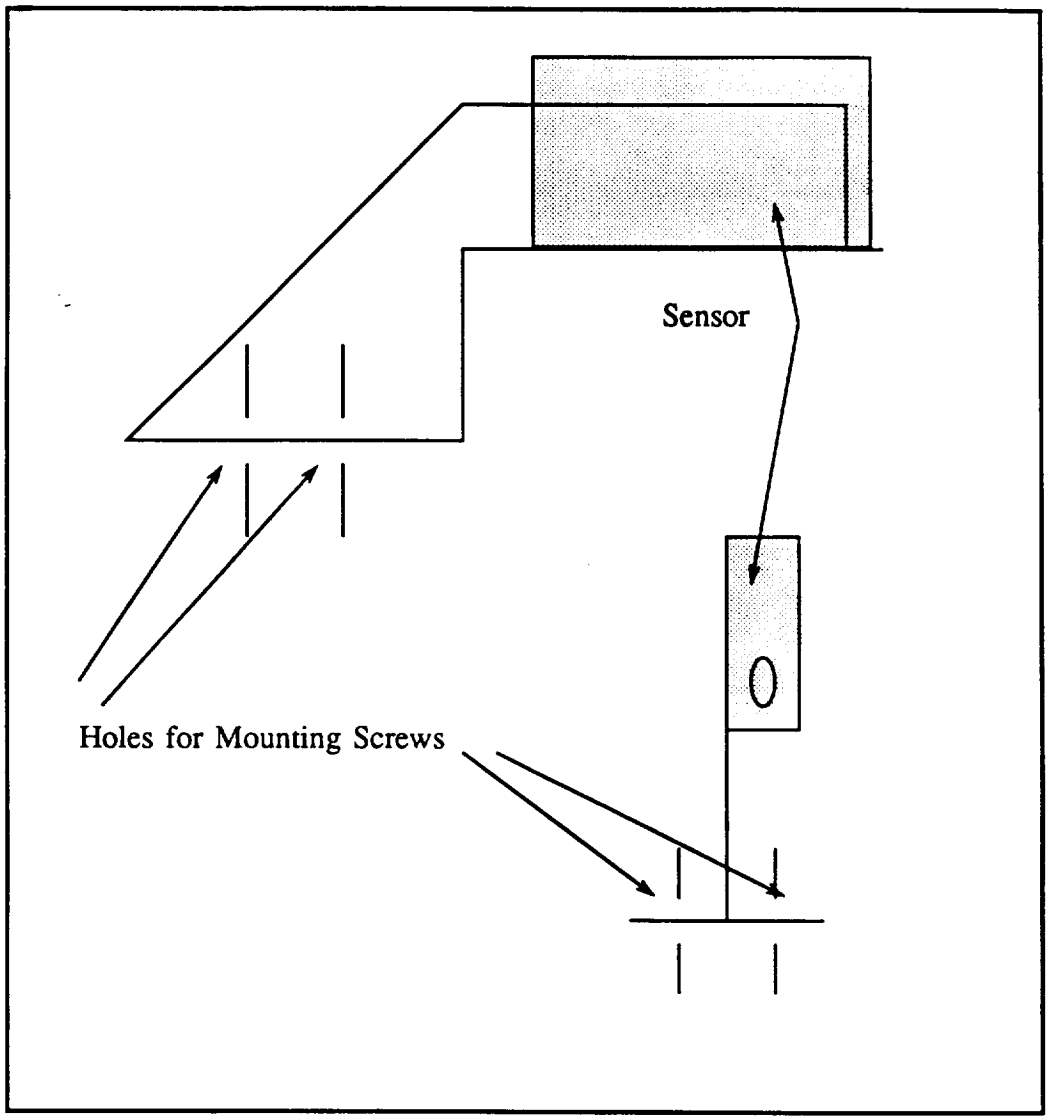

Figure 7.
Bracket Design

4. Software

There is a large amount of software which needs to be linked together to control the separate parts of the system. TSI has written procedures for controlling the TTS, and CyberOptics has a separate software package to control the PRS system. Control software to combine the two systems has been written by this author.

The difficulty in interfacing all three systems is in the different technologies used. TSI wrote their software in Fortran with some Assembly language subroutines to do the actual communication with the TTS. CyberOptics wrote their software as a memory-resident device driver and the controlling software was written in 'C' language. To integrate the separate systems, control software was written to combine the source code for each system. 'C' was used to write the control software for two reasons. 'C' allows flexible data sizes, so that variable size arrays can be implemented, and 'C' allows more effective interface with the more modern CyberOptics software. See section 6 on Implementation for comments on improvements.

5. Project Status

The PRS system has been purchased and delivered. The Traverse Table is available and is located in the MSU engine lab, it is also used for other projects. The Zenith personal computer has been purchased and delivered. The control software has all been written, however extensive testing and modifications will need to be done. A flow diagram of the control software is included in Figure 8.

6. Implementation Concerns

The Major concern for this type of imaging system is the table itself. Only one corner of the table is used for mounting the sensor. It would be more economical to use something that does not waste space. Perhaps a robot-arm mounted measuring device is more appropriate. It also would have slightly more flexibility for measuring objects. Another concern with the table is the controller design. The controller could measure its own position and supply the feedback, eliminating the Sony readout altogether.

On a more immediate basis the software could be improved merely by writing all of it in one language. This will remove all the interface problems that will occur with the three different languages.

The last topic that needs to be discussed is the accuracy and speed of the system. The maximum accuracy of the PRS sensor was pointed out in Section 3.1. The entire system's limits will be based on a combination of the three components, the laser, the PRS system, and the table. The computer has a 12 MHZ processor and the required code to manage the measurements is relatively small, so the limiting factor between the laser and the computer is a factor of the frequency response of the PRS sensor. The stated speed from the "Point Range Sensor User's Manual" is 3.00 milliseconds for a measurement. It is clear that the limiting factor is dependent upon the Traverse Table. The table is the largest moving part of the system and will have the slowest time responses. The difference is

mainly because of the digital nature of the other two components. The fastest sampling speed will then be dependent upon the settling time for the table motions. Surface microstructure will have an effect on these speeds by increasing the number of measurements required

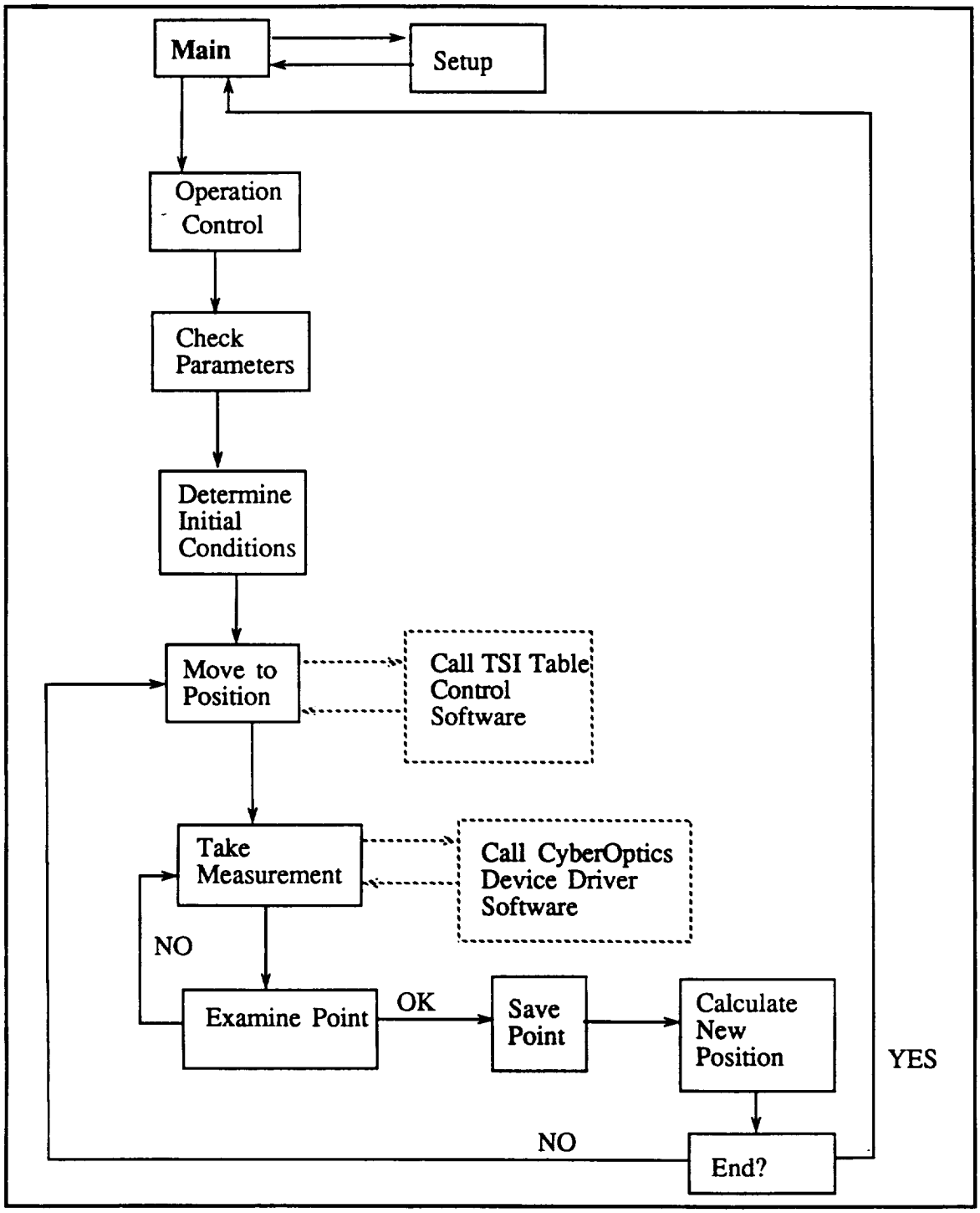

Figure 8.
Software Control Diagram